

CONDITION MONITORING AND ANALYSIS OF A PERMANENT MAGNET
SYNCHRONOUS MACHINE DRIVE SYSTEM

By

Andrew Stephen Babel

A DISSERTATION

Submitted to
Michigan State University
in partial fulfillment of the requirements
for the degree of

Electrical Engineering - Doctor of Philosophy

2014

ABSTRACT

CONDITION MONITORING AND ANALYSIS OF A PERMANENT MAGNET SYNCHRONOUS MACHINE DRIVE SYSTEM

By

Andrew Stephen Babel

Incipient faults in inverter-driven permanent magnet machine drives can often be detected and their progression monitored by some characteristic parameter in the machine's modeling equations. Some diagnosis and prognosis methods use features not reflected in the machine model, evident when voltage and current frequency harmonics are used. To indicate an inverter fault, a model of the inverter is instead used and its characteristic parameters found to detect parametric changes. Insulation condition is assessed by monitoring the high-frequency slot capacitance and high slot resistance. Demagnetization faults are detected by monitoring changes in the inductance.

In order to improve permanent magnet synchronous machine reliability, inverter faults must be detected in addition to motor faults. A minimally-invasive technique is developed which uses the device voltage-current characteristics. By detecting small changes in the voltage-current characteristic, each device's condition is assessed and the time to failure estimation is improved.

The remnant flux density of one or more rotor magnets in a PMSM can be reduced, resulting in demagnetization which occurs from either over-temperatures or excessive demagnetizing current. A magnet with reduced B_r also has a reduced H_c —it is more susceptible to further reversible demagnetization. Voltage and current harmonics can detect the presence of demagnetization, but cannot differentiate between rotor eccentricity and demagnetization in all cases. The direct axis incremental inductance can also be used to indicate demagneti-

zation because this can be used to detect a change in the saturation characteristic. Analysis is used to show the process of demagnetization.

Stator winding insulation failure has the potential outcome of catastrophic failure, cessation of operation, or the necessity for mitigation. Insulation degradation is either caused by voltage stress across the insulation or insulation thermal cycling. Because insulation degradation is reflected in the insulation's electrical characteristics, a method is presented to assess the insulation with its equivalent resistance and capacitance. A method is shown to assess the insulation condition with currents present during switching transitions induced by high dV/dt .

To Sandy and Fern

ACKNOWLEDGMENTS

I would like to express my gratitude to my advisor, Professor Elias Strangas, whose assistance, advice, and professional guidance have helped greatly in my professional pursuits and development. Without his guidance this dissertation would not have been possible.

Additionally, the work performed would not have been possible without the support staff, including, but not limited to: Brian Wright, Gregg Mulder and Roxanne Peacock.

Additionally, my colleagues at the Technical University of Graz were vital for this dissertation. I want to thank Professor Annette Muetze, Dr. Klaus Krischan, and Dr. Roland Seebacher for their collaboration, advice and assistance.

My friends and colleagues have been instrumental in completing my dissertation. Their diverse experiences and input have greatly enriched my experience. Their assistance, time, advice, and constant collaboration made this work possible. I would like to thank Cristián López-Martínez for co-designing the demagnetization machine with me. I would also like to thank Dr. Jorge G. Cintrón-Rivera and Professor Shanelle Foster for their close collaboration and time, as well as: Hendrik Kolbe, Reemon Haddad, Eduardo Montalvo-Ortiz, Alexander Connaughton, Feng Niu, Dr. Carlos Nino-Baron, Arslan Qaiser, Dr. Abdul Rahman Tariq, and Muhammad Jawad Zaheer. Professor Selin Aviyente and Professor Bringsen Wang provided valuable comments which increased the quality of this document.

My wife Cassandra has given me the crucial love and support I needed throughout this experience. My grandmother Fern Keen has, as always, given me invaluable support, as have my parents, Larry and Janet, and siblings Christina and Matthew.

TABLE OF CONTENTS

LIST OF TABLES	viii
LIST OF FIGURES	ix
Chapter 1 Introduction	1
1.1 General Background	1
1.2 Condition Monitoring and Failure Prognosis	2
1.3 Inverter Faults	3
1.4 Inverter Characterization	4
1.5 Machine Insulation Degradation	6
1.6 Demagnetization	8
1.7 Problem Statement	11
1.8 Methodology	12
1.9 Objectives and Contributions	12
1.10 Organization	13
Chapter 2 Theoretical Background	14
2.1 Motor Drive System	14
2.2 Machine Modeling	16
2.2.1 Machine Model Considering Saturation and Cross-Saturation	20
2.2.2 Machine Parameter Determination	22
Chapter 3 Inverter Condition Monitoring	27
3.1 Inverter Modeling	27
3.1.1 Representing the Semiconductor Voltage Drop	28
3.1.1.1 Expression for Voltage Drop with Direct Load Current	30
3.1.1.2 Expression for Voltage Drop with Alternating Load Current	34
3.1.2 Inverter Fault Monitoring	36
3.1.3 Thermal Model of Inverter	37
3.1.4 Thermomechanical Model of Bond Wire Lift-off	39
3.2 Characterization of Inverter Devices	40
3.2.1 Method Utilizing the Waveform Spectrum	41
3.2.2 Characterization with Developed Algorithm	43
3.2.3 Method Using DC Approximation with STFT	43
3.3 Diagnosis of Inverter Faults	48
3.3.1 Diagnosis with Inverter Characterization	48
3.3.2 Online Diagnosis	50

3.4	Effect of Bond Wire Lift-Off Faults on Lifetime	59
Chapter 4	Assessing and Effects of Partial Rotor Demagnetization	62
4.1	Apparent Inductance and Incremental Inductance	62
4.2	Demagnetization Machine	63
4.3	Detection of Demagnetization	70
4.3.1	Comparison with Uniform Demagnetization	78
4.3.2	Comparison with Pole Demagnetization	82
4.4	Susceptibility to Demagnetization	86
Chapter 5	Machine Insulation Assessment	88
5.1	Machine Insulation Degradation Diagnosis	93
5.2	Insulation Degradation Prognosis	98
Chapter 6	Conclusion	104
APPENDIX	107
BIBLIOGRAPHY	110

LIST OF TABLES

Table 3.1	Experimental resistances added	37
Table 3.2	Thermal model from the device losses for the IGBTs, diodes and module between the surface of the device (s) and the ambient (a) . .	38
Table 3.3	The thermal model from the datasheet between the device junctions (j), the sensor (r) and the ambient (a)	38
Table 3.4	Linear approximation parameter of device nonlinearity with added fault.	49
Table 3.5	Variance as a percentage of mean resistance for the resistances calculated from a linear regression of 27 power cycles taken in the saturation region.	49
Table 3.6	Filter Coefficients	53
Table 3.7	Enhanced MTTF prediction assuming that there are 68 thermal cycles in a day.	60
Table 4.1	Design constraints for demagnetization test machine	65
Table 4.2	Additional finite element model parameters	67
Table 5.1	Electrical characteristics of the insulation paper used [16]	88
Table 5.2	Nominal conduction and electrostatic finite element model characteristics	90
Table 5.3	Statistical Parameters used for the Kalman Filter	101

LIST OF FIGURES

Figure 2.1	Physical drive system components	15
Figure 2.2	Controller for a PMSM drive	15
Figure 2.3	Permanent magnet synchronous machine with rotor designed for use in the demagnetization testing	17
Figure 2.4	Stator phase axes and the rotor oriented axes	18
Figure 2.5	Physical illustration of stator and rotor oriented machine axes.	19
Figure 2.6	A generalized flux linkage with respect to current is shown for different current values.	21
Figure 2.7	Multiple current vectors applied during the characterization scheme	25
Figure 2.8	Data acquisition for controller development	26
Figure 3.1	Waveforms showing a generalized semiconductor nonlinearity, given as its voltage-current characteristics and the linear approximation to this with its equivalent parameters; this is the key characteristic for a device.	29
Figure 3.2	The phase A half bridge of the inverter, showing the sensor connection. The purpose of this figure is to demonstrate the paths of current, and how they relate to the voltage measured by the voltage sensor.	30
Figure 3.3	The experimental setup for inverter characterization is shown with the line-to-DCN voltage sensors.	32
Figure 3.4	Representations of the voltages measured with the sensor configuration in Figure 3.3	33
Figure 3.5	$V_{A \rightarrow DC}$ - measurement for an AC waveform showing the relationship between current and the measured PWM voltage. The voltages are: $(V_{\min}, V_{\max}) = (-V_{D2}, V_{I1})$ when current is positive, and $(V_{\min}, V_{\max}) = (-V_{D1}, V_{I2})$ when current is negative.	35
Figure 3.6	IGBT with bond wires and the added fault resistance	37

Figure 3.7	The resulting simulation and experimental waveforms for voltage with the spectrum method.	42
Figure 3.8	Characterization method used to determine the voltage and current relationship of inverter devices	44
Figure 3.9	Results of voltage drop spectrum extraction.	45
Figure 3.10	Experimental results of voltage drop spectrum extraction for AC using STFT.	47
Figure 3.11	Experimental device characteristics under different fault levels.	49
Figure 3.12	Characterization method used to determine the voltage and current relationship of inverter devices	51
Figure 3.13	Filter used for online device diagnosis method	52
Figure 3.14	Quantities used as inputs to the online diagnosis method	53
Figure 3.15	Variables extracted with the spectral characterization method	54
Figure 3.16	Cumulative sum function and fault flag set for f_{r1}	57
Figure 3.17	Cumulative sum function and fault flag set for f_{r2}	57
Figure 3.18	Cumulative sum function and fault flag set for f_{r3}	58
Figure 3.19	Cumulative sum function and fault flag set for f_{r4}	58
Figure 3.20	Paths to failure for BWLO in one phase of an IGBT inverter system, shown here for four bonds.	59
Figure 3.21	The change in MTTF estimation under different fault levels with the enhanced RUL calculation.	61
Figure 4.1	B-H curve for a generic magnet material	63
Figure 4.2	A generalized flux linkage with respect to current (blue) is shown along with the corresponding incremental inductance (green) and apparent inductance (red).	64
Figure 4.3	Rotor dimensions used to optimize torque ripple	66

Figure 4.4	Magnet placement results of the optimization procedure	67
Figure 4.5	Finite element model designed and used for the demagnetization method evaluation	68
Figure 4.6	Finite element model for test machine	68
Figure 4.7	Finite element model for test machine	69
Figure 4.8	Three phase back EMF taken at 300 RPM	70
Figure 4.9	Torque profile for current range; taken at 300 RPM	70
Figure 4.10	Nominal torque ripple calculated from the FEM at $18A_{\text{rms}} \angle 117^\circ$ at 300 RPM	71
Figure 4.11	Field lines with normal magnetization	72
Figure 4.12	Field lines with one completely demagnetized magnet	73
Figure 4.13	Torque ripple due to demagnetization calculated from the FEM at $7.1A_{\text{rms}} \angle 117^\circ$ at 300 RPM	74
Figure 4.14	Line-to-line EMF and comparison of harmonics.	75
Figure 4.15	Line-to-line voltage and comparison of harmonics at 300 RPM and $7.1 A_{\text{rms}} \angle 117^\circ$ for varying degrees of magnet two demagnetization.	76
Figure 4.16	Incremental inductance and flux linkages for partial demagnetization testing of the designed machine	77
Figure 4.17	Torque ripple due to demagnetization calculated from the FEM at $7.1A_{\text{rms}} \angle 117^\circ$ at 300 RPM	78
Figure 4.18	Line-to-line EMF and comparison of harmonics for uniform demagnetization.	79
Figure 4.19	Line-to-line voltage and comparison of harmonics at 300 RPM and $7.1 A_{\text{rms}} \angle 117^\circ$ for varying degrees of uniform demagnetization.	80
Figure 4.20	Incremental inductance and flux linkages for uniform demagnetization testing of the designed machine	81
Figure 4.21	Torque ripple due to pole demagnetization calculated from the FEM at $7.1A_{\text{rms}} \angle 117^\circ$ at 300 RPM	82

Figure 4.22	Line-to-line EMF and comparison of harmonics for uniform demagnetization.	83
Figure 4.23	Line-to-line voltage and comparison of harmonics at 300 RPM and $7.1 A_{\text{RMS}} \angle 117^\circ$ for varying degrees of uniform demagnetization. . . .	84
Figure 4.24	Incremental inductance and flux linkages for uniform demagnetization testing of the designed machine	85
Figure 4.25	Percentage of demagnetized nodes with respect to remnant flux density and direct axis current	87
Figure 5.1	Degradation characteristic curves	89
Figure 5.2	Finite element model geometries used to determine the slot characteristics.	91
Figure 5.3	Finite element model simulation results under parameter variation; use Figure 5.2(a) as reference	92
Figure 5.4	Plot showing the change in voltage failure performance with no partial discharge and as the voltage decreases (from [12])	93
Figure 5.5	Machine stator equivalent circuit; n is the total number of conductors in the slots per phase	94
Figure 5.6	Leakage current measuring test circuit.	95
Figure 5.7	Simulated leakage current with applied voltage; (a) shows about $400 \mu\text{sec}$ of data and (b) zooms into up to $70 \mu\text{sec}$	95
Figure 5.8	Leakage current after the initial voltage pulse is applied to the phase	96
Figure 5.9	Experimental leakage current shown with detail	97
Figure 5.10	The original data from Younsi <i>et al.</i> [50] and an exponential fit for this	98
Figure 5.11	Estimated leakage current shown with the measurements and actual leakage current	103
Figure A.1	Circuit to scale the voltages to within the analog to digital converter limits.	109

Figure A.2 Experimental phase A operating voltages and result used to test the circuit. 109

Chapter 1

Introduction

1.1 General Background

Electric drive systems and the inverters used to control them are quickly becoming ubiquitous. The introduction of electric machine drives into these applications cannot come at the expense of reliability. It is possible to improve system reliability and thus alleviate this concern with the development of methods to evaluate the condition and predict the lifetime of these systems.

A survey of industry in [48] demonstrates that the field of condition monitoring and reliability studies in general need to be expanded upon to allow for the greater proliferation of reliability methods.

The goal is to predict a failure correctly and as early as possible [51]. This failure typically shows some observable signature before the failure occurs. A fault is the early detectable condition which may allow for continued operation but will eventually lead to the catastrophic failure of the system.

Motor drive faults are often reflected in the machine model parameters. There are, however, times when this is not true, due to: inverter faults, higher-order effects, or the lack of a parameter which reflects the specific fault. Three such faults are studied: inverter bond wire lift-off faults, insulation faults, and demagnetization faults. Inverter faults can be detected in the nonlinear device characteristics, something not included in the normal

machine mode. Insulation faults are detected using the high-frequency slot leakage current, for which there is no parameter in the machine model either. Finally, demagnetization faults are not easily reflected in the machine model other than the reduction in the flux linkages due to the magnets. Given the ability to model these faults in alternative ways, diagnostic and prognostic schemes can be introduced to improve the reliability of the drive.

1.2 Condition Monitoring and Failure Prognosis

Song and Wang [40] give an overview of the growing field of reliability and they review some reliability calculations. Song and Wang [40] describe the mean time to failure (MTTF) calculation, a measure of the remaining useful life (RUL) of a component or system. Additionally, the paper [41] by Song and Sarwate clearly describes the four main areas of reliability:

1. diagnosis,
2. prognosis,
3. fault mitigation, and
4. redundant or fault-tolerant design.

In the field of diagnosis, the presence and severity of a fault in a system is determined. This is the most mature portion of reliability studies; many methods have been discussed in literature. Prognosis seeks to determine the RUL of a device with a fault as well as the probability of the fault worsening and causing complete failure. Fault tolerant design is an approach which improves reliability, where the system is designed to be resistant to failure. Mitigation is the change in operation, such as limiting operation to low power, to allow continued operation with a fault and delay the onset of catastrophic failure.

1.3 Inverter Faults

Given their applicability to drive systems, MOSFETs and IGBTs were reported to be of the most interest for inverter reliability [48]. Since IGBTs typically have a higher power rating and so are used more often in traction drive systems, the discussion in this work will be limited to IGBTs and their corresponding freewheeling diodes.

Yang *et al.* , in [49], present physics-based reliability models for some common inverter device faults; the bond wire lift-off (BWLO) fault is discussed in this work because it is a common device fault.

The diagnosis of BWLO faults in IGBTs has been studied in [8, 45, 11, 21, 39, 1]. There are two approaches: first, determining the fault presence with voltage harmonics, current, or added test equipment; second, diagnosing a fault by determining the device parameters.

The first diagnostic approach relates the fault to voltage, current, or their harmonics. In [39], a fault is diagnosed by monitoring the magnetizing and torque-producing currents in an induction machine drive inverter. The fault is related to the voltage harmonics for the solder bond fatigue fault in [45].

Mengoni *et al.* [29] detect small changes in one of the phase resistances in order to detect phase connection problems. Meinguet *et al.* [28] use the phase current magnitudes and frequencies to quickly detect an open circuit fault.

The second diagnostic approach relates the fault to device characteristics. In Xiang *et al.* [46], the effect of BWLO on the device characteristics is seen. The authors acknowledged that determining the device characteristics accurately is difficult. Because the characterization method in this dissertation can determine the characteristics of every inverter device, it is possible to use for diagnosis. There are online methods for diagnosis, such as the PCA-

based method by Anderson *et al.* [2], but a method which can extract parameters in a noise immune way and use this is introduced in this work.

There are two approaches to prognosis for BWLO: monitoring some signal which indicates time to failure and the use of a physics-based model to determine the time to failure. The monitoring approach is taken in [47], where BWLO failure was found to be preceded by a precipitous decrease and subsequent increase in V_{CE} . The Arrhenius relationship was used to model BWLO in [24]; with accurate knowledge of the Arrhenius parameters and the device temperature, an accurate MTTF is found. The Arrhenius method provides a way to calculate RUL at any point in the device's operating life, while the V_{CE} monitoring method can only give warning shortly before failure.

1.4 Inverter Characterization

Semiconductor devices have a nonlinear anode-cathode or collector-emitter voltage drop with respect to the diode current or collector current, respectively. This dissertation is to develop a technique to find the voltage-current characteristic of each of the IGBTs and diodes constituting a typical industrial inverter. The forward voltage drop is the most practically measurable quantity, given the typical industrial drive sensor setup of current and voltage sensors on the phases; it is not possible to extract the gate-to-emitter voltage, another voltage drop in an IGBT, when there are no voltage sensors connected to the gate. The turn-on and turn-off times of the semiconductors are not measured because this work studies only the static device voltage drop characteristics.

Typically, the nonlinear inverter voltage drops are ignored, but their values can be used for condition monitoring.

Condition monitoring for inverters is nascent, but has been discussed in some work, such as [49]. The magnitude of the voltage drop can also reflect the health of each of the devices. Condition monitoring applied to inverters investigates the value of these nonlinearities; a change in these can indicate a developing fault.

The authors in [17, 44, 23, 5] find the average voltage drop of the IGBT and its freewheeling diode. The offline method in [17] uses the voltage command and measured current together with a flux observer that estimates the linearized voltage-current relationship. Liu *et al.* [23] estimate the voltage distortion online using an adaline observer while the machine is operating with no current in the direct axis. The authors of [44] and [5] discuss similar methods which use a machine model and a standstill DC test to find the voltage-current relationship. The result is a voltage-current relationship that is the average of the voltage drop over the IGBT and its corresponding freewheeling diode.

For wide-spread application in the field, a technique needs to be both simple and able to characterize each device. This work seeks to characterize an inverter over its entire current operating range. To isolate each individual quantity, new and simple characterization methods have been developed. The proposed method uses voltage sensors placed between the inverter phases and the negative DC link. Multiple current magnitudes are applied in order to get the entire current range of the device. The proposed method, referred to as the “spectral method”, uses the current measurement with the voltage harmonic content; this is done by analytically determining the relationship between the Fourier transform components and the device voltages. This is done first with a range of direct currents. The spectral method used in the DC case is then extended to the AC case with the short time Fourier transform [51]. Another method which manually extracts the quantities by determining the mean maximum and minimum values of the PWM voltage is used to determine the actual

value of the nonlinearities; this is called the “algorithm method”.

1.5 Machine Insulation Degradation

Winding shorts can cause expensive and inconvenient unexpected downtimes; stator winding short problems cause 25% of electric machine failures below 4 kV [31]. If it is possible to assess the condition of the insulation and a model describing the degradation is known, the length of time to a failed state or short formation can be estimated.

The insulation is compromised when its dielectric strength and mechanical properties are reduced from their respective healthy states. When the dielectric strength and mechanical properties are compromised, the likelihood of short formation and failure is higher.

There are four main approaches to machine insulation monitoring: destructive surge testing, non-destructive partial discharge (PD) surge testing, high-frequency response, and dielectric characterization. Destructive surge testing is avoided because it damages the machine and partial discharge does not apply for low and medium voltage machines. The high frequency response testing, exemplified by [32, 33], analyzes the frequency response of the current with applied voltage (or sometimes analyzes the voltage with applied current) to determine whether degradation is present. The high frequency response is useful if the sampling frequencies required are available. The final method calculates representative variables of the machine insulation: capacitance, resistance, and dissipation factor (DF). This approach is taken by [34, 50, 13]. The machine parameter methods are very reliable, since the parameters are known to track the insulation condition well.

Without partial discharge measurement, as is the case with low to medium voltage machines, assessing the insulation must be done without relying on partial discharge measure-

ments. The methods given by [50] and [32] accomplish just this. In the Younsi *et al.* [50] paper, the insulation is assessed directly by measuring the magnitude of current in the insulation and the angle between the resistive and capacitive components of the current. This method is useful because it uses features which relate directly to the physical properties of the insulation. The downside is that it requires very sensitive sensors because the insulation current is so small, often less than 100 mA. In the Nussbaumer *et al.* method, the insulation condition is assessed by measuring the frequency response of the current during switching transients. This method is useful because it does not require expensive sensors, but having a method that relates directly to the insulation current would be more useful.

The proposed method uses the best of both methods; the switching transient with a PWM-controlled voltage source inverter is utilized with the current measurement. By measuring the current at the switching transient, the magnitude is much larger than the grid connected insulation current. The method measures the current magnitude because it has a direct relationship to the insulation condition. Diagnosing degradation by using the current magnitude during the switching transients is novel.

Pascoli *et al.* [34] investigate the effect of normal aging on large machines during real operation over the course of multiple decades; they do so by measuring the effect of aging on the insulation characteristics. This study clearly shows that the parameters change under normal circumstances. [50] is an especially compelling paper because it performs thermally accelerated aging on a low voltage bar-wound induction machine and monitors the change of insulation current and the angle of the current until machine failure. [50] shows a clear decrease in the insulation current and current angle in time. This paper demonstrates that insulation current is useful for determining the state of the insulation.

In [50], the trend in insulation current exhibits exponential decay behavior in time. In

low voltage machines, heating from losses and current in the insulation plays the largest role. The RUL is determined by extrapolating the insulation current magnitude behavior. A degradation model is needed for RUL extrapolation; this is found by fitting the insulation current to an exponential model with the Extended Kalman Filter (EKF). This concept is demonstrated as effective for RUL calculation in [7]. The application of the EKF to fit the behavior of the change in insulation current to an exponential model is novel.

1.6 Demagnetization

Rotor demagnetization is defined here as the reduction in the remnant flux density of one or more of the magnets of a PMSM with a wound armature and rotor with magnets. Rotor demagnetization may have many negative effects. If all of the magnets have a reduction in B_r , the effect is a reduced λ_{af} ; this results in a reduced torque, per the PMSM torque equation $T_{em} = \frac{3P}{2} [\lambda_{af} + (L_d - L_q)i_d] i_q$. When one magnet is demagnetized, the asymmetry of the airgap flux density may result in increased torque ripple as well as decreased average torque. Demagnetization of one or more rotor magnets may affect the rotor saturation and current angle for maximum torque; demagnetization therefore has an effect on alignment.

Assessing the condition of the rotor magnets can inform maintenance and the control algorithm. If the condition of the rotor magnetization is known, demagnetization faults can be diagnosed or ruled-out. The controller may also be able to ameliorate negative effects of demagnetization and increase torque production by changing the ratio of magnet and reluctance torque, or by applying higher current magnitudes. Demagnetization also reduces the resistance to further demagnetization by lowering the magnet coercive force. This may even result in the knee of the magnet entering the second quadrant; to avoid further

demagnetization, the magnitude of demagnetizing current, ($|i_d|$) should be appropriately limited in the control algorithm.

Increasing the temperature over the nominal value decreases the B_r and H_c and moves the knee closer to the second quadrant, or in it. [26] For small increases in the magnet temperature, the demagnetization is reversible. If the temperature is high enough, the operating point on the BH curve may fall below the knee, resulting in a decrease in B_r . When a magnet is partially damaged, the effective magnetization is also reduced [18]; this affects the performance. When the coercive force is reduced, the magnet's ability to reduce a demagnetizing field is reduced; this could lead to a further reduction in the remnant flux density. For this reason, the controller should limit the demagnetizing current in order to limit the demagnetizing field.

There are two types of methods to diagnose demagnetization faults: using harmonics or incremental inductance. Harmonic-based methods utilize the harmonics of the flux linkages due to the magnets, back-EMF [6], or stator currents [38, 37, 10, 36]. Casadei *et al.* [6] show that by analyzing the harmonic content of the back-EMF and flux linkages due to the magnets that demagnetization can be detected. MCSA is used to the same ends in [38, 37, 10, 36]. Rosero *et al.* as well as Espinosa *et al.* use the Hilbert-Huang transform to diagnose demagnetization during non-stationary conditions while Riba-Ruiz *et al.* use the DWT to detect demagnetization under non-stationary conditions. One drawback mentioned by Espinosa *et al.* [10] is that the same harmonics that are presented during demagnetization are also presented by eccentricity. In order to overcome this, a model based method was introduced by Hong *et al.* [18] which uses change in incremental inductance changes due to less saturation to detect if there is uniform or partial demagnetization. The authors also differentiate between the change in inductance due to demagnetization from eccentricity.

A detailed look at partial demagnetization is taken in this dissertation to understand its effects and have a robust detection method. The voltage and current harmonics can be used to indicate that a fault exists but this method cannot differentiate demagnetization from eccentricity. The inductance characteristics of the direct rotor oriented axis are used to verify the harmonic-based detection findings. The detection of partial demagnetization is improved by determining the incremental inductance over a range of direct axis currents; this way secondary 'knees' caused by asymmetrical rotor saturation are found. This asymmetrical saturation can be determined with the inductance.

Prognosis normally describes the calculation of remaining useful life for a system, given a certain fault. Magnets demagnetize over time, but this process is slow: temperature and demagnetizing currents are more likely to cause demagnetization. The coercivity force can be reduced by many effects—mechanical damage, elevated temperature or prior magnetic demagnetization. A lower coercivity force allows the magnet to be demagnetized with less applied field. In order to avoid demagnetization, care should be taken during design and by the controller to not apply excessive, damaging currents. In this dissertation, the effects of demagnetizing current on a healthy machine and a machine with reduced magnetization are studied with the goal to prevent further demagnetization. Demagnetizing current is normally applied to develop reluctance torque, weaken the rotor field at high speeds, and possibly during abnormal current controller operation. Preventing further demagnetization involves two steps: evaluating the state of magnetization with diagnosis and setting the limits on the controller.

A previous study by McFarland and Jahns [26] shows the demagnetizing effect of negative direct axis current on the different portions of the rotor magnets. In [27] the effect of currents due to stator shorts on the magnet properties is shown. The maximum demagnetizing current

can be found by empirically studying the demagnetization behavior of the magnets using finite element analysis. Expressions for the motor magnetizing current are determined and used as limits in the controller.

1.7 Problem Statement

The machine voltage equations do not describe the drive behavior enough to account for all faults, especially inverter bond wire lift-off faults, insulation degradation and demagnetization.

The inverter parameters are not represented in the machine model at all; small changes to the resistance of the bond wire are very small compared to the winding resistance, thus no effect will be seen in the winding resistance until an open circuit forms.

Insulation degradation precedes a short circuit fault, which can be catastrophic to the drive. The problem lies in the fact that the degradation is often only detectable once a short has formed. By creating a model which can be used to show leakage current—which is representative of insulation degradation—the short prediction may be improved.

Demagnetization can affect performance a great deal if severe enough by increasing torque ripple amongst other effects. While demagnetization may be detectable with the machine voltage equations, the susceptibility to further demagnetization is not as clear, it is not uniform throughout the magnet and depends on temperature as well as previous magnetization level. Additionally, partial demagnetization may not be enough severity to show up in the flux linkage due to the magnets term, λ_{af} , of the machine equations.

1.8 Methodology

This dissertation proposes condition monitoring methods which are model-based but do not use the typical voltage-flux-current machine model equations. The additional models allow for contributions to the condition monitoring of drives in general and serve to complement the existing condition monitoring methods—particularly short-circuit, open-circuit, eccentricity, and bearing monitoring methods.

A series of off- and on-line tests are performed on the drive. The tests all involve the calculation of advanced model parameters: device V-I characteristics, insulation current, and incremental inductance. These advanced model parameters are related to the condition of the inverter and motor components of the drive.

The parameters influence the controller because they inform the controller of appropriate constraints needed to extend the life of the drive. Additionally, they provide lifetime information that is important for planning service for the drive.

1.9 Objectives and Contributions

An inverter characterization method is proposed to determine the V-I characteristic of the switches. The V-I characteristic is used to track the health of each diode and IGBT. By tracking each device, the problem or diode is isolated. By determining the V-I characteristic of each device, the health can be determined even before a short or open occurs.

To assess the insulation condition, a test is proposed which uses minimum added hardware. By using FEA and a lumped parameter model to model the degradation behavior, the prognosis method was developed. Diagnosis and prognosis methods were developed which can assess the condition of the insulation with insulation current that occurs during PWM

switching transitions; the trend in this is used to track the condition over time.

A demagnetization detection scheme is introduced which is effective for determining partial demagnetization by using the saturation characteristic of the steel. The change in saturation with demagnetization is detected by incremental inductance at standstill. The severity of remnant flux density reduction with a demagnetizing field is explored and used to determine the maximum demagnetizing current in a variety of areas.

1.10 Organization

In Chapter 2 some background is given about drives. The typical machine and inverter models are given with the typical control scheme. In Chapter 3, inverter condition monitoring is discussed—both how to detect the condition of an inverter and the effect of parameters upon the lifetime. In Chapter 4, the detection of partial demagnetization is discussed along with the susceptibility of rotors with magnets to demagnetization. Finally, in Chapter 5 A detection method for insulation is given. The role of the condition monitoring is discussed as it relates to existing condition monitoring methods.

Chapter 2

Theoretical Background

2.1 Motor Drive System

A typical PMSM drive is given in Figure 2.1. The power electronics are used to interface the power source—in this case the grid—with the drive. The first component rectifies the voltage which is applied across the capacitor of the DC link. The inverter converts the DC link voltage to the appropriate AC voltage; the machine is driven by this AC voltage. The inverter IGBTs are controlled by a DSP which generates the appropriate gating signals with the sensed quantities. In order for the machine to be controlled, current sensors are attached to the machine phases in addition to an encoder or resolver which senses the rotor position. Current, position, and DC link voltage are most often used by the machine controller. The same quantities and sometimes the voltage are saved to a PC in our experimental setup for characterizing the machine in post-processing and for gathering other data.

A general controller is given for a PMSM drive in Figure 2.2. Going from left to right, the first block is the torque controller, which inputs both the actual drive speed and desired torque and outputs the corresponding currents. The second block is the current controller, which uses PI controllers to calculate the appropriate voltages to generate the desired currents; the measured currents are used to achieve this. The third block transforms these rotor-oriented quantities to the stationary frame of reference. The final block uses a space vector scheme to determine the gating signals needed for the appropriate voltage.

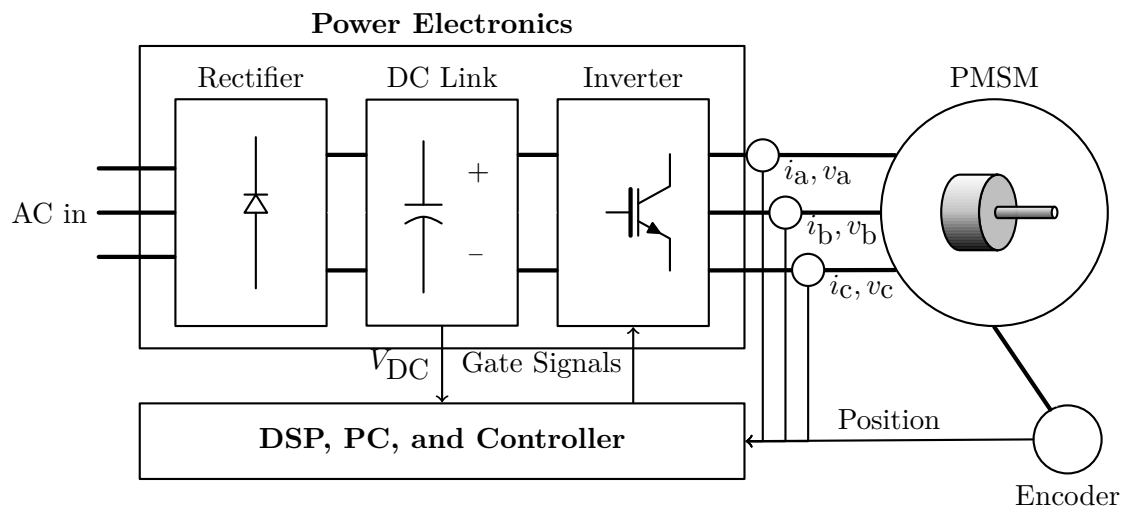


Figure 2.1: Physical drive system components

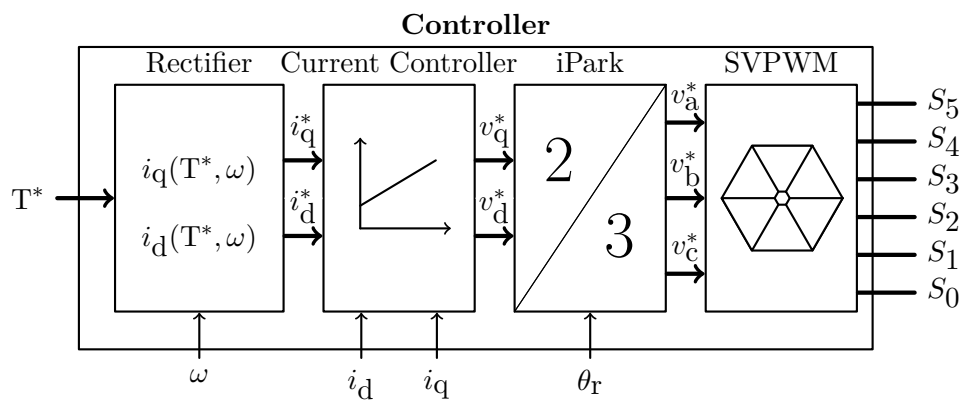


Figure 2.2: Controller for a PMSM drive

2.2 Machine Modeling

While expensive, PMSMs are valuable for their torque density and efficiency. Additionally, the fact that the coercivity of the Neodymium Iron Boron and Samarium Cobalt magnets is so high prevents demagnetization at low currents. The magnets also have a much higher remnant flux density than Alnico or ferrite magnets. This allows for the design of small machines with a high power, thus allowing for small kW-sized machines. A great deal of this size reduction can be attributed to reasons discussed in [22]: the lack of rotor ohmic losses; the machines do not have rotor windings of any sort.

In these machines, magnets can either be attached to the surface or embedded within of the rotor; an example of the embedded style, an interior permanent magnet machine, is a machine studied in this dissertation, Figure 2.3. In the case of the magnets being embedded in the rotor, the inductance is not uniform along the angle of the machine rotor. Machine axes are defined as from the center of the rotor to its outermost edge. There are two main axes: the axis which coincides with the center of the magnet flux and the axis which coincides with the point between the positive and negative fluxes. For reference, note that the positive flux is defined to be the ‘north’ pole or the area in which the flux lines exit the rotor. The d-axis coincides with the middle of the magnet. Through the magnet, a field line along this path would have a large reluctance to cross, since the permeability of the magnet is that of air, which is much smaller than that of the steel which makes up the rest of the rotor.

The machine can be modeled by the phase equations in (2.1). Note that the $e_{a,b,c}$ quantities correspond to the back-EMF induced in the machine by the magnets. In the IPM machine discussed previously, the difference in permeability of the magnet in comparison with the steel path give rise to the problem of nonuniform inductance. Thus, it makes more

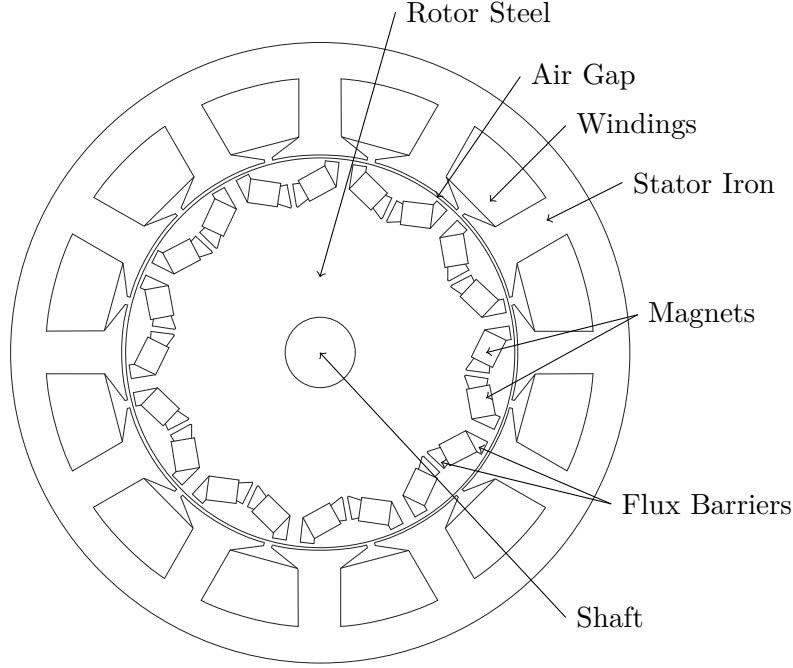


Figure 2.3: Permanent magnet synchronous machine with rotor designed for use in the demagnetization testing

sense to develop the equations of the machine in a new two phase frame of reference. This two phase frame of reference is defined to be the axes which align with the magnets and perpendicular to it, so that the inductance in each of these two phases is constant in all cases. This reference frame is defined as the rotor frame of reference.

$$\begin{bmatrix} v_{as} \\ v_{bs} \\ v_{cs} \end{bmatrix} = \begin{bmatrix} R_s & 0 & 0 \\ 0 & R_s & 0 \\ 0 & 0 & R_s \end{bmatrix} \begin{bmatrix} i_{as} \\ i_{bs} \\ i_{cs} \end{bmatrix} + \frac{d}{dt} \begin{bmatrix} L_{aa} & L_{ab} & L_{ac} \\ L_{ba} & L_{bb} & L_{bc} \\ L_{ca} & L_{cb} & L_{cc} \end{bmatrix} \begin{bmatrix} i_{as} \\ i_{bs} \\ i_{cs} \end{bmatrix} + \begin{bmatrix} e_{as} \\ e_{bs} \\ e_{cs} \end{bmatrix} \quad (2.1)$$

The rotor oriented frame of reference for an interior permanent magnet machine is not aligned to the stator, or fixed axes, but the moving, or rotor axes. In particular, it is oriented with the rotor magnet flux axis. The end goal is to have the system be aligned such that the

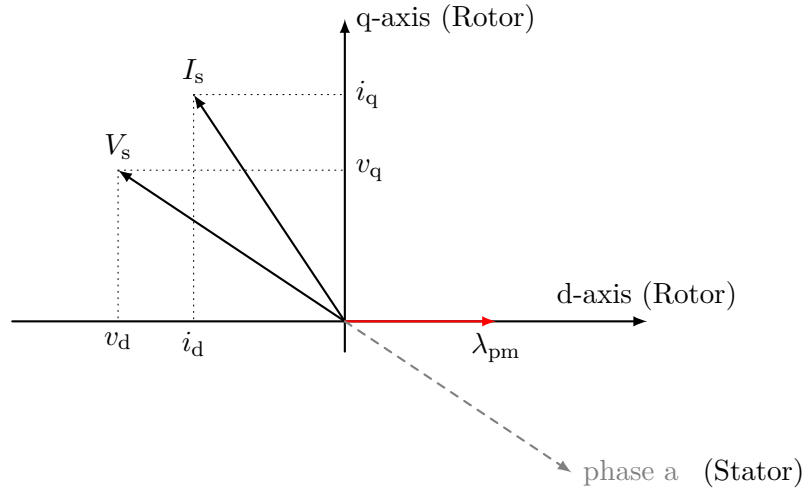


Figure 2.4: Stator phase axes and the rotor oriented axes

horizontal axis aligns with the middle of the magnet flux. This axis is designated the direct axis. The vertical axis is then set to be ninety degrees ahead of this direct axis, and should be ninety degrees ahead of the maximum positive magnet flux point and ninety degrees behind the maximum negative flux point. Note the axes given in Figure 2.4, and shown on an example machine in Figure 2.5. Not shown are the α and β axes; they are the horizontal and vertical axes in the stator frame of reference. These do not change position as the machine moves, and are aligned to the machine such that the horizontal axis is in line with the flux developed by the machine with only a positive phase A current. The β axis is defined as ninety degrees ahead of this.

Note that the north pole of the magnet is not in alignment with the a axis, due to the rotation of the rotor. Instead, the d-axis is always aligned with the rotor pole of the magnet to maintain alignment with the positive flux of the magnet. Thus, if a stator current were applied in alignment with the d-axis, flux would be applied in a direction which strengthens the flux in the machine, while applying a negative d-axis current would weaken the flux. Further, applying a quadrature axis current would induce torque in the machine with a

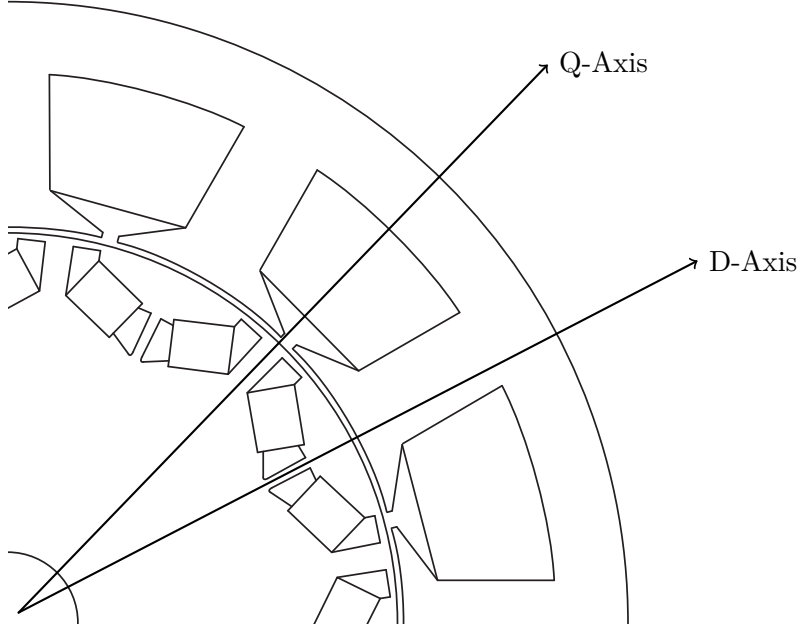


Figure 2.5: Physical illustration of stator and rotor oriented machine axes.

relationship to the rotor oriented axes as in equation (2.2). The value of operating the machine in this coordinate system can be seen by the simplicity of the torque equation.

$$T = \frac{3}{4}P [\lambda_{af} + (L_d - L_q)i_{ds}] i_{qs} \quad (2.2)$$

The final issue remaining is the application of rotor oriented axis current. This can be done with knowledge of the proper rotor oriented quantities desired, and then applying a transformation (2.4) to achieve the appropriate stator oriented quantities. By doing this, the controllers regulate constant quantities, reducing the bandwidth requirement of the controller.

$$\begin{bmatrix} x_a \\ x_b \\ x_c \end{bmatrix} = \begin{bmatrix} T_{abc} \end{bmatrix}^{-1} \begin{bmatrix} x_q \\ x_d \\ x_0 \end{bmatrix} \quad (2.3)$$

$$\begin{bmatrix} T_{abc} \end{bmatrix} = \begin{bmatrix} \cos(\theta_r) & \cos(\theta_r - \frac{2\pi}{3}) & \cos(\theta_r + \frac{2\pi}{3}) \\ \sin(\theta_r) & \sin(\theta_r - \frac{2\pi}{3}) & \sin(\theta_r + \frac{2\pi}{3}) \\ 1/2 & 1/2 & 1/2 \end{bmatrix} \quad (2.4)$$

With this understanding, the machine is modeled by equations in this rotor frame of reference as in (2.5)-(2.8).

$$v_d = i_d R_s + \frac{d\lambda_d}{dt} - \omega_e \lambda_q \quad (2.5)$$

$$\dots = i_d R_s + L_d \frac{di_d}{dt} - \omega_e L_q i_q \quad (2.6)$$

$$v_q = i_q R_s + \frac{d\lambda_q}{dt} + \omega_e \lambda_d \quad (2.7)$$

$$\dots = i_q R_s + L_q \frac{di_q}{dt} + \omega_e \lambda_{af} + \omega_e L_d i_d \quad (2.8)$$

The machine equations relate the current and voltage with the resistances, inductances and the flux linkage due to the magnets. The resistance R_s is simply the resistance of the phase, L_d is the inductance of the path through the direct axis, L_q is the inductance of the path through the quadrature axis, and the λ_{af} is the flux which links the stator due to the magnets.

2.2.1 Machine Model Considering Saturation and Cross-Saturation

The machine model parameters are not shown as functions in equation (2.5). In reality, these parameters vary during operation. The resistance is the most obvious, depending upon the temperature of the machine at any given point as well as the frequency applied to the machine due to the skin effect. The flux linkage due to the magnets can change slightly due to saturation of the iron of the machine as well as temperature. The main

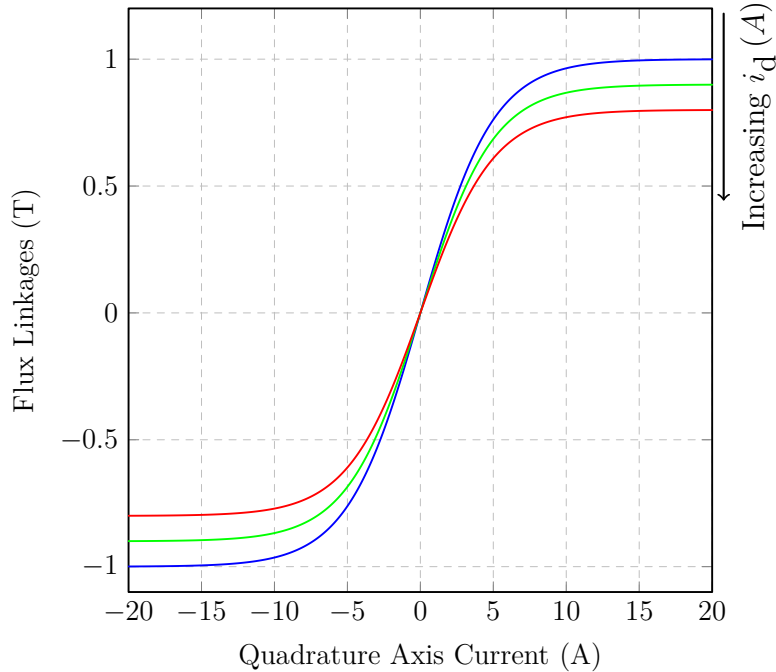


Figure 2.6: A generalized flux linkage with respect to current is shown for different current values.

components that change are the inductances. The L_d can change slightly due to saturation and cross-saturation, but because the equivalent airgap and reluctance are both large, the current required to saturate that axis can be quite high. In addition, one must apply positive i_d to saturate the machine easily, which is not often done in the control of IPM machines. Because the magnets are embedded, the airgap can become very small. Because of this, when current is applied, much more flux is developed. Because more flux is developed, the machine will saturate rapidly with increasing applied current, especially for the low reluctance Q-axis. This saturation caused by the high level of flux, especially in an IPM machine, is a typical source of variation in the parameters. The typical quadrature axis flux curve shows saturation at large current quantities in Figure 2.6.

Beyond the effect of mere saturation, cross saturation can lead to a reduction in flux in

that axis. This is especially true for the quadrature axis with large quadrature axis currents and direct axis currents. This curve in Figure 2.6 also shows decreasing quadrature axis flux with respect to direct axis current. The saturation changes which affect the machine model can be represented by a machine model which depends on both axis currents as in equations (2.9)-(2.12).

$$v_d = i_{ds}R_s + \frac{d\lambda_d(i_{ds}, i_{qs})}{dt} - \omega_e\lambda_q(i_{ds}, i_{qs}) \quad (2.9)$$

$$\dots = i_{ds}R_s + L_d(i_{ds}, i_{qs})\frac{di_{ds}}{dt} - \omega_eL_q(i_{ds}, i_{qs})i_{qs} \quad (2.10)$$

$$v_q = i_{qs}R_s + \frac{d\lambda_q(i_{ds}, i_{qs})}{dt} + \omega_e\lambda_d(i_{ds}, i_{qs}) \quad (2.11)$$

$$\dots = i_{qs}R_s + L_q(i_{ds}, i_{qs})\frac{di_{qs}}{dt} + \omega_e\lambda_{af} + \omega_eL_d(i_{ds}, i_{qs})i_{ds} \quad (2.12)$$

2.2.2 Machine Parameter Determination

In order to design a controller, the machine parameters must be known. These parameters can be determined in a variety of ways, with varying levels of accuracy. The simplest methods are motor standstill techniques, which apply a voltage or current to a machine and measure the rise time to determine the inductance and steady state relation to determine resistance. The flux linkage due to the magnets as well as d- and q- axis flux linkage with applied current must however be calculated by rotating the machine at a constant speed.

The simplest parameter to determine is the resistance of the machine. The measurement does not require the rotor to be moving, and this requires no other parameters. The resistance is measured as in [20] by applying a current to phase A, with the return current coming through the parallel combination of phases B and C. Apply a current for both the rated

machine current and 150% the rated machine current. At each current measure the voltage and apply the relationship in equation (2.13).

$$R_a = \left(\frac{2}{3}\right) \frac{V_{150\%} - V_{100\%}}{I_{150\%} - I_{100\%}} \quad (2.13)$$

The flux linkage due to the magnets is also an easy parameter to measure accurately, without requiring any other machine parameters. The back-EMF is the voltage induced by the flux linkage of the magnets. As such, if the machine is open circuited, and the voltage is measured while spinning the machine at constant speed, the flux linkage due to the magnets can be determined. If the line-to-line voltage and speed are precisely applied, the relationship in equation (2.16) is derived from the machine equations with current zero in equations (2.14) and (2.15).

$$v_d = 0 \quad (2.14)$$

$$v_q = \lambda_{af}\omega_e \quad (2.15)$$

$$\lambda_{af} = \frac{V_{l-1,rms}}{\Omega \frac{\pi P \sqrt{3}}{60\sqrt{2}}} \quad (2.16)$$

The resistance and flux linkage due to the magnets are the simplest parameters to calculate due to the simplicity of these tests. The inductance has a similar simple method which is found from a short circuit test on the machine operating at or above the base speed. The machine equations in the short circuit test simplify such that the only current is due to the flux linkage of the magnets, and that this current is in the direct axis. While the machine terminals are shorted and the RMS phase current is measured, the direct axis inductance can be determined as in equation (2.17) if the flux linkage due to the magnets is known, as

the induced current is limited by the inductance L_d .

$$L_d = \frac{\lambda_{af}}{i_{sc}\sqrt{2}} \quad (2.17)$$

This direct axis inductance is an excellent measure of inductance if the machine has surface mounted magnets. In this case, the inductances are typically equal in both axes and saturation has little effect due to the large airgap. The assumption of no saturation is insufficient with the IPM machines due to the fact that it measures only the direct axis inductance at one point, at a high current level in the machine. In an IPM motor, this would mean calculating the direct axis inductance, and not having information on either the quadrature axis inductance or the effects of both currents on this quadrature axis inductance value. The aforementioned tests solve this by applying a voltage at standstill and measuring the rise time; the rise time method is the classical inductance determination tool.

In order to take into account all current combinations and actual operating conditions, the most accurate characterization method is that of the steady state dynamic characterization. The main method used for inductance calculation has the machine spin at a constant speed while a constant current vector is applied to the machine, primarily a representative set of current vectors in the second quadrant as shown in Figure 2.7. This application is shown in the characterizing current and drive blocks of Figure 2.8. With knowledge of the resistance and flux linkage due to the magnets, the voltage is measured and the flux linkages then calculated, as shown in the characterization block. This flux linkage depends on both currents and can thus be used for controller development with parameters which will match machine performance during operation as in [35].

Having the machine move at constant speed with a constant current vector will remove

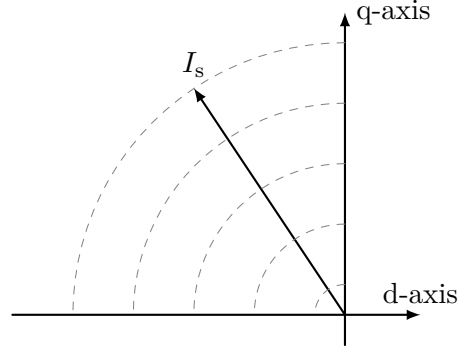


Figure 2.7: Multiple current vectors applied during the characterization scheme

the derivative terms for the currents from equations (2.5)-(2.8), and thus of fluxes in equation (2.18).

$$\begin{aligned}
 v_d &= i_{ds}R_s - \omega_e\lambda_q \\
 v_q &= i_{qs}R_s + \omega_e\lambda_d
 \end{aligned}
 \tag{2.18}$$

With the resistance known, the flux depending on both currents can be found from equation (2.19).

$$\begin{aligned}
 \lambda_q(i_{ds}, i_{qs}) &= \frac{v_d - i_{ds}R_s}{-\omega_e} \\
 \lambda_d(i_{ds}, i_{qs}) &= \frac{v_q - i_{qs}R_s}{\omega_e}
 \end{aligned}
 \tag{2.19}$$

With the machine parameters known, the controller depending on these parameters can be developed.

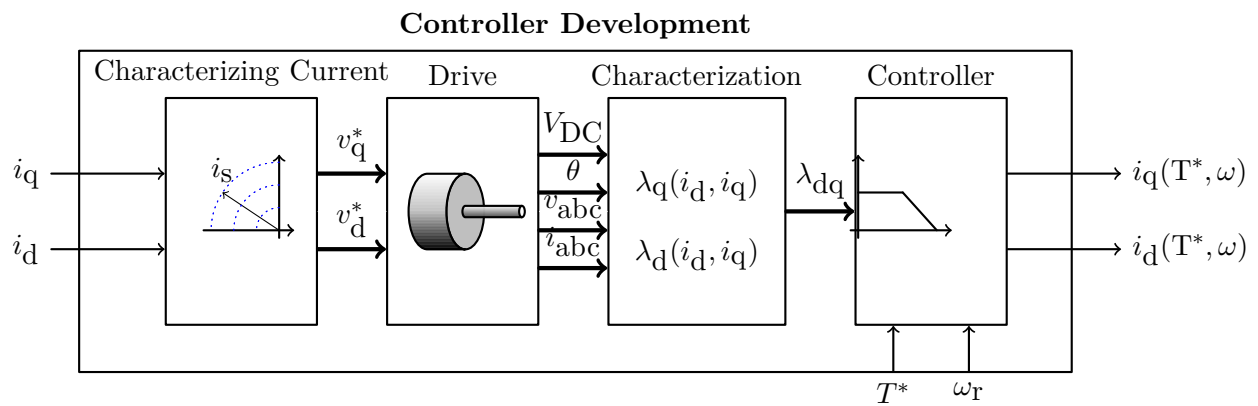


Figure 2.8: Data acquisition for controller development

Chapter 3

Inverter Condition Monitoring

3.1 Inverter Modeling

Inverter device modeling is discussed in this section. The relationship between the voltage and current of the devices in the inverter is found using the characterization method, and with this, the equivalent resistance in the saturation region of the device is calculated.

The semiconductor characteristics of interest in this work are the voltage drops. There are voltage drops between the anode-cathode (V_d) and collector-emitter (V_{CE}), for the diodes and IGBTs, respectively. This voltage drop is nonlinear; the solid line in Figure 3.1 is a generalized example of this. The dotted line is a linear approximation of this, $V = V_{fw} + IR$. There are two regions of the solid curve: the saturation (linear) region at high currents, and the nonlinear region at low currents.

In order to determine the type of fault present, the relationship between the fault and voltage drop must be known. The characteristic of interest here is the IGBT voltage, V_{CE} , although this applies for the diode voltage, too. The collector-to-emitter voltage equation in the saturation region [30],

$$V_{CE,sat} = V_{p+n-} + V_B + V_{MOS} + V_{bondwire}, \quad (3.1)$$

is modeled by the sum of four voltages:

1. The junction drop (V_{p+n-}),
2. the voltage drop across the lightly doped storage region (V_B),
3. the voltage drop over the space charge region (V_{MOS}), and
4. the ohmic voltage drop due to the bond wire ($V_{bondwire}$).

The resistance was shown to change with BWLO in [46], which is clear from the resistance in $V_{bondwire}$ of $V_{CE,sat}$,

$$V_{bondwire} = I_C R = I_C R_{20} (1 + \alpha_{20}(\theta - 20)) . \quad (3.2)$$

The bondwire voltage is the ohmic drop due to the wires bonded to the semiconductor. If some of the bonds lift, the resistance will increase; thus, the resistance is used to detect faults.

The resistance found with the characterization results is used to determine if the bond wires have lifted. The resistance is determined from the nonlinear characterization results curve. The resistance is defined as the slope ($R = \Delta V / \Delta I$) in the linear region of the voltage curve.

3.1.1 Representing the Semiconductor Voltage Drop

A series of tests is used to determine the entire voltage-current relationship of the device. Current is applied to each of the devices and the device voltages are determined from measurements.

There are four characteristics which define the nonlinearity: The resistance (R_d , differential resistance of linear region) and forward biased junction voltage ($V_{th,d}$) over the diode, as well as the resistance (R_i , differential resistance of linear region) and forward biased junction

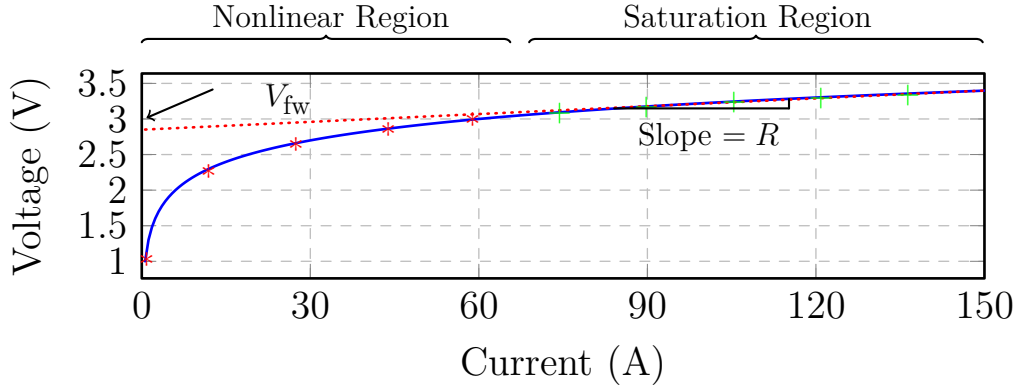


Figure 3.1: Waveforms showing a generalized semiconductor nonlinearity, given as its voltage-current characteristics and the linear approximation to this with its equivalent parameters; this is the key characteristic for a device.

voltage ($V_{th,i}$) over the IGBT. These quantities form a linear approximation to the device nonlinearity, as shown in Figure 3.1. The linear region begins where the linear approximation and actual characteristic curve are close. This varies by device, and it is assumed to be where the differential resistance becomes less than twice its final value in Figure 3.1, at roughly 125 A (The differential resistance decreases with current.) This linear approximation is helpful for simplification and to determine the saturation behavior of the device, but the nonlinear area below this is also important to fully characterize the device behavior.

Any characterization method requires that the device voltages be calculated from the phase voltage measurements. With the phase and DC link voltage sensors shown in Figure 3.3, the information required to characterize the devices is available, as shown in the next section.

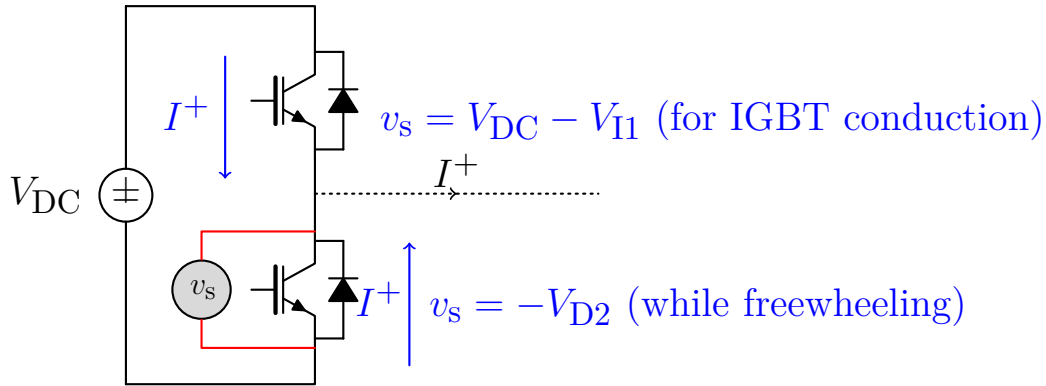


Figure 3.2: The phase A half bridge of the inverter, showing the sensor connection. The purpose of this figure is to demonstrate the paths of current, and how they relate to the voltage measured by the voltage sensor.

3.1.1.1 Expression for Voltage Drop with Direct Load Current

An analytic expression for the voltage drop with direct load current is derived using the discussed sensor placement. These sensors are shown to be sufficient for characterization using the following situation: assume phase A of the inverter conducts a positive current into the load. When the switching command for phase A is high, the top IGBT conducts; when low, the bottom diode conducts (freewheels). These two paths are illustrated in Figure 3.2. When the bottom diode is conducting during freewheeling, the voltage measured will be the bottom diode voltage with a negative sign. When the IGBT is conducting, the voltage will be that of the DC link, less the IGBT voltage drop. The IGBT voltage drop can therefore be calculated using $V_{DC} - V_{A \rightarrow DCN}$.

The measured voltage $V_{A \rightarrow DCN}$ resembles the waveform in Figure 3.4(a) for positive current ($V_{A \rightarrow DCN}^{DC+}$). The negative current case is given in Figure 3.4(b). The effect of the DC-link should be removed, to isolate the diode and IGBT voltages. This is only discussed for the positive load current case; the DC link voltage is removed and the resulting square wave

made to intersect with 0 V, with the positive and negative values corresponding to the IGBT and diode, respectively. When this square wave is high, the DC link voltage is subtracted from the value and the result negated; when low, nothing is done. The removal of DC link voltage and negation when high results in the waveform shown in Figure 3.4(c). The values between the positive and negative maximum areas are ignored. The modified waveform is referred to as the semiconductor voltage drop, V_{sdrop} , and is used for the subsequent analysis. The waveforms for the positive and negative cases will take the following shape: for the positive current case, the square wave positive value should be V_{I1} and the square wave negative value should be $-V_{D2}$; for the negative current case, the square wave positive value should be V_{I2} and the square wave negative value should be $-V_{D1}$.

The analytic expressions for the measured phase A voltage with positive direct load current, $V_{A \rightarrow \text{DCN}}^{\text{DC}+}$, and measured voltage with negative load current, $V_{A \rightarrow \text{DCN}}^{\text{DC}-}$, are found first. The two expressions are then combined into the complete phase A measured voltage expression with applied DC current, $V_{A \rightarrow \text{DCN}}^{\text{DC}}$. In Figure 3.4(a), $V_{A \rightarrow \text{DCN}}^{\text{DC}+}$ is plotted; only the voltage for the top IGBT of phase A (IGBT1/I1) and the bottom diode of phase A (diode2/D2) is measurable. The analytic expression for $V_{A \rightarrow \text{DCN}}^{\text{DC}+}$ is given for $0 \leq t < T_c$ by equation (3.3) as a pulsetrain waveform with a constant duty cycle. In Figure 3.4(b), $V_{A \rightarrow \text{DCN}}^{\text{DC}-}$ is plotted; for this case the bottom IGBT of phase A (IGBT2/I2) and the top diode of phase A (diode1/D1) voltage is measurable. The analytic expression for $V_{A \rightarrow \text{DCN}}^{\text{DC}-}$ is given by equation (3.4). Equation (3.5), $V_{A \rightarrow \text{DCN}}^{\text{DC}}$, is found from $V_{A \rightarrow \text{DCN}}^{\text{DC}+}$ and $V_{A \rightarrow \text{DCN}}^{\text{DC}-}$.

$$\begin{aligned}
V_{A \rightarrow DCN}^{DC+}(t) &= [V_{DC} - V_{I1}(i_a)] u(t) \\
&\quad - [(V_{DC} - V_{I1}(i_a)) + V_{D2}(i_a)] u(t - DT_c)
\end{aligned} \tag{3.3}$$

$$\begin{aligned}
V_{A \rightarrow DCN}^{DC-}(t) &= [V_{DC} + V_{D1}(i_a)] u(t) \\
&\quad + [V_{I2}(i_a) - (V_{DC} + V_{D1}(i_a))] u(t - DT_c)
\end{aligned} \tag{3.4}$$

$$\begin{aligned}
V_{A \rightarrow DCN}^{DC}(t) &= V_{A \rightarrow DCN}^{DC+}(t) \left\{ \frac{1}{2}(\text{sgn}(i_a) + 1) \right\} \\
&\quad + V_{A \rightarrow DCN}^{DC-}(t) \left\{ \frac{1}{2}(1 - \text{sgn}(i_a)) \right\}
\end{aligned} \tag{3.5}$$

If V_{DC} varies, this has a negative effect on the accuracy of calculation result. By measuring V_{DC} and removing the effect, equations (3.3) and (3.4) become equations (3.6) and (3.7). V_{sdrop} , previously discussed, is the voltage drop over the inverter semiconductors; this is the

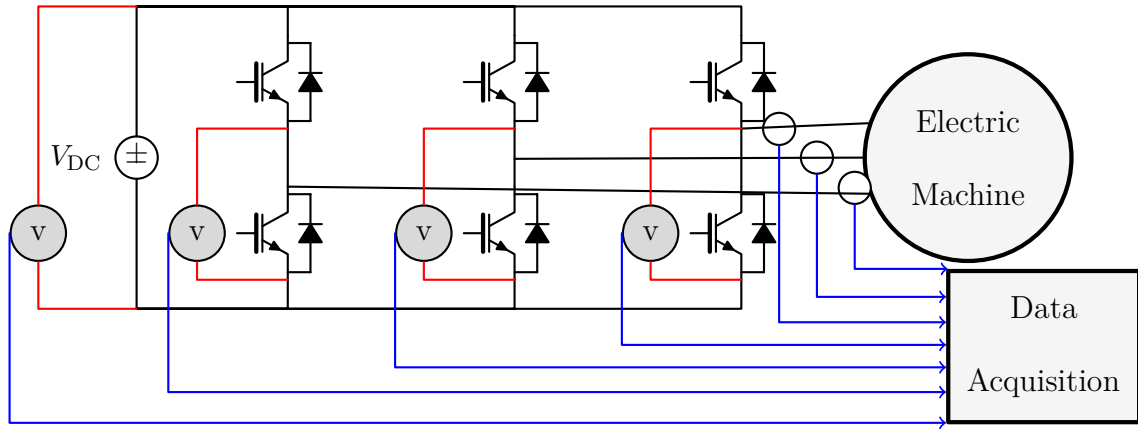
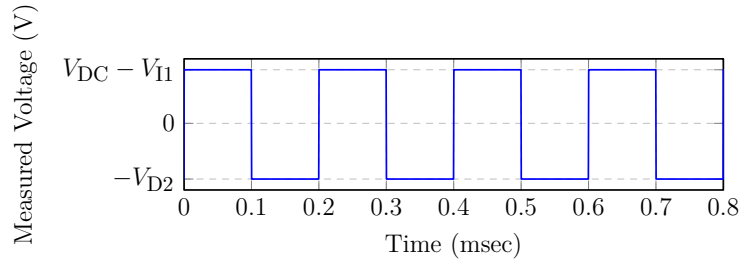
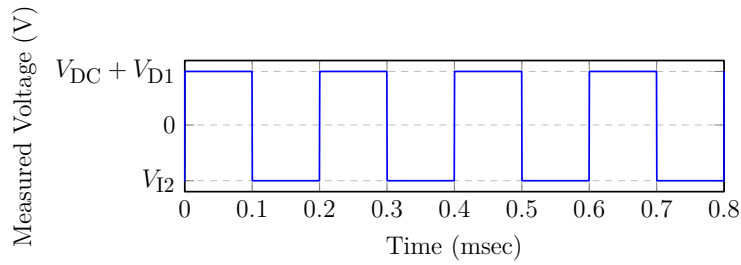


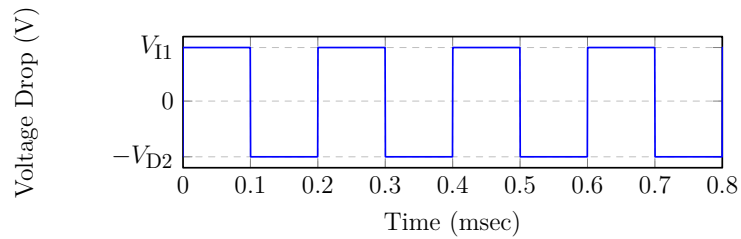
Figure 3.3: The experimental setup for inverter characterization is shown with the line-to-DCN voltage sensors.



(a) The voltage measured from phase A to the negative DC link with positive current, $V_{A \rightarrow DCN}^{DC+}$.



(b) The voltage measured from phase A to the negative DC link with negative current, $V_{A \rightarrow DCN}^{DC-}$.



(c) Extracted semiconductor device voltage drop representation, V_{sdrop}^{DC+} , used in analysis.

Figure 3.4: Representations of the voltages measured with the sensor configuration in Figure 3.3

voltage used hereafter.

$$\begin{aligned}
V_{\text{sdrop}}^{\text{DC}+}(t) &= [V_{\text{I1}}(i_a)] u(t) - \\
&\quad [V_{\text{I1}}(i_a) + V_{\text{D2}}(i_a)] u(t - DT_c)
\end{aligned} \tag{3.6}$$

$$\begin{aligned}
V_{\text{sdrop}}^{\text{DC}-}(t) &= [V_{\text{I2}}(i_a)] u(t) - \\
&\quad [V_{\text{I2}}(i_a) + V_{\text{D1}}(i_a)] u(t - DT_c)
\end{aligned} \tag{3.7}$$

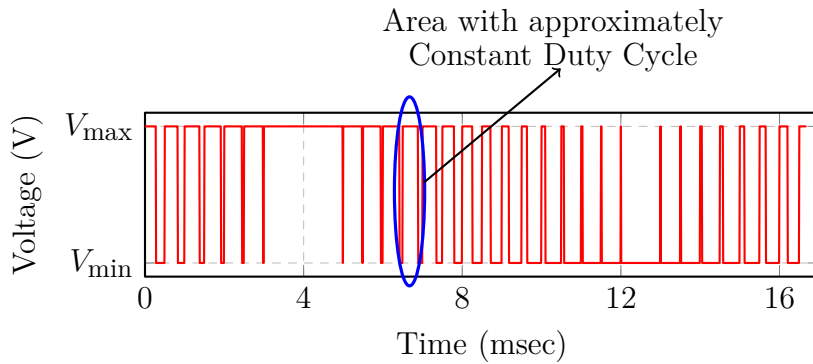
3.1.1.2 Expression for Voltage Drop with Alternating Load Current

In most applications, alternating currents are applied to the machine. This necessitates an AC waveform representation, $V_{\text{A} \rightarrow \text{DCN}}^{\text{AC}}$, to which there are two approaches. The first is representing $V_{\text{A} \rightarrow \text{DCN}}^{\text{AC}}$ analytically as was done with $V_{\text{A} \rightarrow \text{DCN}}^{\text{DC}}$. The second assumes that $V_{\text{A} \rightarrow \text{DCN}}^{\text{AC}}$ is a succession of “ $V_{\text{A} \rightarrow \text{DCN}}^{\text{DC}}$ -like” signals.

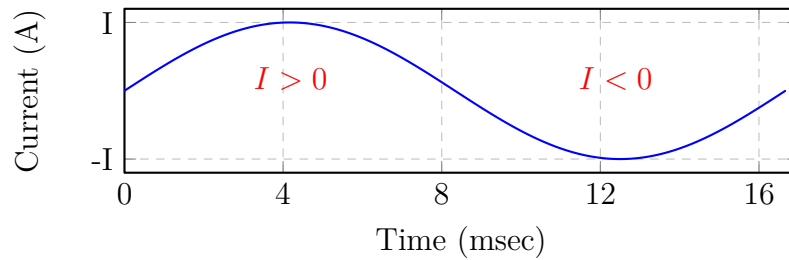
In equation 3.8 [41], an analytic expression of a pulse train whose duty cycle is modulated with a sinusoid is developed using Bessel functions. A microcontroller cannot calculate the spectrum quickly, as the spectrum calculation requires the sum of many Bessel functions to be accurate, thus this approach is not taken.

$$\begin{aligned}
&V_{\text{A} \rightarrow \text{DCN}}^{\text{AC}}(t, M, f_1, V_{\text{DC}}, V_{\text{I1}}, V_{\text{I2}}, V_{\text{D1}}, V_{\text{D2}}, i_a, f_c) \\
&= \left\{ \frac{1}{2}(\text{sgn}(i_a) + 1) \frac{V_{\text{DC}} - V_{\text{I1}} - V_{\text{D2}}}{2} + \frac{1}{2}(-\text{sgn}(i_a) + 1) \frac{V_{\text{I2}} - V_{\text{D1}} - V_{\text{DC}}}{2} \right\} \left\{ M \sin(2\pi f_1 t) \right. \\
&\quad \left. + \sum_{k=1}^{\infty} \frac{2}{k\pi} [1 - (-1)^k J_0(k\pi M)] \sin(2\pi k f_c t) \right. \\
&\quad \left. - \sum_{k=1}^{\infty} (-1)^k \sum_{n=1}^{\infty} \frac{J_n(k\pi M)}{k\pi} [\sin(2\pi(k f_c - n f_1)t) + (-1)^n \sin(2\pi(k f_c + n f_1)t)] \right\} \\
&+ \frac{1}{2}(\text{sgn}(i_a) + 1) \frac{V_{\text{DC}} - V_{\text{I1}} - V_{\text{D2}}}{2} + \frac{1}{2}(-\text{sgn}(i_a) + 1) \frac{V_{\text{I2}} + V_{\text{D1}} + V_{\text{DC}}}{2}
\end{aligned} \tag{3.8}$$

The second approach approximates $V_{\text{A} \rightarrow \text{DCN}}^{\text{AC}}$ as shown in Figure 3.5(a) as many DC



(a) Simulated inverter phase voltage.



(b) Simulated inverter phase current corresponding to 3.5(a).

Figure 3.5: $V_{A \rightarrow DC}$ - measurement for an AC waveform showing the relationship between current and the measured PWM voltage. The voltages are: $(V_{\min}, V_{\max}) = (-V_{D2}, V_{I1})$ when current is positive, and $(V_{\min}, V_{\max}) = (-V_{D1}, V_{I2})$ when current is negative.

waveforms, like that in Figure 3.4(c). Figure 3.5(b) gives the corresponding current, because this contains both positive and negative currents, all devices in that phase can be measured with this one test. Further, as long as the amplitude of the current is high enough to saturate the semiconductors, the phase leg can be completely characterized. The ACPWM signal, a pulse train with time-varying duty cycle in Figure 3.5(a), is viewed as a succession of constant duty cycle waveforms; one area of constant duty cycle is marked in Figure 3.5(a). Equation (3.5) is used to model the voltage in the constant duty cycle area.

3.1.2 Inverter Fault Monitoring

It is necessary to build a simple BWLO model to show the benefits of applying inverter characterization to condition monitoring. The device resistance is used to determine the number of attached bonds; by observing the resistance in time, any bond lifts that occur can be detected. The chips have a structure where each chip's emitter has multiple bond wires attached to it, while the collectors are usually connected with solder at the chip-level. These connectors form a parallel connection, shown in Figure 3.6, between the external emitter connection and the chip with a resistance of $R = R_{\text{bond}}/m$ where m is the number of wire bonds connected to the chip. This means that as each connector breaks, the resistance increases. Furthermore, it is typical for different chips to be connected in parallel, but this does not change the fact that the resistance depends on the m term, the number of bonds for all chips in parallel for a given phase.

Experiments are performed by controlling current in an induction machine using the SEMIKRON SKiiP 2 (SkiiP 342GDL 120-4DU) inverter; currents of different magnitudes are applied, 0 A, 10 A, . . . 150 A, and frequencies, 60 Hz, 120 Hz, and 180 Hz; this is done for

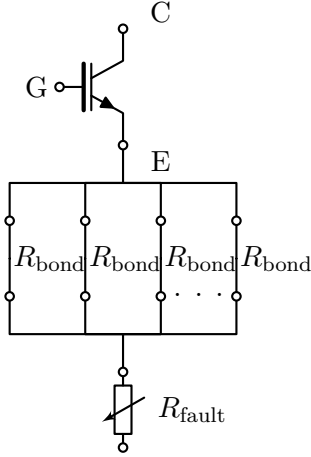


Figure 3.6: IGBT with bond wires and the added fault resistance

Table 3.1: Experimental resistances added

	Nominal	$R_{\text{fault}0}$	$R_{\text{fault}1}$	$R_{\text{fault}2}$	$R_{\text{fault}3}$
R_{fault}	0 m Ω	4 m Ω	13 m Ω	17 m Ω	24 m Ω

different fault levels.

To get the faulted case data, a resistance is added in series with phase A as shown in Figure 3.6. The phase A voltage is then used for the generation of harmonic information. Voltage measurements shown in Figure (3.2) are used for characterization while 150 A AC is applied. In the experimental case here, the resistances in Table 3.1 are added to test the diagnostic methods.

3.1.3 Thermal Model of Inverter

When using the Arrhenius relationship to model the time to BWLO, it is important to accurately measure the junction temperature. Using the thermal model parameters given in Tables 3.2 and 3.3, the Cauer thermal model computes the temperatures for use in the

Arrhenius model [24]. The losses in the switches are given by the datasheet with respect to the current in that phase.

Table 3.2: Thermal model from the device losses for the IGBTs, diodes and module between the surface of the device (s) and the ambient (a)

$R_{th(j-s)I}$	per IGBT	0.09	K/W
$R_{th(j-s)D}$	per diode	0.25	K/W
$R_{th(s-a)}$	per module	0.036	K/W

Table 3.3: The thermal model from the datasheet between the device junctions (j), the sensor (r) and the ambient (a)

Z_{th}	R_i (mK/W) (max vals)				τ_i (s)			
	1	2	3	4	1	2	3	4
Device:	1	2	3	4	1	2	3	4
$Z_{th(j-r)I}$	10	69	11	0	1	0.13	0.001	1
$Z_{th(j-r)D}$	28	193	30	0	1	0.13	0.001	1
$Z_{th(r-a)}$	1.7	24	7.6	2.6	494	165	20	0.03

Under normal conditions, the current the device delivers to or from the load defines the amount of losses. This assumes a healthy device resistance. In the faulted mode, the resistance increases according to the number of lifted bonds. If half of the bonds are lifted for instance, this translates to the doubling of the equivalent resistance. Thus, the losses used in the model will double because the current remains the same; the losses in the thermal model are doubled. This study assumes that bond lifting results in an increased resistance; the resistances added to the nominal to simulate the fault are those in Table 3.1. Also note that each device does not conduct at all times, given that the induction machine is driven

with an AC current. Each device in a given phase conducts roughly a quarter of the time. There are two reasons for this: each phase conducts in the positive and negative directions for equal amounts of time and the duty cycle for each IGBT/diode pair is on average 50%, therefore the diode and IGBT conduct for equal amounts of time.

In order to run the thermal simulations, currents from torque given by the ECE 15 + EUDC driving cycle from the new European driving cycle handbook [3] are used. The cycle translates to 68 thermal cycles per day; the driving cycle has currents applied 34 times, during acceleration or deceleration, and is performed twice per day. This is done for the thermal model using actual measurements of the voltage drop over the devices with respect to current. This information allows for the calculation of the device junction temperatures.

3.1.4 Thermomechanical Model of Bond Wire Lift-off

In [49] temperature cycling is found to cause BWLO failure. Failure occurs when stress develops (ϵ_{tot}) in the bond wire connection as in equation (3.9) because of the different coefficients of thermal expansion, where the α -terms are the coefficients of thermal expansion for the respective materials, ΔT_j is the temperature cycling range and ν is the Poisson ratio for the device in the elastic range,

$$\epsilon_{\text{tot}} = \frac{(\alpha_{\text{Al}} - \alpha_{\text{Si}})\Delta T_j}{1 - \nu}. \quad (3.9)$$

With uniform temperature cycling, this results in the estimated number of thermal cycles to failure being $N_f \propto \epsilon_{\text{tot}}^{-\alpha}$, and with equation (3.9) this is $N_f \propto \Delta T_j^{-\alpha}$. Using the Arrhenius

relationship from experimentally acquired data, the RUL in the number of cycles is given by

$$N_f = A\Delta T_j^{-\alpha} \exp \frac{E_a}{k_B T_m}. \quad (3.10)$$

This relationship is used to determine the number of thermal cycles until failure, where $A = 648000$, $\alpha = 5$, $E_a = 9.89 \times 10^{-20} \text{ J}$ and $k_B = 1.38 \times 10^{-23} \frac{\text{J}}{\text{K}}$ [4]. Knowing the average number of cycles per any given time period, the failure rate is found with

$$\lambda^{-1}(\text{hour}) = \frac{\left(\frac{\text{cycles}}{\text{hour}}\right)}{N_f(\text{cycles})}. \quad (3.11)$$

3.2 Characterization of Inverter Devices

The representations for inverter semiconductor voltage drops are used to develop methods for inverter characterization. Direct load current is used to characterize the inverter devices. When a constant direct load current is applied, the semiconductor voltage drops for positive and negative current are given by equations (3.12) and (3.13). Characterization methods are introduced first analytically, then are verified with simulations and experiments.

$$\begin{aligned} V_{\text{sdrop}}^{\text{DC}+}(t) &= [V_{\text{I1}}(i_a)] u(t) - \\ &\quad [V_{\text{I1}}(i_a) + V_{\text{D2}}(i_a)] u(t - DT_c) \end{aligned} \quad (3.12)$$

$$\begin{aligned} V_{\text{sdrop}}^{\text{DC}-}(t) &= [V_{\text{I2}}(i_a)] u(t) - \\ &\quad [V_{\text{I2}}(i_a) + V_{\text{D1}}(i_a)] u(t - DT_c) \end{aligned} \quad (3.13)$$

3.2.1 Method Utilizing the Waveform Spectrum

The “spectral method” is described in this section. The Fourier spectrum of the PWM voltage was investigated to find the voltage drops, since, if no aliasing occurs, the spectrum should not contain high frequency noise. The measured semiconductor voltage drop in equation (3.14) is used to derive the analytic expression of the DFT in equation (3.15). N_p represents the number of positive samples of the PWM signal.

$$\begin{aligned} x[n] &= V_{I1}u[n] - (V_{I1} + V_{D2})u[n - (DN + 1)] \\ &= x[n + N] \end{aligned} \quad (3.14)$$

$$C_0 = \frac{(V_{D2} + V_{I1})N_p}{N} - V_{D2} \quad (3.15)$$

$$|C_k| = \frac{V_{D2} + V_{I1}}{N} \frac{\sin(\frac{\pi k N_p}{N})}{\sin(\frac{\pi k}{N})} \quad (3.16)$$

$$\begin{aligned} V_{D2} &= N_p C_1 \frac{\sin(\frac{\pi}{N})}{\sin(\frac{N_p \pi}{N})} - C_0 \\ V_{I1} &= N C_1 \frac{\sin(\frac{\pi}{N})}{\sin(\frac{N_p \pi}{N})} - V_{D2} \end{aligned} \quad (3.17)$$

The relationship between the device characteristics and harmonics is defined by this analytic representation of the DFT of V_{sdrop} . There are two unknowns with one equation. In this case two equations are found by selecting two harmonics and their respective equations: the fundamental and DC. The device characteristics can be computed with: these two equations, the number of samples, the duty cycle, as well as the DC and first harmonic values. For this method, the FFT must be computed by the inverter’s DSP or microcontroller at the DC

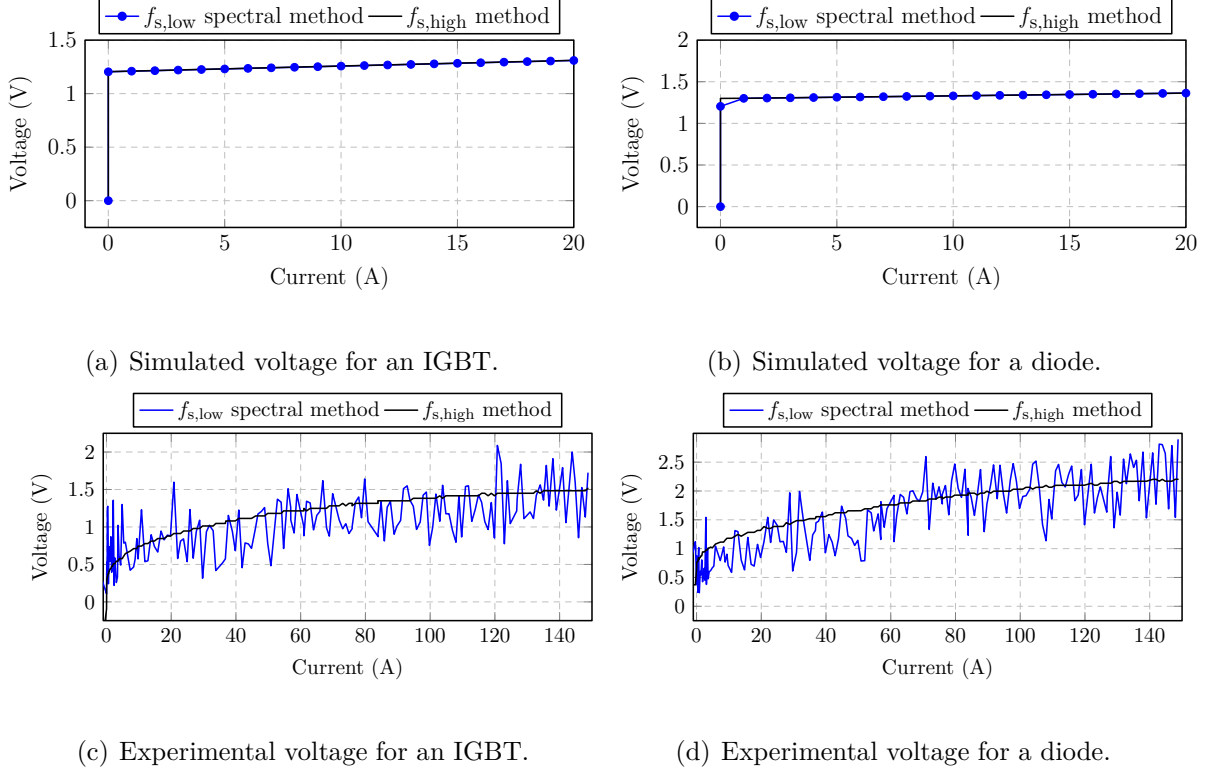


Figure 3.7: The resulting simulation and experimental waveforms for voltage with the spectrum method.

and fundamental switching frequency (5 kHz). The resulting characteristics of IGBT1 and diode2 are found with equation (3.17) and given in Figures 3.7(a) and 3.7(b) from simulations, and Figures 3.7(c) and 3.7(d) from experiments. This method can effectively estimate the nonlinearity for each device with minimal loss of precision due to noise.

Inverter characterization is accomplished by using alternating current in two ways. The first method, termed the “algorithm method”, uses measurements of the measured voltage signal and a simple algorithm to determine the device characteristics. The second approach uses a variation of the spectral method from this section using the knowledge of the approximately constant duty cycle in a local area. To test the performance of the proposed AC methods, the high sampling rate data are used with the algorithm method and the result filtered.

3.2.2 Characterization with Developed Algorithm

An “algorithm method” is developed to use the measured AC voltage with respect to the current to find the voltage-current relationship for each device. In Figure 3.5(a), the voltage of phase A is shown with respect to the current in Figure 3.5(b). This waveform contains voltage data for both directions of current, so it is possible to characterize the top and bottom IGBTs and diodes, as well as their respective freewheeling diodes.

If the current values are associated with their respective voltages, a model can be constructed for each device. In implementation, only integer valued currents are stored, by rounding all current readings to the nearest integer. Voltage readings taken at $1.5\text{ A} \rightarrow 2.49\text{ A}$ are averaged and stored for the 2 A point; this reduces the number of points in the model. Thus, the model will consist of two vectors: $(0\text{ A}, 1\text{ A}, \dots, I_{\max}\text{ A})$ and $(V_{0\text{ A}}\text{ V}, V_{1\text{ A}}\text{ V}, \dots, V_{I_{\max}\text{ A}}\text{ V})$.

Figure 3.8 shows the algorithm to find the appropriate voltage with respect to current. The inverter can be characterized by one AC point, if a sinusoidal current is applied which has a peak value within the saturation area of the IGBT and diode, as every intermediate current is also contained in that data.

The same setup as the DC methods is used, but with an AC of $150 A_{\text{peak}}$ applied. The results in Figure 3.9 match well to the verification method.

3.2.3 Method Using DC Approximation with STFT

A method using the spectrum of the voltage is proposed for use with AC current; this is termed the “AC spectral method”. The problem with applying the spectral method directly to the AC signal is that this method calculates the FFT for the entire time span; in the DC

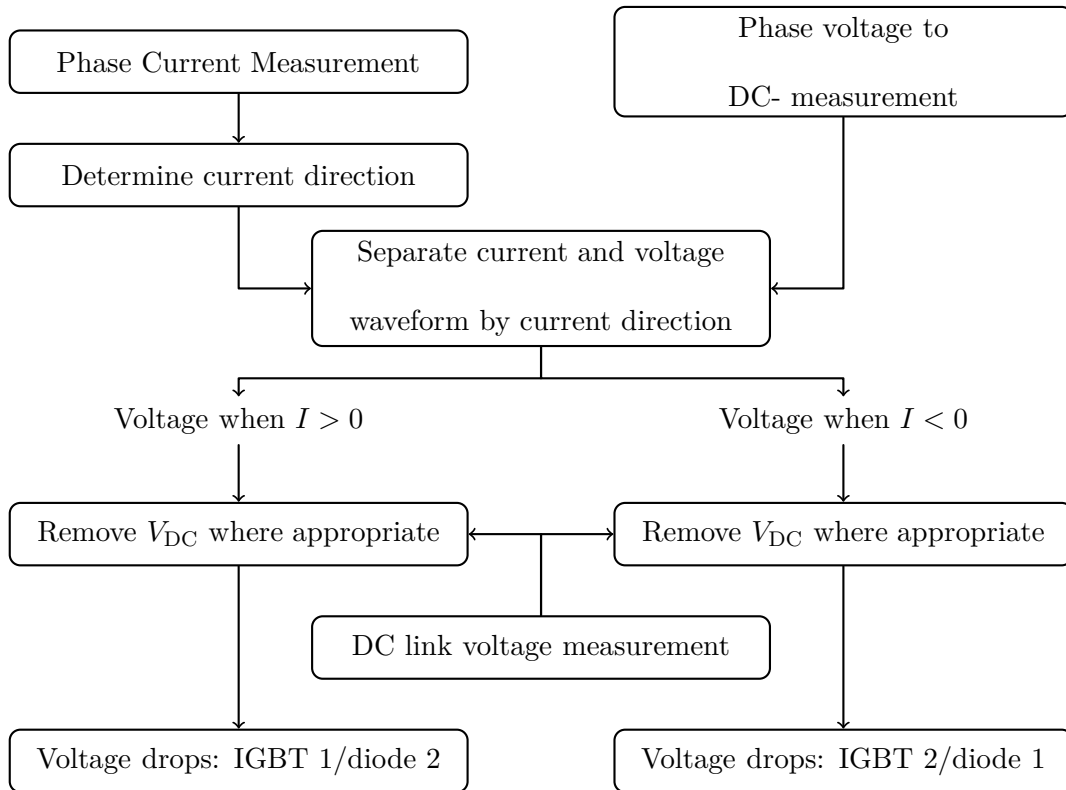
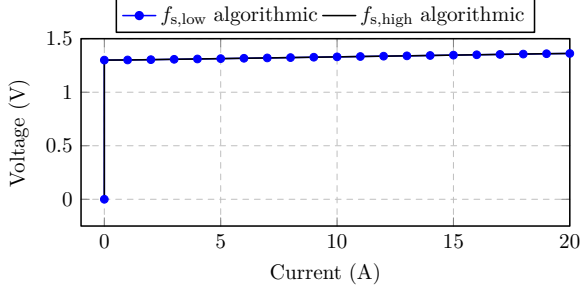
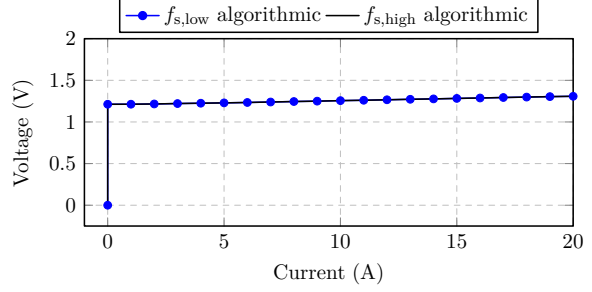


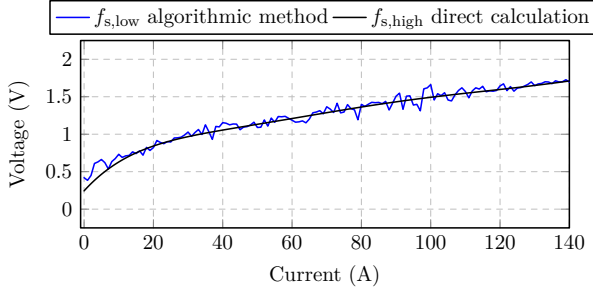
Figure 3.8: Characterization method used to determine the voltage and current relationship of inverter devices



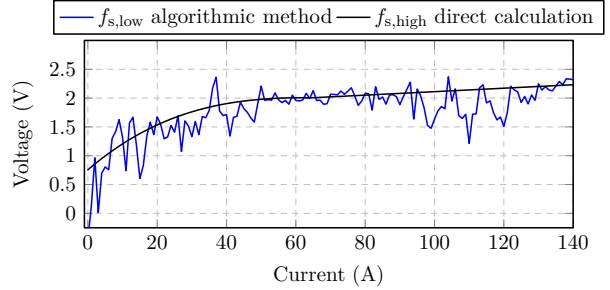
(a) Simulation IGBT characteristic curve.



(b) Simulation Diode characteristic curve.



(c) Experimental IGBT characteristic curve.



(d) Experimental Diode characteristic curve.

Figure 3.9: Results of voltage drop spectrum extraction.

case this is a stationary signal and thus appropriate. The harmonics of a stationary signal do not change in time; with the varying duty cycle waveform that results when measuring the voltage while alternating current is applied, this is not the case. It is possible to calculate the FFT of the entire signal, but the voltage-current relationship is lost, as the harmonics correspond to multiple currents.

Taking the FFT in a localized region, like that circled in Figure 3.5(a), would remedy this if the FFT is calculated for a local DC-like area with roughly constant current. This is possible with the short-time Fourier transform (STFT), shown in equation (3.18) [51].

$$\text{STFT}(t, f) = \int h(t - \tau) s(\tau) e^{-j2\pi f \tau} d\tau \quad (3.18)$$

The choice of window is important in this application, because it affects the calculation of the parameters. There is one main considerations when choosing a window function: the derivation of the DFT. Since the STFT with its respective window is shift-invariant, shifts

in the signal will not result in a different DFT result.

The simplest window is the rectangular one, with a magnitude of one for all samples within the window and zero otherwise. Normally this would introduce discontinuities at the edge of the window, but because a PWM waveform is already discontinuous, this is not relevant. The analytic derivation of the DFT is given in equations (3.21)-(3.23), where the DFT of two shift-instances given by equations (3.19)-(3.20) are determined for the situation where N samples are taken over one PWM period. The magnitude of the spectrum ends up being the same since the $x[n]$ waveform, the product of the window and the PWM waveform, is one over the nonzero indices.

$$x[n] = \begin{cases} 1, & \text{if } n = 0, 1, 2, 3, 4. \\ 0, & \text{otherwise.} \end{cases} \quad (3.19)$$

$$x[n-1] = \begin{cases} 1, & \text{if } n = 1, 2, 3, 4, 5. \\ 0, & \text{otherwise.} \end{cases} \quad (3.20)$$

The coefficients for the DFT are given by the following:

$$C_k = \sum_{n=0}^{N-1} x[n] \frac{e^{-jkn2\pi}}{N} = \sum_{n=0}^{N-1} x[n-1] \frac{e^{-jkn2\pi}}{N}, \quad (3.21)$$

$$C_k = \sum_{n=0}^4 \frac{e^{-jkn2\pi}}{N} = \sum_{n=1}^5 \frac{e^{-jkn2\pi}}{N}, \text{ and} \quad (3.22)$$

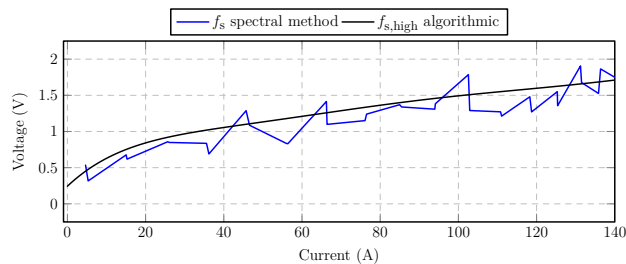
$$|C_k| = \frac{1}{N} \frac{\sin(kN_p \frac{\pi}{N})}{\sin(k \frac{\pi}{N})} = \frac{1}{N} \frac{\sin(kN_p \frac{\pi}{N})}{\sin(k \frac{\pi}{N})}. \quad (3.23)$$

When the values of the window are not constant and depend on n , $x[n]$, and therefore the analytic derivation of the DFT changes depending on where the waveform is sampled. If the

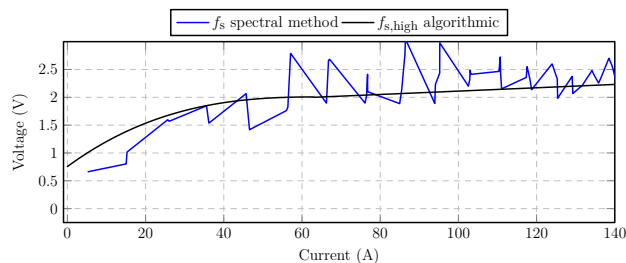
PWM waveform is shifted and this is multiplied by the window function the result changes; this would require the derivation of a new analytic DFT function. This is the drawback to using the default window in the *spectrogram* function, the Hamming window. If the sampling shift changes, a new set of equations must be used to calculate the device characteristics. For these reasons, the rectangular window is chosen for characterization.

The MATLAB [25] function *spectrogram* is used with a rectangular *window* size five times the number of samples per period, *overlap* is set to half of the PWM period, and *nfft* is set to the *window* size.

The DC method equations in (3.17) are used with the harmonic information found using the STFT to find the characteristics in Figures 3.10(a) and 3.10(b). These figures show the results for the phase A positive current quantities, IGBT1 and diode2, though all devices can be characterized using this method.



(a) Experimental voltage for an IGBT.



(b) Experimental voltage for a diode.

Figure 3.10: Experimental results of voltage drop spectrum extraction for AC using STFT.

3.3 Diagnosis of Inverter Faults

This section describes an improved bond wire lift-off (BWLO) fault diagnostic method which uses knowledge of the device voltage-current characteristics. To demonstrate that inverter nonlinearities can improve condition monitoring, a common fault, the BWLO fault, is chosen [49]. The diagnostic methods are tested using an inverter and induction machine. The BWLO is replicated experimentally by adding small resistances to the phase A of the inverter. The characterization method is used to directly diagnose the fault.

3.3.1 Diagnosis with Inverter Characterization

Measuring the resistance of the devices directly will allow for the diagnosis of BWLO faults. The resistance is periodically measured using the inverter characterization method, and any changes used to diagnose a fault.

Further, because the characterization technique can detect small changes in the resistance, it is possible to determine the exact number of lifted bond wires. Because the resistance is constantly measured, as long as saturation-level current is applied, drift due to non-fault reasons such as thermal drift could be ruled out.

Characterization of the inverter top phase A IGBT and bottom phase A diode under different faults results in the plots in Figure 3.11. The plots give the voltage and current relationship calculated with the algorithm characterization method for the entire current range when a balanced three phase sinusoidal current with a magnitude of 150 A is applied to each phase of the inverter.

The equivalent forward voltage and resistance are calculated from the voltage-current plots and are given in Table 3.4. Both the resistance and forward voltage drop are found by

taking the linear regression of voltage-current data in the saturation region. This is repeated for 27 power cycles; there are 27 separate resistance calculations. The variance taken from 27 resistance calculations is given in Table 3.5. The small variance, and therefore calculation accuracy of the characterization method demonstrates that it is possible to use it to diagnose faults.

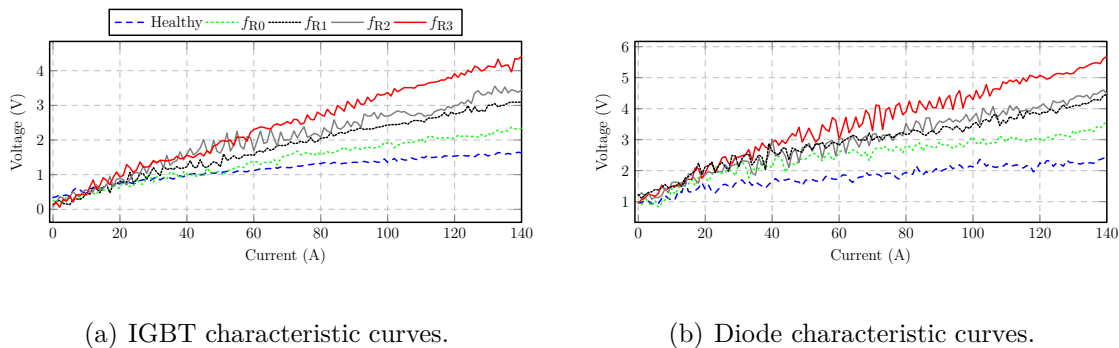


Figure 3.11: Experimental device characteristics under different fault levels.

Table 3.4: Linear approximation parameter of device nonlinearity with added fault.

	Healthy	f_{R0}	f_{R1}	f_{R2}	f_{R3}
$R_{\text{fault,d}}$	5.7 m Ω	11.5 m Ω	17.2 m Ω	20 m Ω	26.4 m Ω
$V_{\text{fault,d}}$	0.85 V	0.71 V	0.70 V	0.66 V	0.67 V
$R_{\text{fault,i}}$	5.7 m Ω	10.4 m Ω	18.7 m Ω	19.8 m Ω	27 m Ω
$V_{\text{fault,i}}$	1.53 V	1.86 V	1.52 V	1.87 V	1.77 V

Table 3.5: Variance as a percentage of mean resistance for the resistances calculated from a linear regression of 27 power cycles taken in the saturation region.

	Healthy	f_{R0}	f_{R1}	f_{R2}	f_{R3}
σ_d^2	0.0035 %	0.0093 %	0.0534 %	0.0085 %	0.0087 %
σ_i^2	0.004 %	0.0049 %	0.004 %	0.0002 %	0.0316 %

3.3.2 Online Diagnosis

The online detection algorithm is a six step process given by Figure 3.12. The bottom device and DC link voltages given in Figure 3.14 are sensed with either sensors or the circuit configuration in Appendix 6. The individual device voltages are extracted as in section 3.3.1. The device voltages are then filtered and normalized. The filtered and normalized quantities are then used as inputs to the cumulative sum (CUSUM) function in a method similar to an open circuit diagnosis method discussed by Meinguet *et al.* [28]. Once a fault is present, the CUSUM values will grow and the respective fault flag will be set.

The instantaneous device voltage features given in Figure 3.15 show a clear change in the amplitude of the top phase A IGBT voltage quantity in the presence of a fault. A fourth-order low pass filter given by equation (3.24) and Figure 3.13 is applied to this which reduces the features to a roughly constant quantity—this is also given in Figure 3.15; The output is an average of the instantaneous voltage features. The filter coefficients are chosen to correspond to a cutoff frequency of 125 Hz and are designed using the MATLAB filter design toolbox. The coefficients are given in Table 3.6.

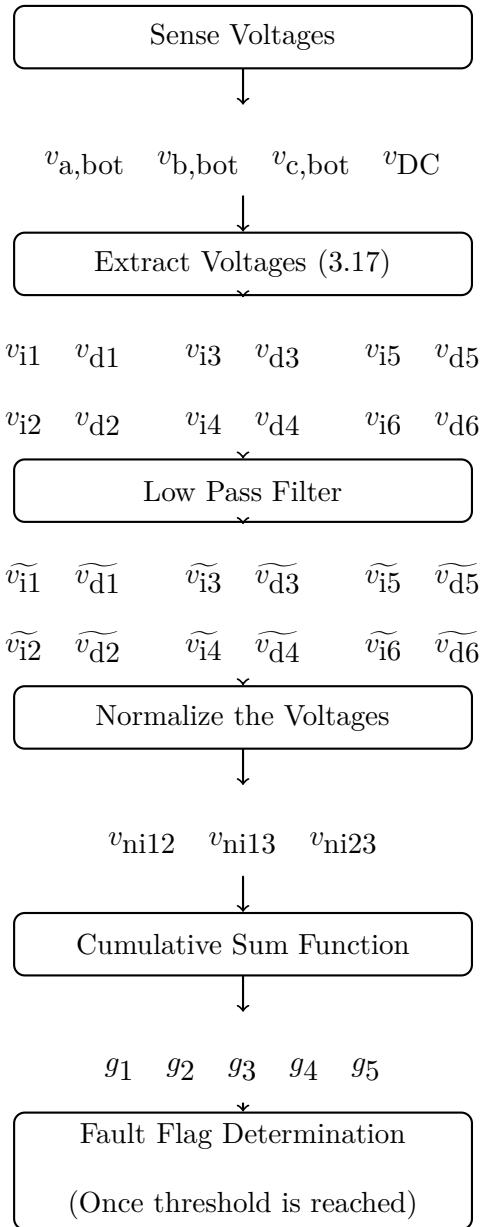


Figure 3.12: Characterization method used to determine the voltage and current relationship of inverter devices

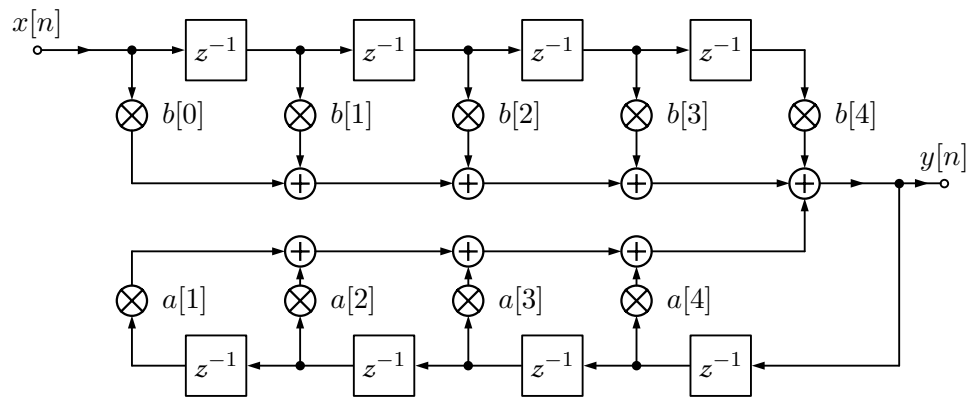


Figure 3.13: Filter used for online device diagnosis method

$$H(z) = \frac{y}{u_i} = \frac{b(0) + b(1)z^{-1} + b(2)z^{-2} + b(3)z^{-3} + b(4)z^{-4}}{a(0) + a(1)z^{-1} + a(2)z^{-2} + a(3)z^{-3} + a(4)z^{-4}} \quad (3.24)$$

Table 3.6: Filter Coefficients

b	$1.4e-7$	$5.7e-7$	$8.5e-7$	$5.7e-7$	$1.4e-7$
a	1	-3.9	5.7	-3.7	0.9

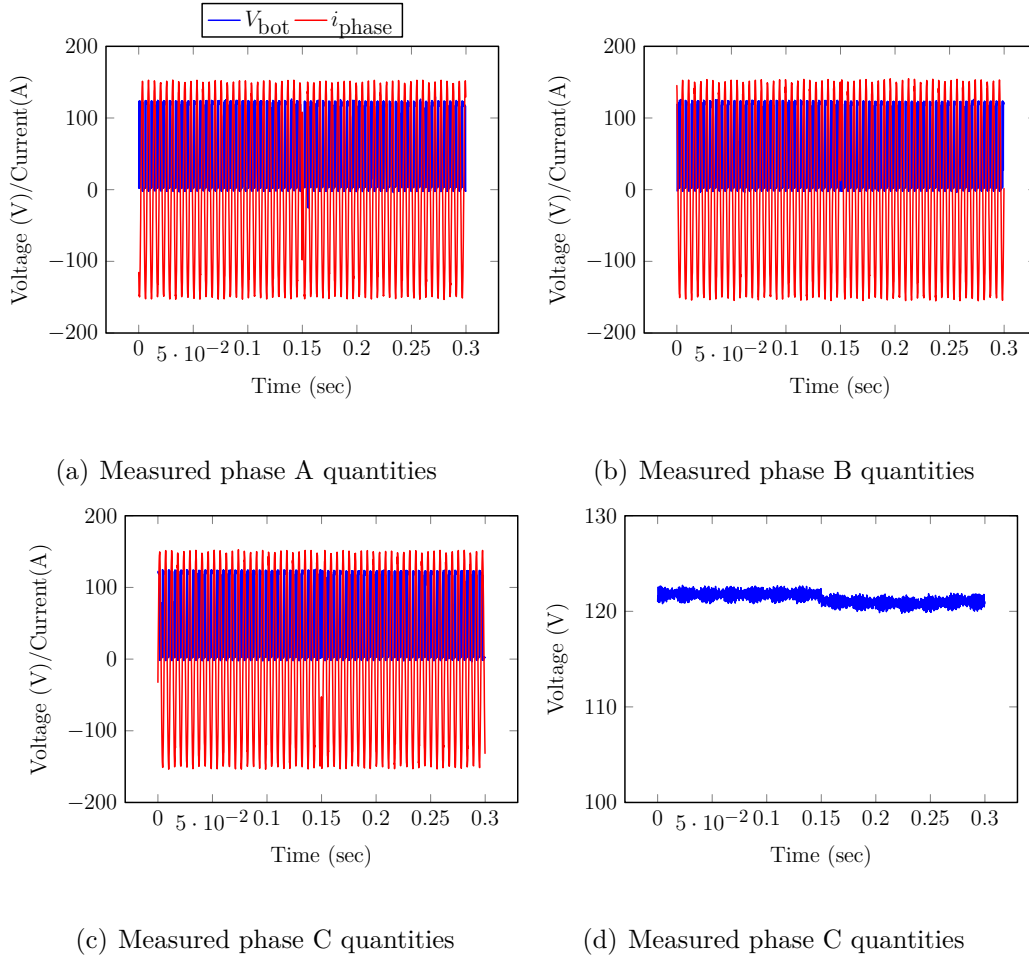
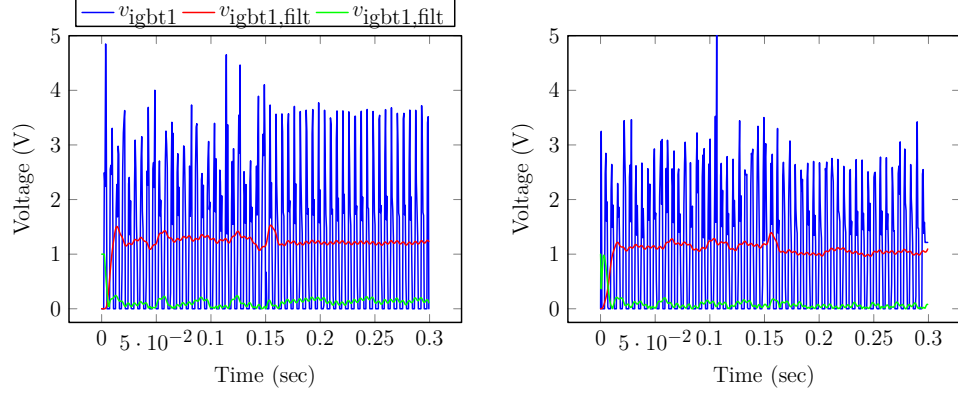
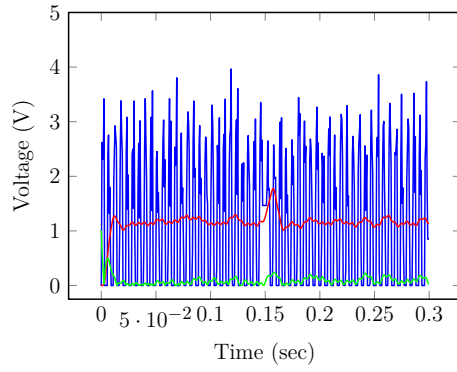


Figure 3.14: Quantities used as inputs to the online diagnosis method

Once filtered, the features are then normalized by equations (3.25)-(3.27). The features are subtracted from one another to allow for the features to be zero under healthy conditions.



(a) Phase A top IGBT device quantities (b) Phase B top IGBT device quantities



(c) Phase C top IGBT device quantities

Figure 3.15: Variables extracted with the spectral characterization method

The result of this is normalized to the maximum of the filtered voltage features for a given time instant; the result is given in Figure 3.15.

$$v_{ni12} = \left| \frac{v_{i1} - v_{i2}}{\max(v_{i1}, v_{i2}, v_{i3})} \right| \quad (3.25)$$

$$v_{ni13} = \left| \frac{v_{i1} - v_{i3}}{\max(v_{i1}, v_{i2}, v_{i3})} \right| \quad (3.26)$$

$$v_{ni23} = \left| \frac{v_{i2} - v_{i3}}{\max(v_{i1}, v_{i2}, v_{i3})} \right| \quad (3.27)$$

In order to make the online detection noise resistant and use multiple features, multiple

samples are used rather than the instantaneous voltage features. This is done with the CUSUM algorithm [28]. The input to the CUSUM algorithm is the log-likelihood ratio between any two health states j and l ($0 \leq l \neq j \leq n_f$),

$$s_{j,l}(k) = \ln \frac{p_j(r[k])}{p_l(r[k])}, \quad (3.28)$$

where p_j and p_l are the probability distribution functions of $[r(k)]$ under the states for j and l , respectively. It is assumed that the features are Gaussian distributed; doing so allows us to find the LLR as

$$s_{j,l}(k) = ([\mu_j] - [\mu_l])^T [\Sigma]^{-1} ([r(k)] - \frac{[\mu_j] + [\mu_l]}{2}). \quad (3.29)$$

It is necessary to determine the fault state distributions in order to conduct the online diagnosis. The mean is found as the expected fault level; the fault resistance can be determined from the number of lifted bonds. The resistance can then be used to determine the mean of the fault voltage. In this work, the mean of 27 features is used. The variance is difficult to determine practically, therefore the variance matrix is chosen as the identity matrix; this does not have a large effect on the performance of the diagnosis method.

Because, as an effect of the Gaussian distributions, $s_{j,l}(k) = s_{j,0}(k) - s_{l,0}(k)$, it is possible to calculate each fault state (l, j) with respect to the health state 0.

The CUSUM operates by successively summing the LLR using

$$g_{j,0}(k) = \max(0, g_{j,0}(k-1) + s_{j,0}(k)). \quad (3.30)$$

This can be slightly modified to distinguish even between fault phases using

$$g_j^*(k) = \min_{0 \leq l \neq j \leq n_f} (g_{j,0}(k) - g_{l,0}(k)). \quad (3.31)$$

By normalizing and subtracting the resistances from one another, the healthy state lies at the origin, thus $g_{0,0}(k) = 0$. Without the presence of a fault, the LLRs will be negative, and the healthy function will therefore be the highest. Because the CUSUM integrates only the positive sum of $g_{j,0}(k-1)$ and $s_{j,0}(k)$, when a fault is present ($s_{j,0}(k) > 0$) the CUSUM will integrate the LLR $s_{j,0}(k)$ —this will cause $g_{j,0}(k)$ to grow. Once the threshold for the CUSUM function—determined in the next paragraph—is reached, the corresponding fault flag is set.

The detection delay,

$$\Delta t_{\text{FDI},l} = T_s \left(\frac{h_{\text{FDI},l}}{\min_{0 \leq l \neq j \leq n_f} \kappa_{l,j}} \right), \quad (3.32)$$

is inherent with the fault detection because it is an integrator; this delay can be chosen by the selection of a CUSUM threshold. The $\kappa_{l,j}$ Kullback-Leibler information given in equation 3.33 [28] defines the distance between the statistical distributions for two given fault states; this is a result of the data for each fault. The sampling period T_s is defined by the sampling time of the input to the CUSUM algorithm—it is $100 \mu\text{sec}$ in the case of the data. With the sampling period and Kullback-Leibler information, the delay is chosen by calculating the threshold value $h_{\text{FDI},l}$; for a sampling delay $\Delta t_{\text{FDI},l} = 0.11 \mu\text{sec}$, the threshold is found to be 2.37. The other cumulative sum results plots to detect higher resistance faults are given in Figures 3.17-3.19.

$$\kappa_{l,j} = \frac{1}{2}([\mu_j] - [\mu_l])^T [\Sigma]^{-1}([\mu_j] - [\mu_l]) \quad (3.33)$$

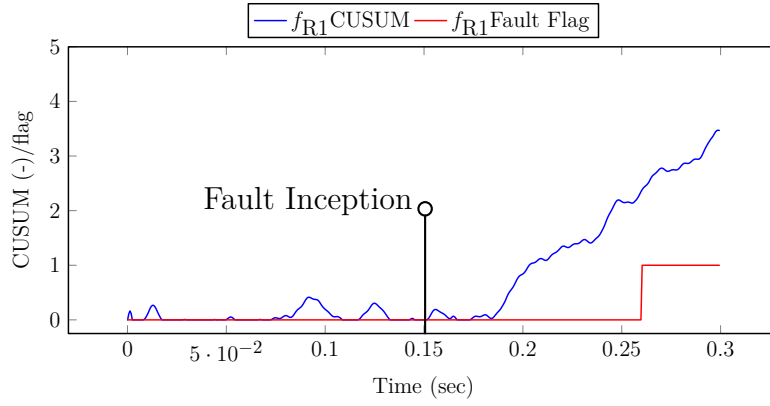


Figure 3.16: Cumulative sum function and fault flag set for f_{R1}

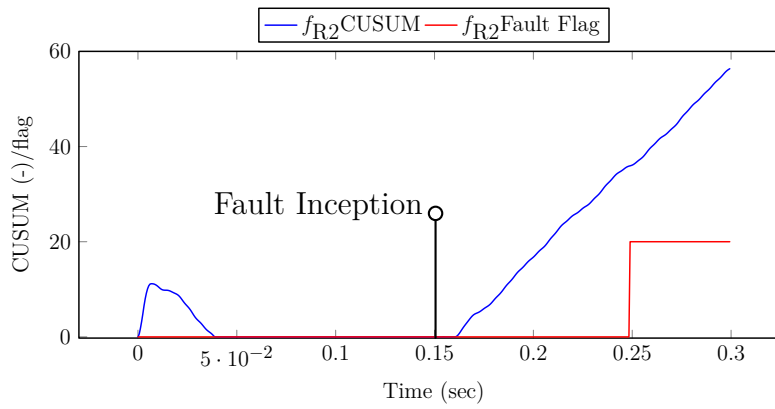


Figure 3.17: Cumulative sum function and fault flag set for f_{R2}

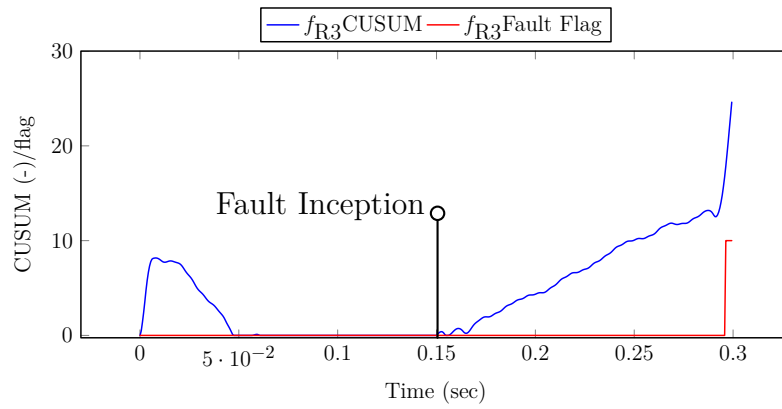


Figure 3.18: Cumulative sum function and fault flag set for f_{r3}

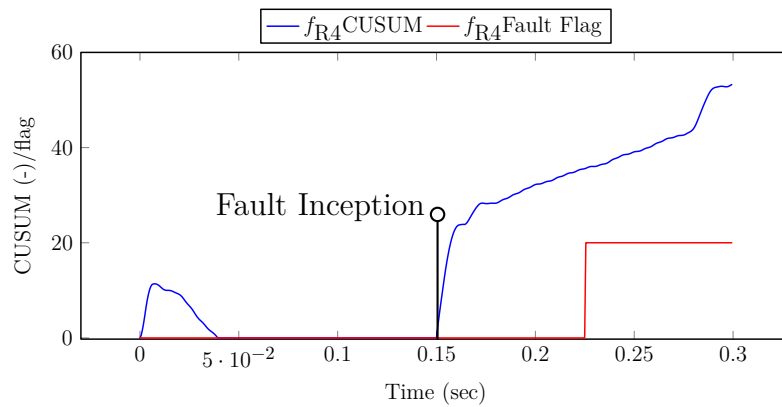


Figure 3.19: Cumulative sum function and fault flag set for f_{r4}

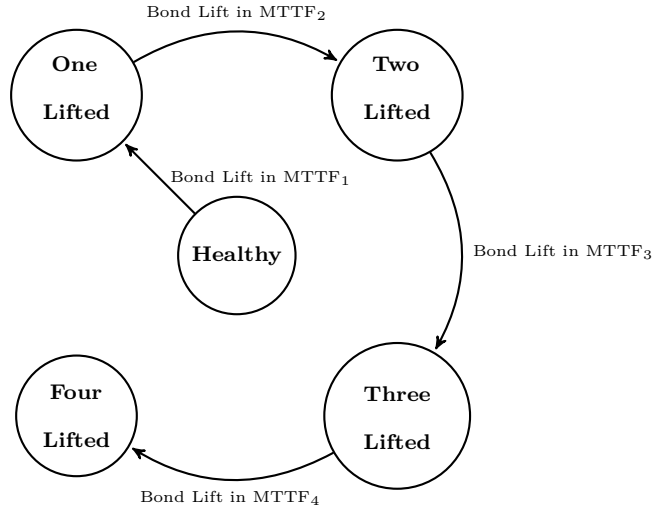


Figure 3.20: Paths to failure for BWLO in one phase of an IGBT inverter system, shown here for four bonds.

3.4 Effect of Bond Wire Lift-Off Faults on Lifetime

The inverter lifetime method calculates the RUL using the Arrhenius model, but requires junction temperatures [24]. The Cauer thermal model is used to determine these temperatures. The application is assumed to be a traction drive. The operating conditions chosen in the determination of these temperatures are defined by the ECE 15 + EUDC driving cycle [3].

To determine the MTTF, the device temperatures are not directly measured, but are instead estimated using the Cauer thermal model. The losses in the switches are used in this thermal model. If there is a BWLO fault, the resistance of the device, and therefore ohmic losses, will increase. By performing the characterization method online, the ohmic losses in each of the devices is found by determining the resistance; the ohmic loss estimate is constantly updated. With better knowledge of the ohmic losses, the accuracy of the thermal model and therefore the temperature estimation is improved. This results in a better RUL

Table 3.7: Enhanced MTTF prediction assuming that there are 68 thermal cycles in a day.

Fault Severity	T_m °C	ΔT_j K	N_f	MTTF (hours)
Healthy	60.8	59.05	1.9×10^6	669×10^3
f_{R_0}	86.1	115.5	14.6×10^3	5.1×10^3
f_{R_1}	112.6	174.3	472.3	166.7
f_{R_2}	123.3	198.1	151	53.3
f_{R_3}	151.3	260.4	12	4.1

estimation.

Figure 3.20 is used to demonstrate the benefit of improved MTTF estimation. Assuming that there are five states, one healthy and four faulty (i.e. one or more lifted bonds), under normal circumstances the MTTF is always estimated to be $MTTF_t$, the typical MTTF. Without an improved MTTF estimation with characterization, if there is a fault, while the MTTF will in reality drastically decrease, the MTTF estimation will always be $MTTF_t$. If the fault level is known, the MTTF is recalculated, resulting in $MTTF_1, MTTF_2, \dots$. These new MTTF calculations will better reflect reality, as they are based upon the actual device losses. Operation with the driving cycle results in different thermal profiles under different fault levels from the healthy to the largest fault resistance case. Using the calculated range of temperatures and the mean temperature once the inverter has warmed up, the MTTF calculation is made, and is shown in Table 3.7. The benefit of the enhanced prognostic method is demonstrated in Figure 3.21, showing that if the fault severity is not determined in the BWLO case, as bonds lift off, the change in estimated MTTF is very large.

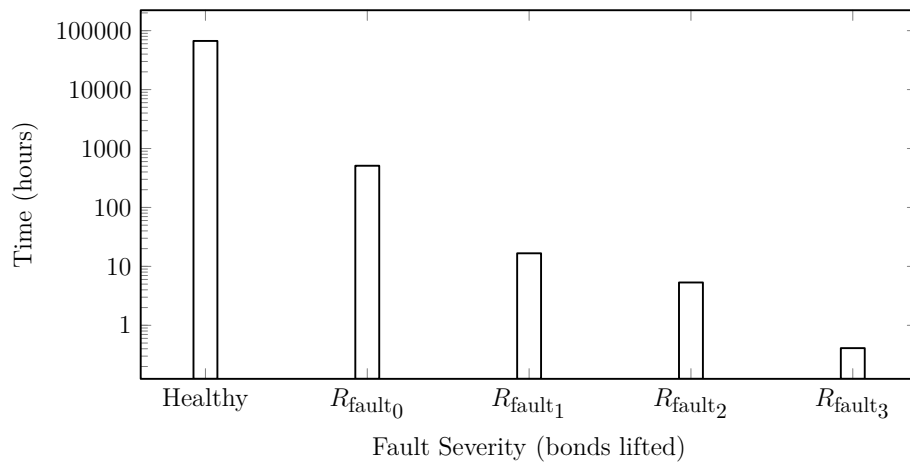


Figure 3.21: The change in MTTF estimation under different fault levels with the enhanced RUL calculation.

Chapter 4

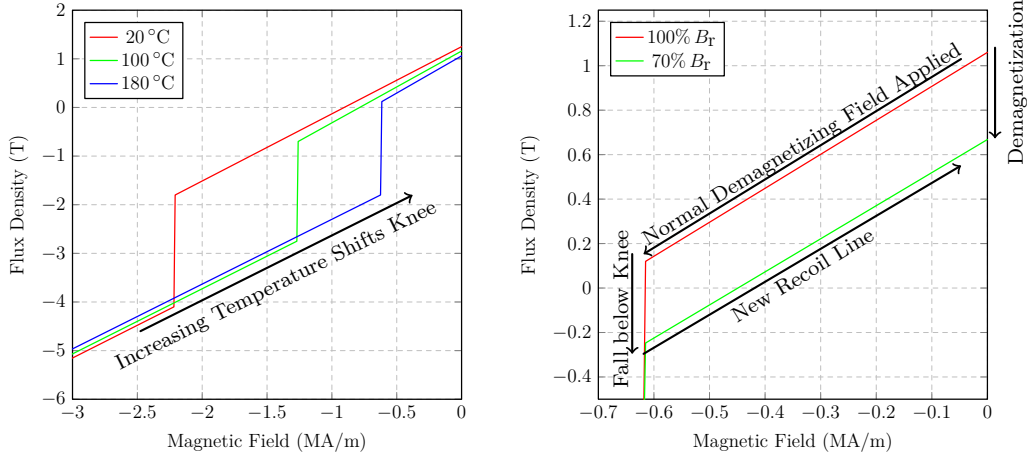
Assessing and Effects of Partial Rotor Demagnetization

Uniform demagnetization occurs when the remnant flux density of every magnet in a machine is reduced by some quantity; partial demagnetization is when less than all of the magnets have a reduced remnant flux density.

In Figure 4.1(a), multiple B-H curves are given for the same magnet material. Note that the H_C at the point which the curves cross the $B = 0$ T point is very negative at 20°C and increases as the temperature increases. This—with the fact that the knee also moves nearer to the $B = 0$ T results in a larger vulnerability to demagnetization. In Figure 4.1(b), the flux density is shown for two values of remaining remnant flux density, $70\% B_R$ and $100\% B_R$. Note that when demagnetizing field is applied the operating point of the magnet moves along the red curve; once it passes the knee, irreversible demagnetization occurs. The point of B at which the curve stops at defines the new remaining remnant flux density B_R . The net loss in B_R is what is termed demagnetization of one or more magnets.

4.1 Apparent Inductance and Incremental Inductance

In Figure 4.2, the flux linkages are given for some coil with respect to the applied current. If the current is divided out of this, since $\lambda = Li$, the result is the apparent inductance,



(a) B-H curves are shown for three temperatures
 (b) B-H curves are shown for a healthy magnet and one that has been demagnetized

Figure 4.1: B-H curve for a generic magnet material

also given in Figure 4.2. Either the inductance or flux is sufficient to characterize the electromagnetic coil which it represents, perhaps the direct or quadrature axis of a PMSM. The incremental inductance is another measure given in Figure 4.2, and is the derivative of the flux function with respect to current. Because it is the derivative rather than the ratio of λ/i , it shows a more clearly defined peak at the inflection point of the flux curve.

4.2 Demagnetization Machine

A rotor was designed to fit an existing machine designed by Foster in [14]; the same geometric dimensions and materials were used to constrain the design process; a comparison of the previous and proposed machine is given in Table 4.1. The number of magnets was reduced from 30 to 20 due to magnet availability. The desired mean torque is not a primary goal of the design, but a reasonable torque should be achieved; the desired torque is greater than $30 \text{ N} \cdot \text{m}$ at the maximum current of the machine, $18 A_{\text{RMS}}$. The rotor must also be

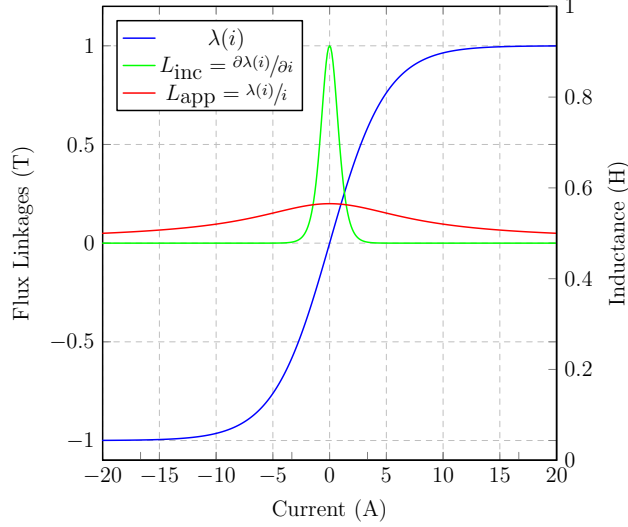


Figure 4.2: A generalized flux linkage with respect to current (blue) is shown along with the corresponding incremental inductance (green) and apparent inductance (red).

mechanically robust—to achieve this, the bridge and rib width should be greater than 1 mm.

The main design goal will be to reduce the torque ripple,

$$\%T_{\text{ripple}} = \frac{T_{\text{max}} - T_{\text{min}}}{T_{\text{avg}}} \times 100\%, \quad (4.1)$$

to be within 20% of the average torque at the maximum phase current.

An optimization algorithm is performed to reduce the torque ripple given the other design constraints. In order to perform the optimization, a large number of magnet placement combinations are simulated using the Flux2D finite element analysis software. This is accomplished by first parameterizing the magnet placement using the three variables shown in Figure 4.3: the distance from the center of the rotor to the magnets, D_1 ; the distance between the closest corners of the magnets, D_2 ; and the angle of the v-shape of the magnets, θ . The finite element model is capable of changing any of the variables; all combinations of

Table 4.1: Design constraints for demagnetization test machine

Motor Constraints	Previous 2/5 SPP Machine[14]	2/5 SPP Machine
Stator Diameter	220 mm	220 mm
Rotor Diameter	138 mm	138 mm
Stack Length	72 mm	72 mm
No. of Stator Slots	12	12
No. of Poles	10	10
Air Gap Length	1 mm	1 mm
Magnet Type	NdFeB N38EH	NdFeB N38EH
Winding Type	Single Layer Concentrated	Single Layer Concentrated
No. of Turns Per Coil	150 turns	150 turns
Stator Line Voltage	480 V	480 V
Maximum Current	$18 A_{\text{rms}}$	$18 A_{\text{rms}}$
No. of Magnets	30	20
T_{avg} at i_{max}	$55 \text{ N} \cdot \text{m}$	$> 30 \text{ N} \cdot \text{m}$
$T_{\text{r,pk-pk}}$ at i_{max}	$10 \text{ N} \cdot \text{m}$	20%
Thinnest Steel	– mm	1 mm

the three are used to find a suitable design. Transient finite element analysis is performed for all of these combinations; two fundamentals of the torque ripple are determined. All candidate designs are removed which are not physically possible due to collisions, have steel less than 1 mm thick, or those with $T_{\text{avg}} < 10 \text{ N} \cdot \text{m}$.

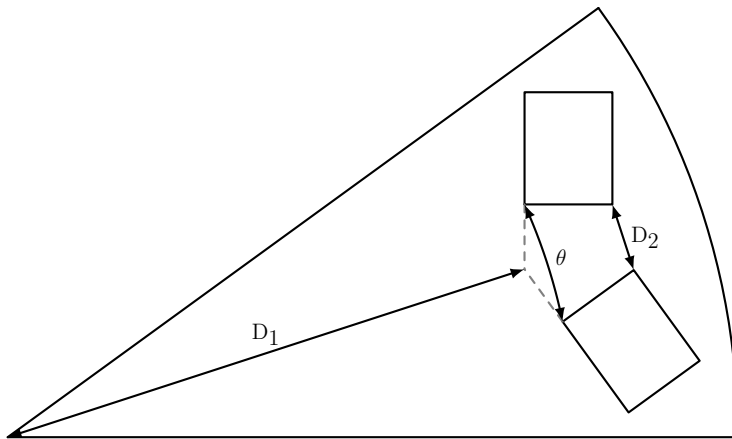


Figure 4.3: Rotor dimensions used to optimize torque ripple

The best designs were not within the desired torque ripple, but some design objectives became clear from the optimization procedure, including:

- have a v-shape,
- be close to airgap, and
- have a small D_2 value.

Designs which fulfilled these requirements all had a minimal amount of magnet field shorting, or field leaving one face of the magnet and entering the other. Minimal shorting is desirable for two reasons: maximal use of the magnet (higher torque) and a smoother airgap flux density (less ripple). In order to create a design which achieved this, air was added around the magnets to reduce shorting. By adding air to the outside of the magnet 'v', shorting was reduced. By adding air between the magnets, no shorting could occur through the center rib. An ideal design using this air configuration is given in Figure 4.4(a). Because this is

not mechanically stable, a small strip of steel was added to the center rib, resulting in the design in Figure 4.4(b). Because the rib is small, it saturates and behaves as air, limiting shorting through the rib.

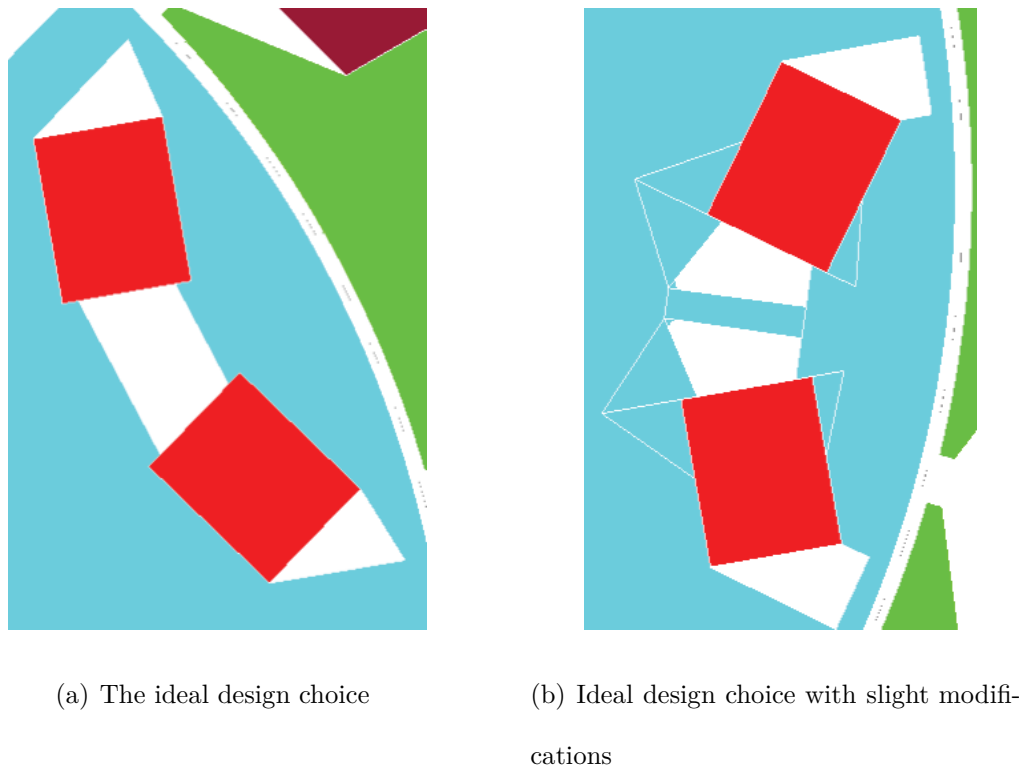


Figure 4.4: Magnet placement results of the optimization procedure

The rotor design shown with the stator in Figure 4.5 was chosen for use for the demagnetization analysis. The FEM and circuit in Figure 4.6 are used for all FEM simulations. The parameters in Table 4.2 are used; the same resistance and nominal remnant flux density are used, because the same stator and magnets are used, respectively.

Table 4.2: Additional finite element model parameters

FEM Parameter	2/5 SPP Machine	
Phase Resistance	R_s	1.5 Ω
Nominal Remnant Flux Density	$B_{r,nom}$	1.18 T

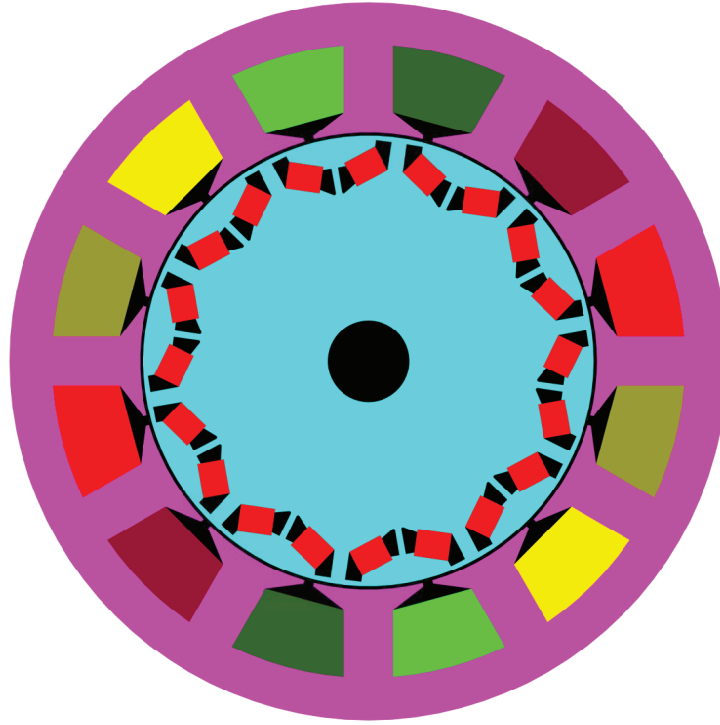
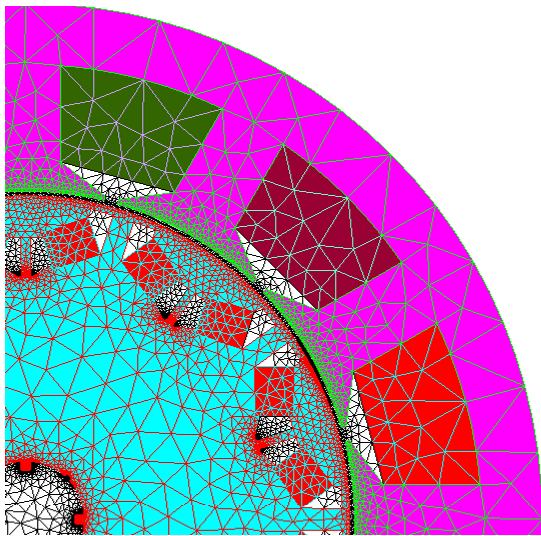
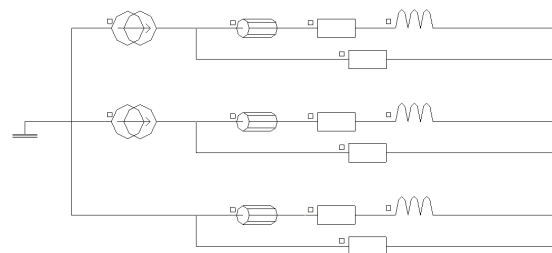


Figure 4.5: Finite element model designed and used for the demagnetization method evaluation



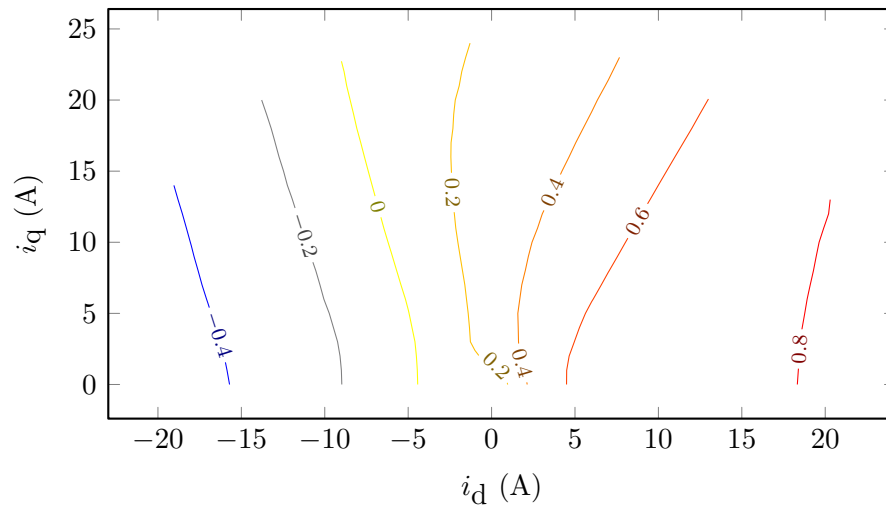
(a) Demagnetization test machine finite element model with mesh



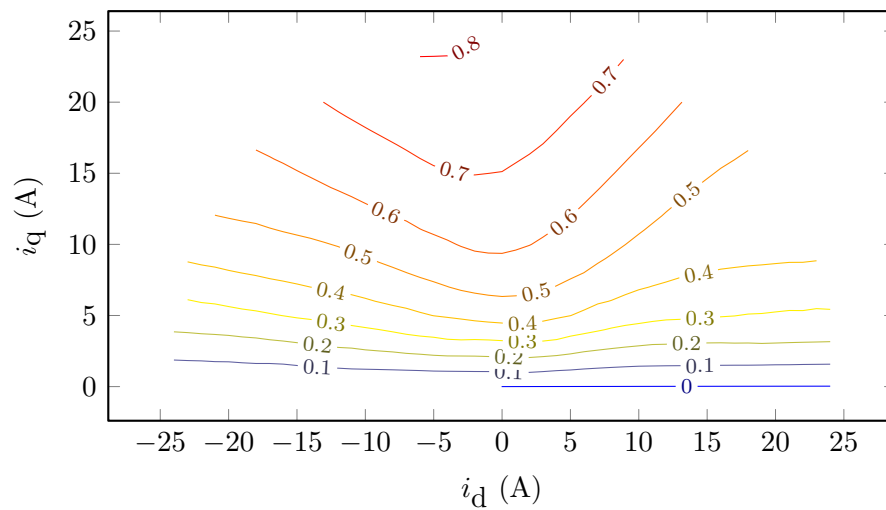
(b) Demagnetization test machine finite element model circuit

Figure 4.6: Finite element model for test machine

Some basic characteristics are determined from finite element analysis. The flux linkages λ_d and λ_q are calculated using equation 2.19 and given in Figure 4.7.



(a) Direct axis flux linkages, λ_d



(b) Quadrature axis flux linkages, λ_q

Figure 4.7: Finite element model for test machine

The back-EMF taken at 300 RPM is plotted for all three phases with respect to the angular position in Figure 4.8.

The torque response is determined with respect to the control angle in Figure 4.9 for current magnitudes ranging from $2.5 A_{pk} \rightarrow 25 A_{pk}$ in increments of $2.5 A_{pk}$

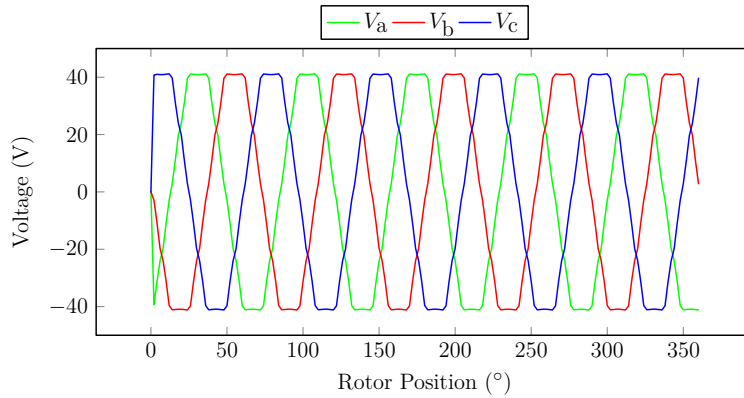


Figure 4.8: Three phase back EMF taken at 300 RPM

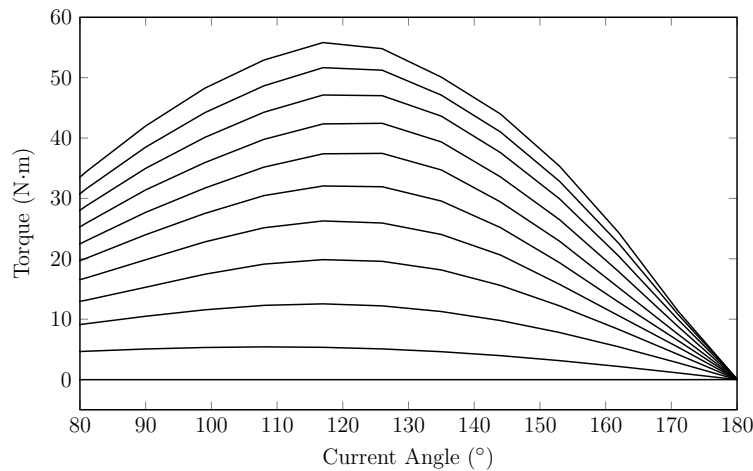


Figure 4.9: Torque profile for current range; taken at 300 RPM

Figure 4.10 shows the torque at $18A_{RMS} \angle 117^\circ$; the mean is $T = 53.3 \text{ N}\cdot\text{m}$, and torque ripple is $T_r = 10.1 \text{ N}\cdot\text{m}$. The torque ripple is 19%, which falls within the desired torque ripple at maximum current.

4.3 Detection of Demagnetization

A comparison is made between a nominally magnetized machine in Figure 4.11 and one with a completely demagnetized magnet in Figure 4.12 with no armature current. The four whole

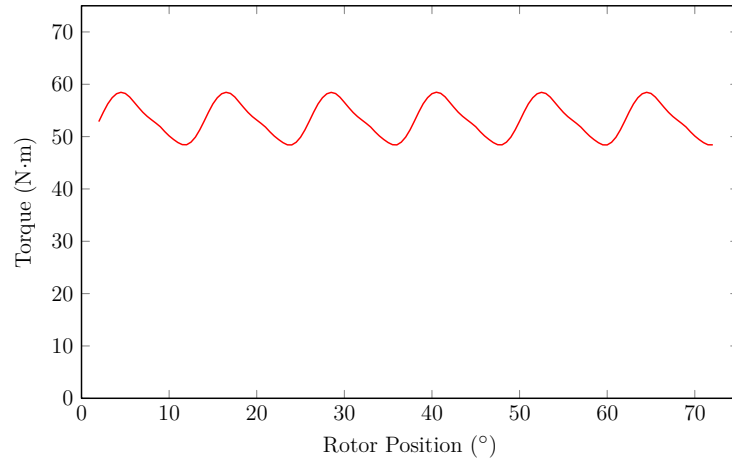


Figure 4.10: Nominal torque ripple calculated from the FEM at $18A_{\text{rms}}/117^\circ$ at 300 RPM magnets are used for this discussion, numbered one to four from the bottom to the top, as shown in Figure 4.11. The field behavior changes with no flux as is clearly seen in magnet three. The field strength linking magnets three and four is reduced. The field linking the stator also decreases, which indicates less flux linking the stator coils. This is especially clear in the direct axis formed by the ‘v’ of magnets two and three. The partial demagnetization of the rotor is shown to have a substantial effect on the magnetic characteristics.

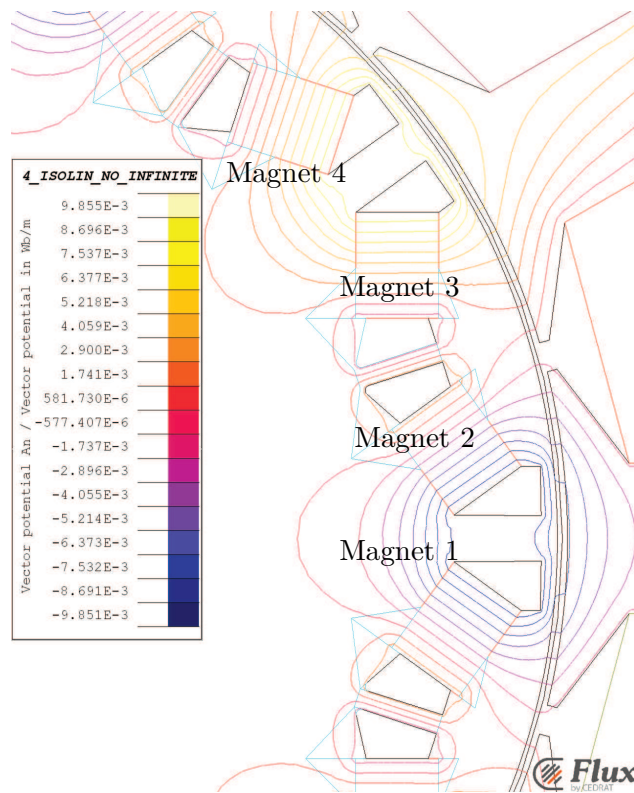


Figure 4.11: Field lines with normal magnetization

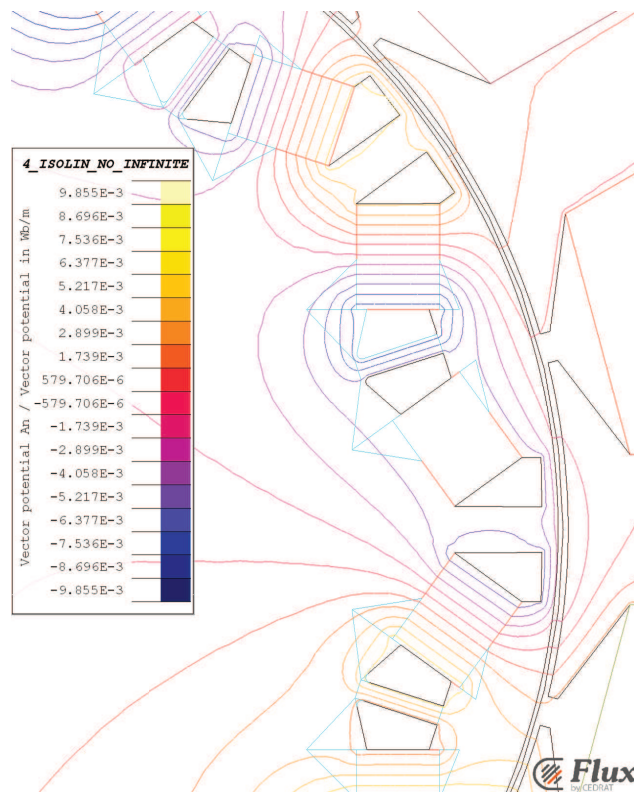


Figure 4.12: Field lines with one completely demagnetized magnet

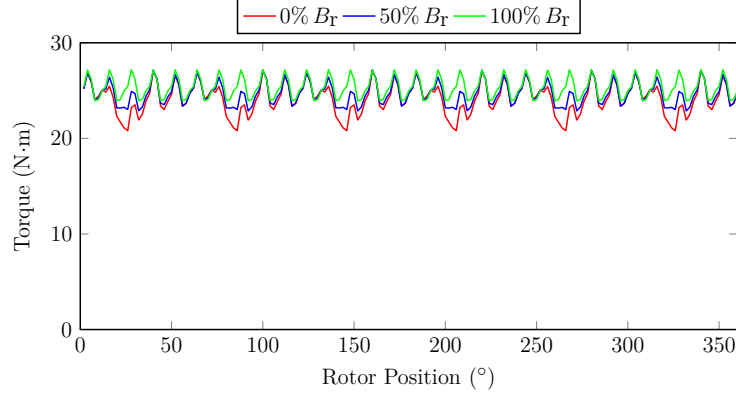


Figure 4.13: Torque ripple due to demagnetization calculated from the FEM at $7.1_{\text{rms}} \angle 117^\circ$ at 300 RPM

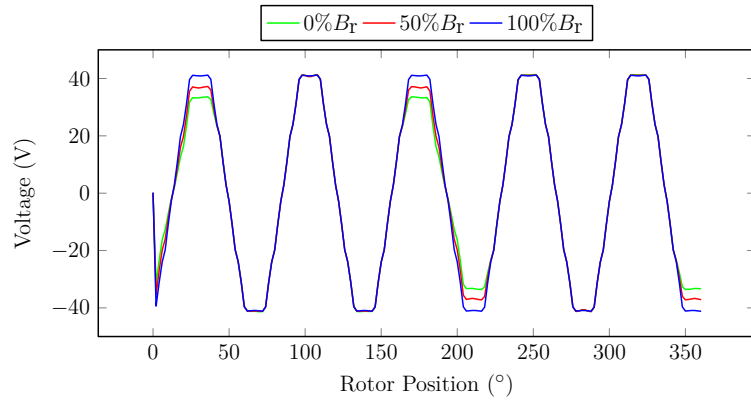
The effect of the change in the flux linking the stator can be seen in the open-circuit back-EMF in Figure 4.14(a). The asymmetrical linkage of the rotor flux with the stator results in an asymmetrical line-to-neutral back-EMF; it is also evident in the line-to-line back-EMF voltage, as shown in Figure 4.14(b). The frequency content of the EMF clearly changes per the predicted harmonic equation [6],

$$f_{\text{dm}} = f_s \left(1 \pm \frac{k}{p} \right), \quad (4.2)$$

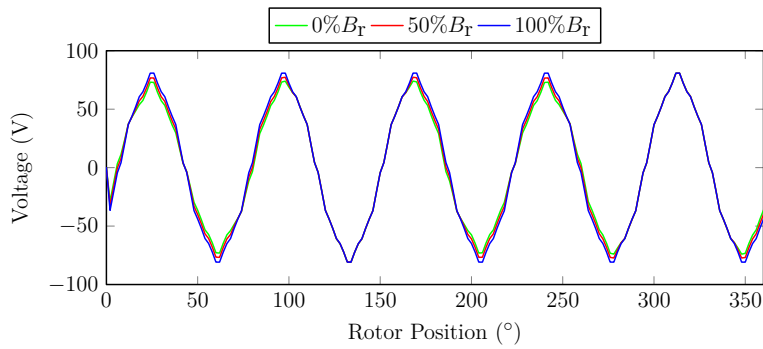
especially for the following harmonics as shown in Figure 4.14(c): 0.2, 1.4, 3.8 and 4.6.

Similarly, the line-to-line voltage in Figure 4.15(b) shows harmonic content changing for the 25 N·m, 300 RPM operating point at the harmonics predicted by the equation. The effect of the harmonic content change is evidenced by the line-to-line voltage in Figure 4.15(a).

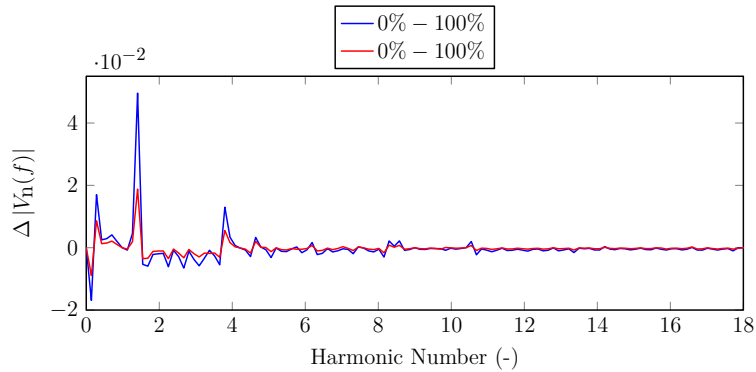
While the harmonics can be used to detect partial demagnetization, the same harmonics present themselves during an eccentricity fault. The incremental inductance is instead used to detect the partial demagnetization as an extension of [18]. In addition to a net λ_{af}



(a) Line-to-neutral EMF for phase A



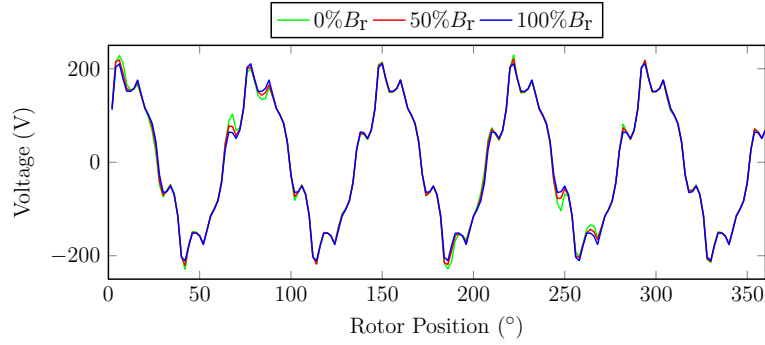
(b) Line-to-line EMF for phase A under demagnetization



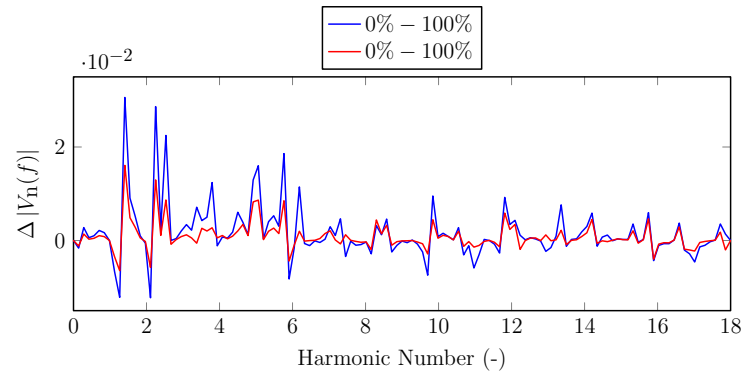
(c) Comparison of Single sided amplitude spectra of the line-to-line back EMF

Figure 4.14: Line-to-line EMF and comparison of harmonics.

reduction which shifts the knee of the direct axis flux linkage curve with applied positive direct axis, partial demagnetization introduces two knees due to the asymmetric flux-and



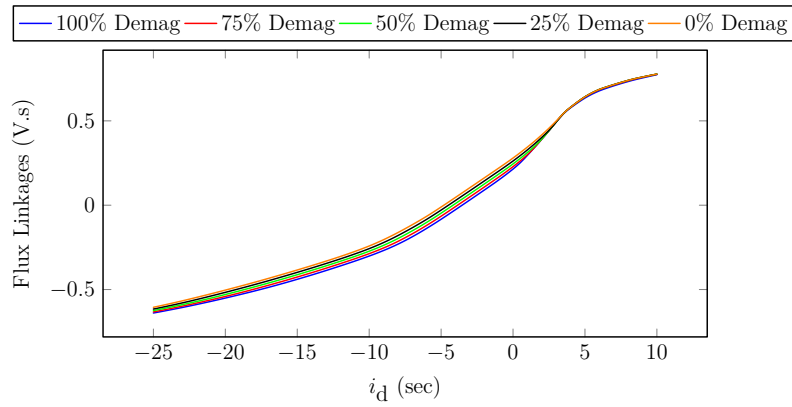
(a) Line-to-line voltage for phase A



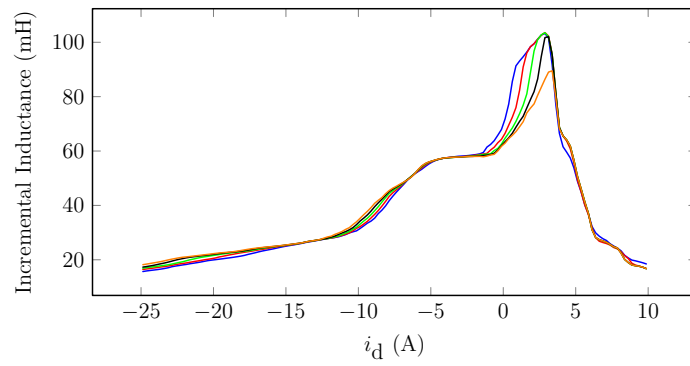
(b) Comparison of Single sided amplitude spectra of the line-to-line voltage

Figure 4.15: Line-to-line voltage and comparison of harmonics at 300 RPM and $7.1 A_{rms} \angle 117^\circ$ for varying degrees of magnet two demagnetization.

therefore saturation-behavior. In areas of the motor with less flux due to demagnetization there is a change in the saturation characteristics. By applying a range of positive direct axis currents, the multiple knees due to asymmetric saturation can be seen. Figure 4.16(a) shows the direct axis incremental inductance calculated from the direct axis flux linkages in Figure 4.16(b). As the remnant flux of the magnet decreases, a second peak develops at an earlier positive direct axis current value.



(a) Flux linkages under three levels of partial demagnetization



(b) Incremental Inductances under three levels of partial demagnetization

Figure 4.16: Incremental inductance and flux linkages for partial demagnetization testing of the designed machine

The second peak occurs for two reasons. The first reason is that the diverted magnetic field from the magnets in the area of the rotor saturates the iron more, preventing the stator field from penetrating deeply. Secondly, the field due to the stator current links the rotor but does not penetrate deeply due to the magnets in the area around the demagnetized magnet shorting; this saturates the surface of the rotor even more.

4.3.1 Comparison with Uniform Demagnetization

The torque ripple increases slightly for uniform demagnetization, as shown in Figure 4.17.

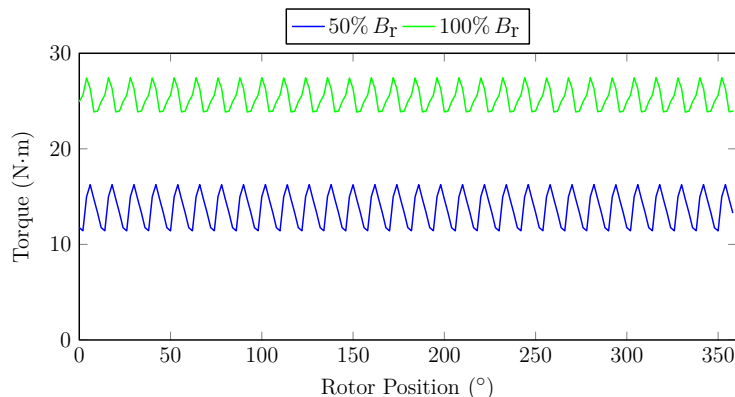
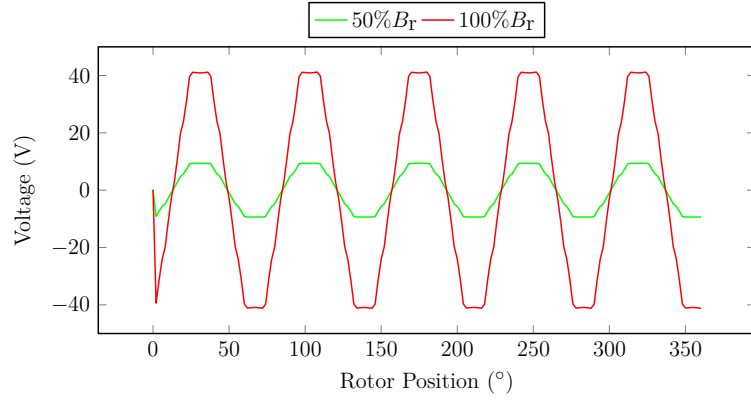


Figure 4.17: Torque ripple due to demagnetization calculated from the FEM at $7.1_{\text{rms}} \angle 117^\circ$ at 300 RPM

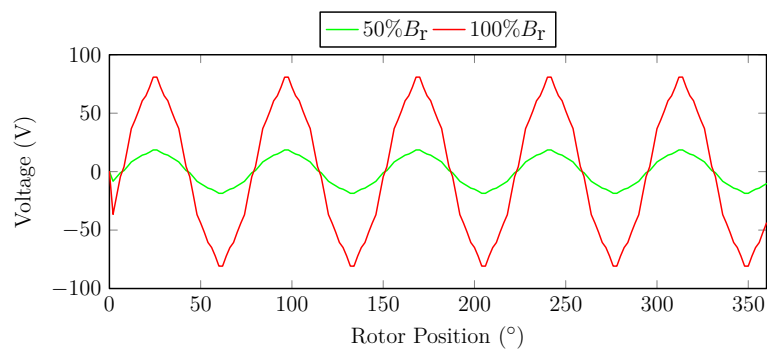
The back-EMF harmonics change slightly as shown in Figure 4.18(c), and from Figures 4.18(a) and 4.18(b), it is clear that the magnitude is the most visible change.

Significant voltage harmonics are however introduced when currents are applied, as shown in Figures 4.19(a) and 4.19(b). This is due to the change in saturation behavior as the knee of the flux curve of the direct axis changes for uniform demagnetization; this is shown in Figure 4.20(a).

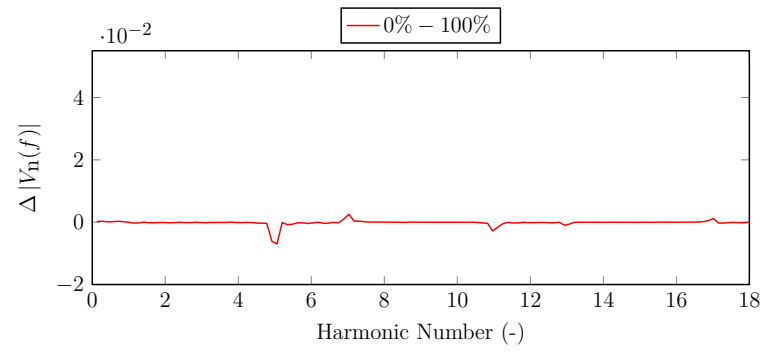
The incremental inductance behavior is shown under demagnetization in Figure 4.20(b).



(a) Line-to-neutral EMF for phase A

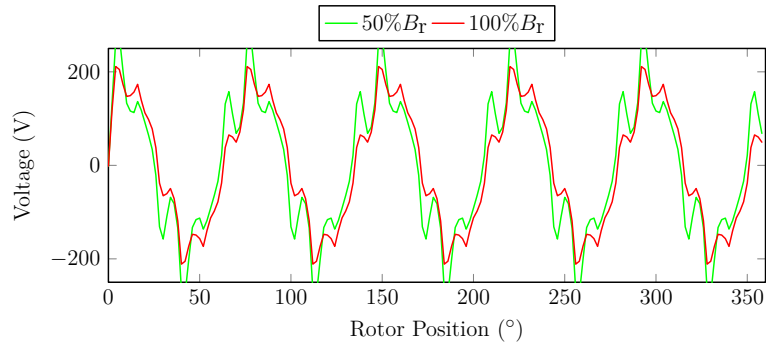


(b) Line-to-line EMF for phase A under demagnetization

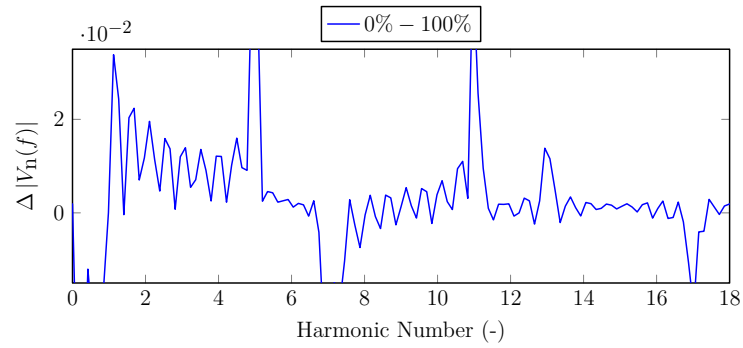


(c) Comparison of Single sided amplitude spectra of the line-to-line back EMF

Figure 4.18: Line-to-line EMF and comparison of harmonics for uniform demagnetization. Compared with the partial demagnetization, the entire peak of the incremental inductance moves during demagnetization due to the shift in the knee. While there are two peaks in the most severe case, the center of the incremental inductance peaks is shifted as compared

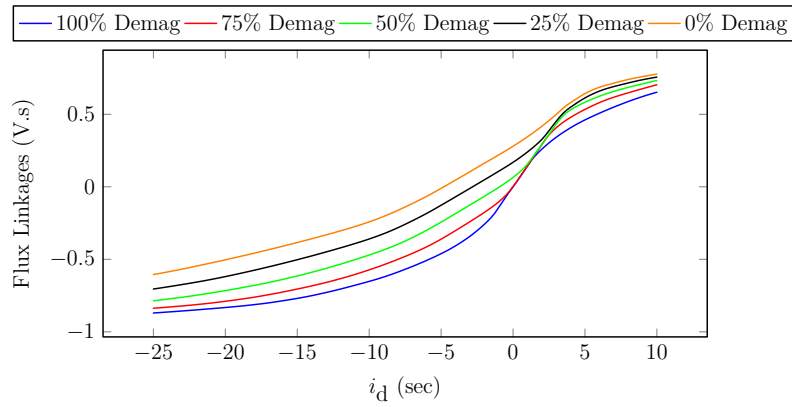


(a) Line-to-line voltage for phase A

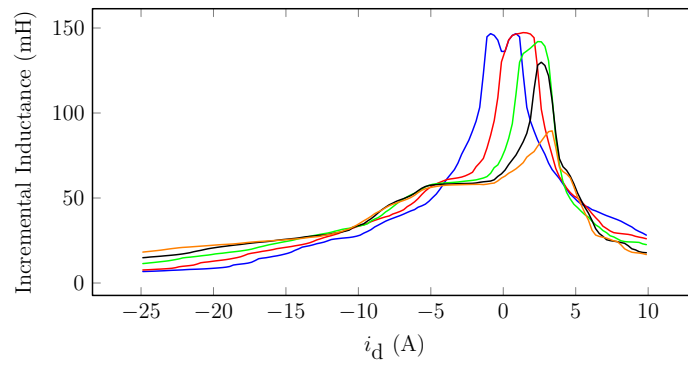


(b) Comparison of Single sided amplitude spectra of the line-to-line voltage

Figure 4.19: Line-to-line voltage and comparison of harmonics at 300 RPM and $7.1 A_{\text{rms}} \angle 117^\circ$ for varying degrees of uniform demagnetization. to the partial demagnetization case.



(a) Flux linkages under three levels of uniform demagnetization



(b) Incremental Inductances under three levels of uniform demagnetization

Figure 4.20: Incremental inductance and flux linkages for uniform demagnetization testing of the designed machine

4.3.2 Comparison with Pole Demagnetization

The torque ripple increases significantly for pole demagnetization, as shown in Figure 4.3.2.

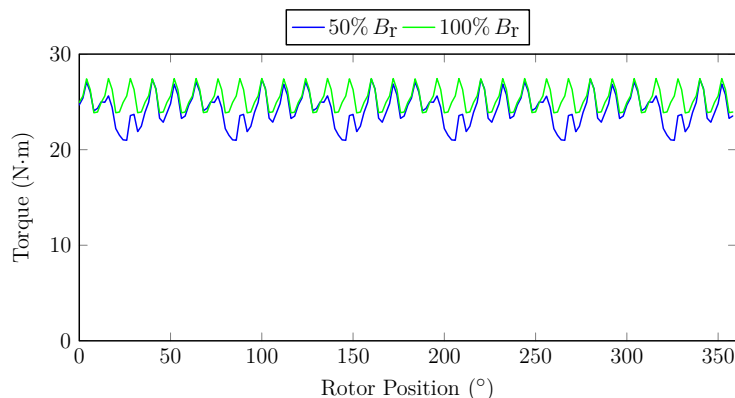
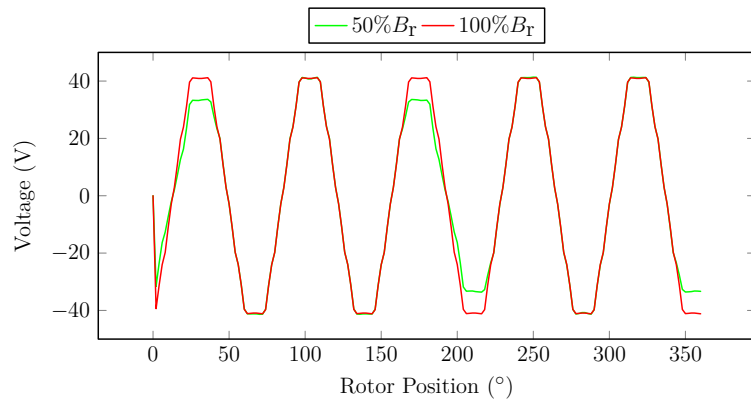


Figure 4.21: Torque ripple due to pole demagnetization calculated from the FEM at $7.1_{\text{rms}} \angle 117^\circ$ at 300 RPM

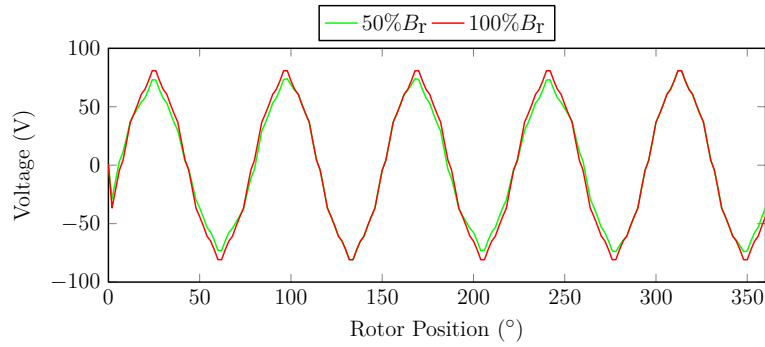
The back-EMF harmonics change as shown in Figure 4.22(c), and from Figures 4.22(a) and 4.22(b), it is clear that the magnitude is the most visible change. The magnitude of back-EMF change for pole demagnetization is more stark than for one magnet due to the absence and worsening of airgap flux asymmetry.

Similarly to the magnet demagnetization, significant voltage harmonics are introduced when currents are applied, as shown in Figures 4.23(a) and 4.23(b). This is also due to the change in the airgap flux density in the demagnetized pole; this is shown in Figure 4.24(a).

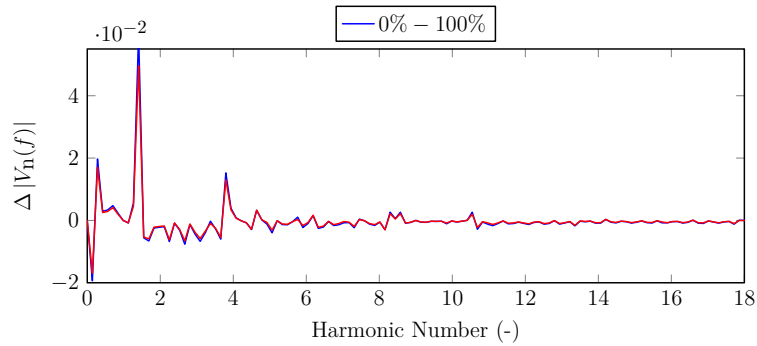
The incremental inductance behavior is shown under demagnetization in Figure 4.24(b). Compared with the one magnet demagnetization, the change in the peak is more significant.



(a) Line-to-neutral EMF for phase A

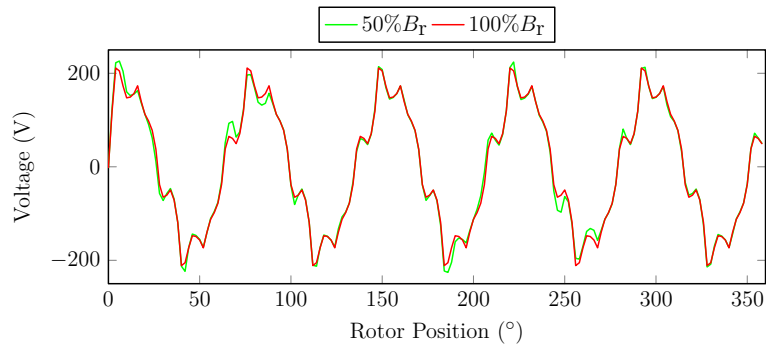


(b) Line-to-line EMF for phase A under demagnetization

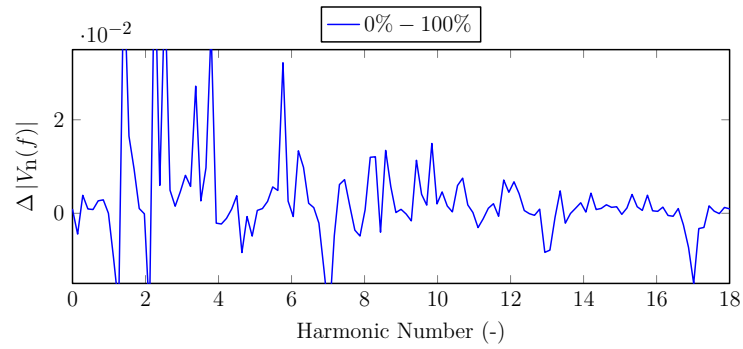


(c) Comparison of Single sided amplitude spectra of the line-to-line back EMF

Figure 4.22: Line-to-line EMF and comparison of harmonics for uniform demagnetization.

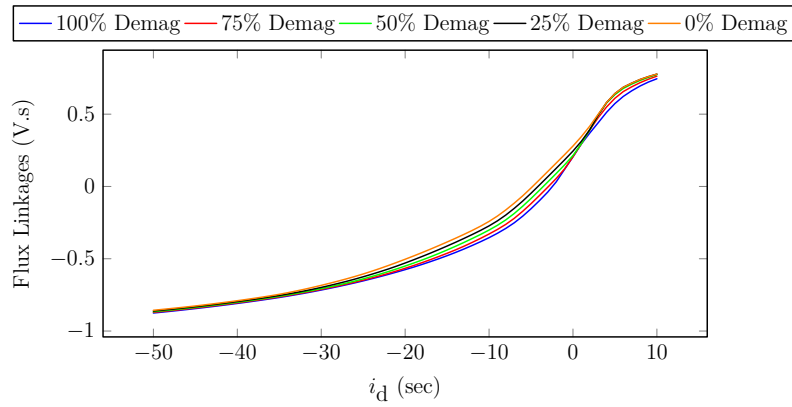


(a) Line-to-line voltage for phase A

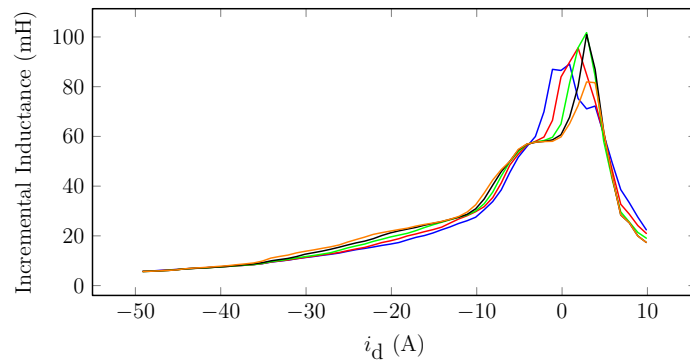


(b) Comparison of Single sided amplitude spectra of the line-to-line voltage

Figure 4.23: Line-to-line voltage and comparison of harmonics at 300 RPM and $7.1 A_{rms} \angle 117^\circ$ for varying degrees of uniform demagnetization.



(a) Flux linkages under three levels of uniform demagnetization



(b) Incremental Inductances under three levels of uniform demagnetization

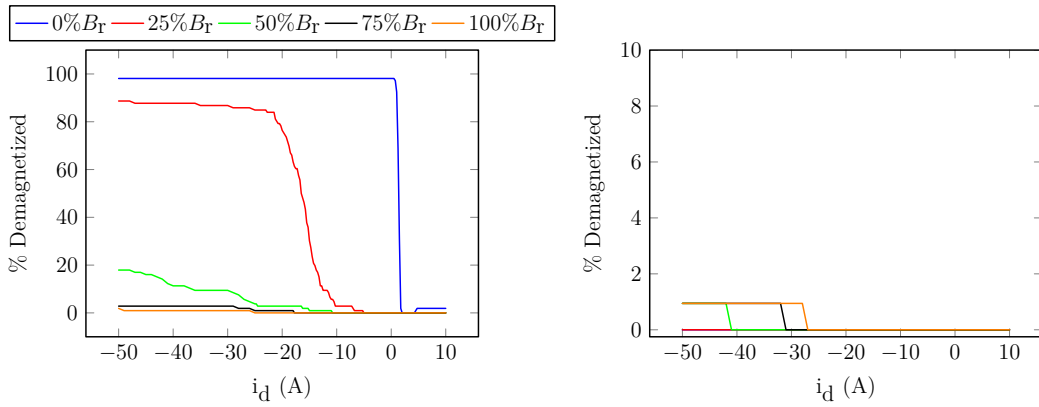
Figure 4.24: Incremental inductance and flux linkages for uniform demagnetization testing of the designed machine

4.4 Susceptibility to Demagnetization

The percentage of the magnet area operating in the third quadrant is discussed to understand the effect of demagnetization on further demagnetization. As more demagnetizing currents are applied, the flux density is reduced throughout the magnet. If the magnet has less than the healthy remnant flux density, the negative current required to reduce the flux density to zero decreases, as shown in Figure 4.25(a). In this case, care should be taken, as negative demagnetizing current can worsen the performance problems due to the air gap flux asymmetry.

The demagnetization of the healthy magnet next to the magnet with changing magnetization is shown in Figure 4.25(b). In the event of demagnetization of one magnet, the adjacent magnet has a negligible portion of it which has flux density reduced to zero. This is because the flux linking that magnet does not come from the same, but the adjacent pole.

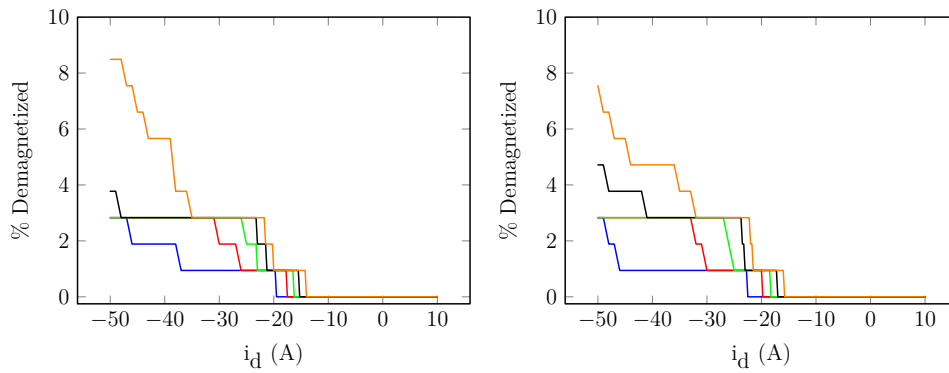
The curves in Figure 4.25(c) shows the percentage of magnet two—the magnet being demagnetized—which has operating points that fall below the knee of the magnet's BH curve and are permanently demagnetized. Note that this is calculated for a magnet temperature of 180 °C; the intrinsic coercivity of NdFeB magnets makes them very resistant to demagnetization at low temperatures. As the B_r of the magnet increases towards the nominal quantity, the magnet will have slightly more permanent demagnetization. This is due to the atypical field paths during partial demagnetization; the direct axis is saturated in a way that limits the effect of the direct axis current. This can be seen in the pole formed by magnets two and three in Figure 4.12, where the flux is perpendicular to the direct axis. In Figure 4.25(d), the effect is seen, but the magnet is slightly more resistant to demagnetization, as the half of the direct axis near magnet two is more saturated than the demagnetized magnet near



(a) Percentage of demagnetized nodes in Magnet (b) Percentage of demagnetized nodes in

1

Magnet 1



(c) Percentage of permanently demagne- (d) Percentage of permanently demagne-
tized nodes in Magnet 1 at 180°C tized nodes in Magnet 2 at 180°C

Figure 4.25: Percentage of demagnetized nodes with respect to remnant flux density and direct axis current

magnet two. This occurs because of both the flux of magnet three and the atypical flux patterns caused by a demagnetized magnet two.

Chapter 5

Machine Insulation Assessment

A low voltage, bar wound PMAC machine is used for analysis in this work. In this case, the bar conductors are coated with epoxy and when implanted in the slot, the conductors have insulation paper wrapped around them. The multiple insulation systems are described in [42]. The slot geometry and stator insulation are shown in Fig. 5.2(a). One pole of the actual machine geometry is given in Figure 5.2(b).

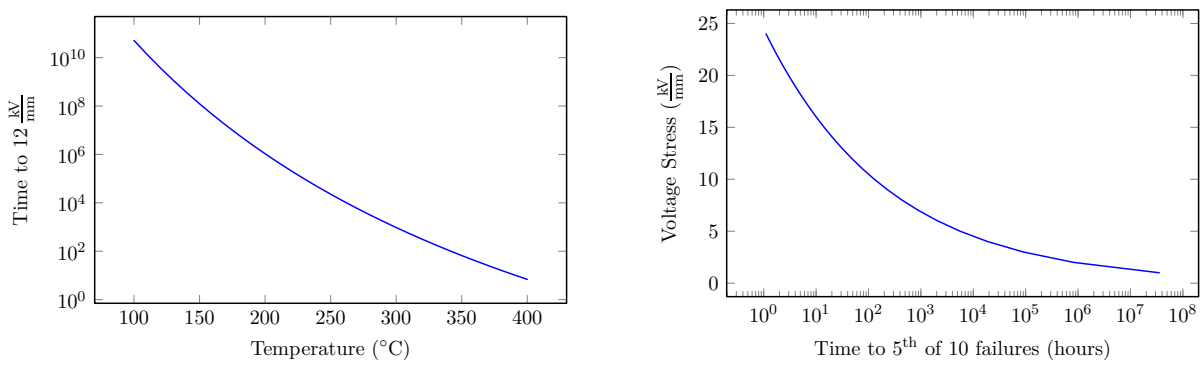
In order to study insulation degradation in the machine, the characteristics of the insulation must be known. The effect of the insulation paper is assumed to be the dominant insulation; the effect of the epoxy on insulation current is assumed to be negligible. The paper insulation used is the DuPont NOMEX 410 paper insulation detailed in [9] for analysis purposes. The nominal parameters are given in Table 5.1.

Table 5.1: Electrical characteristics of the insulation paper used [16]

Constant	25°C	100°C	250°C
Dielectric Constant 10 kHz, 50%RH	3.5	3.675	4.13
Volume Resistivity	4×10^{16}	4.9×10^{15}	5.1×10^{11}

The insulation degradation occurs due to thermal, electrical, chemical and mechanical factors. The mean time to failure decays exponentially with respect to the temperature by the Arrhenius model. The exact temperature dependent degradation from [9] is given in Figure Fig. 5.1(a) with its respective equation in (5.1). This relationship is a model of

the mean time to failure, where failure is defined as the point where the dielectric strength reaches 12 kV/mm. The mean time to failure due to voltage decays according to the inverse power law. The exact voltage dependent degradation from [9] is given in Figures Fig. 5.1(b) and (5.2). Chemical and mechanical degradation are very unpredictable and their causes vary widely. There is no single model for chemical and mechanical degradation; in some instances these are not present. For these reasons, only thermal and electric degradation are studied.



(a) Arrhenius degradation characteristic for thermal degradation to 12 $\frac{\text{kV}}{\text{mm}}$.

(b) Inverse power law degradation characteristic for voltage degradation.

Figure 5.1: Degradation characteristic curves

$$MTTF = 10^{\frac{8262}{T+273}-11.44}, \quad (5.1)$$

$$U_{b1} = 3.5462 \times 10^7 n_{b1}^{-5.4381}. \quad (5.2)$$

A finite element model (FEM) is used to calculate the equivalent capacitances and resistances from the data sheet parameters. Using the slot model in Figure Fig. 5.2(a), electrostatic and conduction simulations are performed to calculate the capacitance and resistance by measuring the energy and the current flowing in the insulation between each conductor

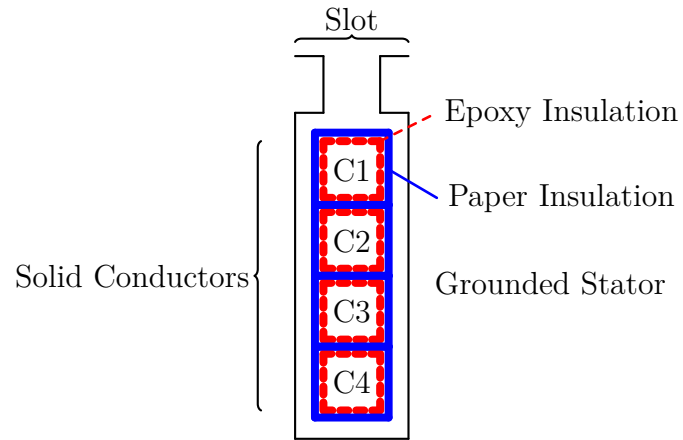
with each other, and from each conductor to ground. The nominal permittivity and resistivity used is taken given in [9] at 25°C and is given in Table Table 5.2. The simulations are performed in each case by applying 25 V uniformly between the conductors being tested, or the conductor and ground, respectively. This way, the relationship between each conductor, and from each conductor to ground is known. For the electrostatic simulation, the total energy in the electric field between the two regions being tested is determined and then the equation for the energy in a capacitor, $C = \frac{2W}{V^2}$, is used to determine the equivalent capacitance. For the conduction simulation, the total current leaving the line region of the primary test conductor is determined. This current is used with the voltage to determine the equivalent resistance.

Table 5.2: Nominal conduction and electrostatic finite element model characteristics

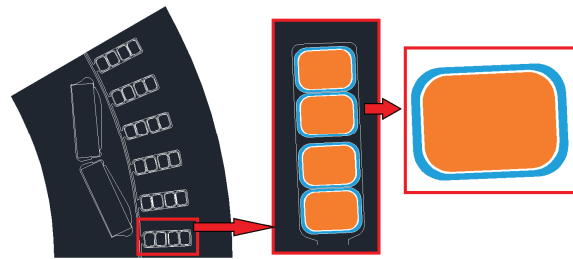
Parameter	Value
Dielectric Constant 1 kHz, 50%RH	3.5
Resistivity 1 kHz, 50%RH	1.5×10^{16}

The nominal electrical parameters are changed to simulate the effect of aging. The relative effect of aging upon the capacitance and resistance from Younsi *et al.*, [50] is used to determine the change in the parameters. The dielectric constant is assumed to move from its healthy value to the same as that of air ($\epsilon_r = 1$). The resistivity is assumed to increase from the nominal to forty times the nominal in the failed state. The effects of the change in permittivity and resistivity on capacitance and resistance, respectively, are shown in Fig. 5.3(a) and 5.3(b).

The insulation degradation model is verified in order to justify the change in parameters. Between both thermal and electrical degradation, thermal degraded insulation dominates in

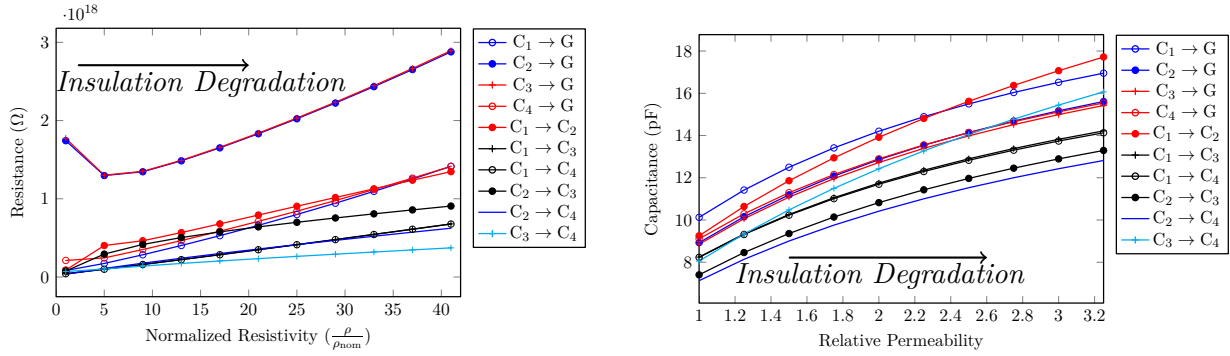


(a) Slot geometry used in finite element model



(b) Finite element model used for the electrostatic and conduction simulations.

Figure 5.2: Finite element model geometries used to determine the slot characteristics.



(a) Change in capacitance with insulation permittivity; results from FEA.

(b) Change in resistance with insulation conductivity; results from FEA.

Figure 5.3: Finite element model simulation results under parameter variation; use Figure 5.2(a) as reference

low voltage machines. This is clear from Fig. 5.4, from [12] which shows the degradation characteristics of twisted pairs due to voltage applied between them at both 10 kHz and 50 Hz. Other recent work, including the paper [43] has detailed the effect of voltage pulses on machine insulation. These tests are done both in air and in oil. When submerged in oil, the behavior of the degradation is similar to that of low voltage machines – no partial discharge is present. The degradation rate is much lower without PD. This is further demonstrated by the behavior of the twisted pairs in air becoming the same as in oil as the applied voltage decreases. The insulation degradation rate due to voltage without PD is very small; therefore the thermal degradation dominates in low voltage machines. The insulation degradation in [50] is therefore used to model degradation with the increase in resistivity and decrease in permittivity.

An analytical model is developed which takes into account the capacitances and resistances for testing diagnostic methods. An equivalent circuit is then developed which models the insulation using the capacitance and resistance components calculated from the finite

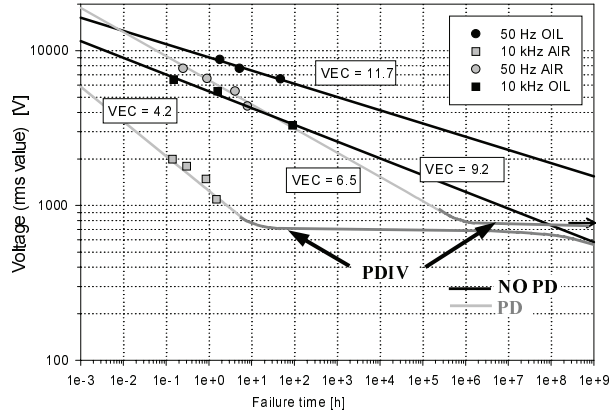


Figure 5.4: Plot showing the change in voltage failure performance with no partial discharge and as the voltage decreases (from [12])

element model. This circuit is given in Figure 5.5.

5.1 Machine Insulation Degradation Diagnosis

The methods described in [50] and [32] have been combined and an enhanced new method has been developed which measures the magnitude of the current during the switching transients. The method does not require the high sensitivity current transducers and because it measures the magnitude of the leakage current – a quantity directly related to the insulation condition – the method is useful for condition monitoring. The leakage current can be measured by applying a PWM voltage to phase A of the machine. This is done by using the voltage drop on resistors to calculate the input and output currents and subtracting the output from the input; the resulting voltage and current plots are given in Fig. 5.7(a). To simulate the effect of insulation degradation, the values of capacitance and resistance from the FEA work are used in the equivalent circuit.

It is not clear from the plot in Fig. 5.7(a) that the insulation current has a salient signature

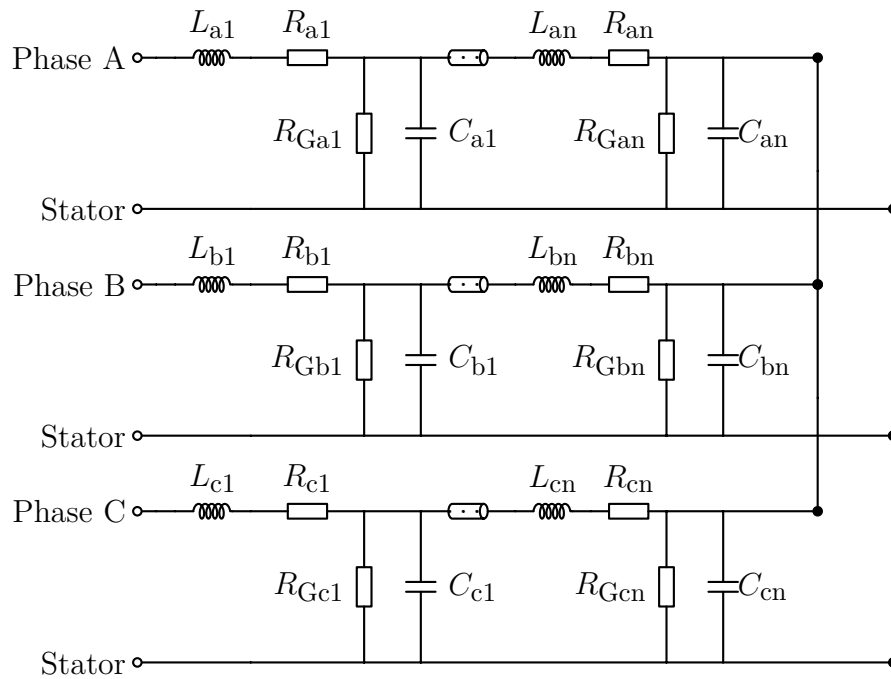


Figure 5.5: Machine stator equivalent circuit; n is the total number of conductors in the slots per phase

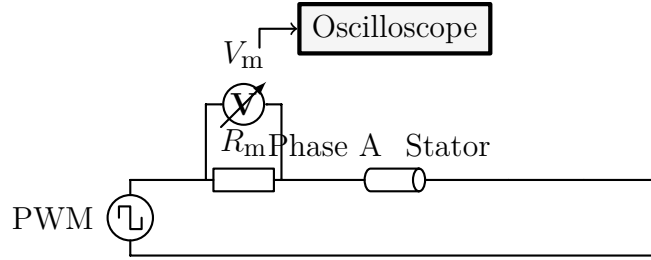


Figure 5.6: Leakage current measuring test circuit.

during the switching transients. In Fig. 5.7(b), the leakage current is shown over a smaller interval and the transient area is zoomed in. It is now easier to see that the leakage current has the behavior of a decaying sinusoid; the maximum peak of this is the insulation current magnitude. Note that the magnitude here is much greater than the magnitude of the grid voltage insulation current measurement method. While both methods include capacitive current, the higher dV/dt which causes a larger current through the leakage capacitance in the switching method. Because of this, no special sensor is required for this test method.

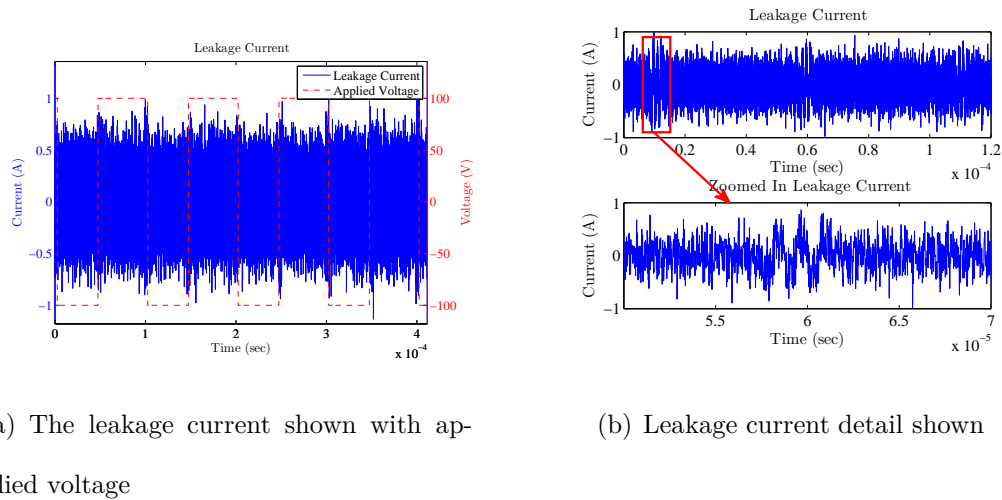


Figure 5.7: Simulated leakage current with applied voltage; (a) shows about 400 μsec of data and (b) zooms into up to 70 μsec .

The experimental method follows the same general approach as the simulation, and is

informed by the literature on the topic, including the works by Kavanagh *et al.* [19] as well as Grebchenko *et al.* [15]. The same circuit shown in Figure 5.6 is used to calculate the leakage current. A signal generator is used to generate a square voltage waveform of 20 V. The resistance of the two measuring resistors, 178 mΩ and 185 mΩ for R_{m1} and R_{m2} , respectively, is determined beforehand for accuracy. The resistor voltages are measured with an oscilloscope and are used to determine the current in each resistor. The difference between the input and output currents are used to calculate the leakage current. The same peak behavior is seen which can be used to characterize the leakage current, and therefore the condition of the insulation.

In order to test the diagnostic method, the current response to the first PWM pulse is given for different fault levels. The result of this for different fault levels is given in Fig. 5.8 for simulation.

The diagnosis method is also tested experimentally on a healthy machine, with the results given by Fig. 5.9.

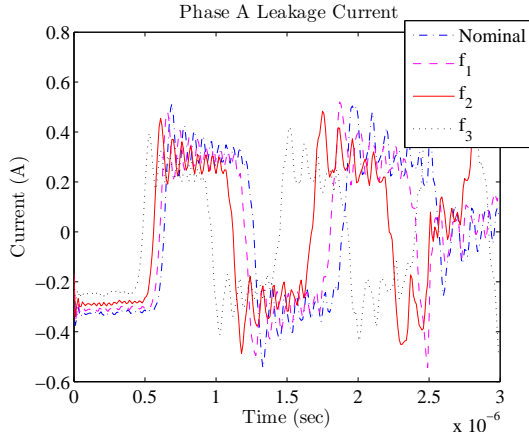


Figure 5.8: Leakage current after the initial voltage pulse is applied to the phase

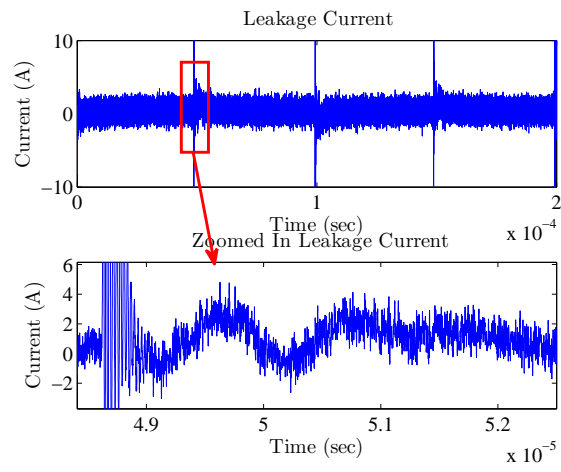


Figure 5.9: Experimental leakage current shown with detail

5.2 Insulation Degradation Prognosis

The prognosis of insulation faults is built upon degradation models. The proposed condition monitoring method is used to assess the condition of the insulation (diagnosis) and a degradation model allows for the prognosis of the insulation health.

The simulated accelerated lifetime leakage current data from [50] is fit to an exponential model with artificially added noise. The exponential fit is shown in Fig. 5.10. The exponential model is therefore used as our failure model. The exponential decay rate parameter (the β term) from [50] is used with the ‘healthy’ insulation current of 500 mA calculated from the simulation results in Fig. 5.7(b).

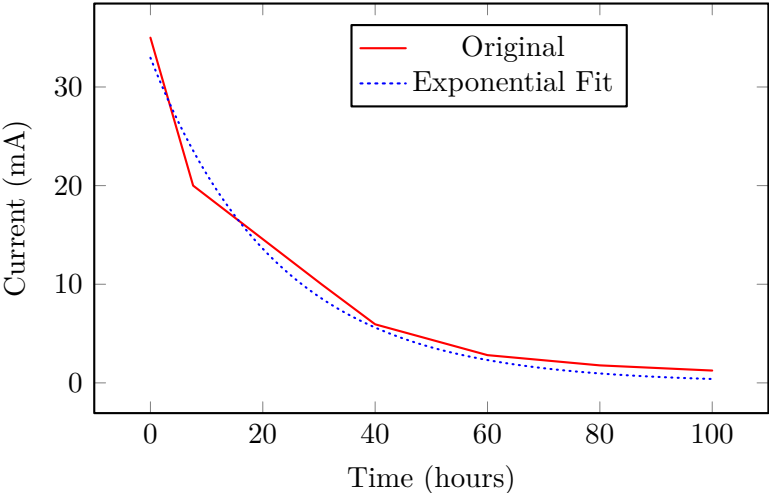


Figure 5.10: The original data from Younsi *et al.* [50] and an exponential fit for this

Given that the insulation current decays exponentially with insulation degradation, this model is used in the prognostic algorithm. Given a time series of data points, least squares minimization is used to fit the data points to a generic exponential model. Once this is complete it is possible to extrapolate the exponential model to a predefined insulation current failure limit. The difficulty with curve fitting is that the exponential model parameters, in

addition to the insulation current, change in time. By using the EKF, the insulation current measurement is used to model the degradation online, which takes into account changes in the trend and parameters. To do this, the generalized decaying exponential model in (5.3) and (5.4) is taken as the degradation model, where α and β are generalized model parameters. The state model is determined by taking the derivative of the degradation model as in (5.5).

$$I_{\text{leakage}} = \alpha e^{\beta t} \quad (5.3)$$

$$\alpha = I_{\text{healthy}} \quad (5.4)$$

$$\dot{I}_{\text{leakage}} = \alpha e^{\beta t} (\beta + t\dot{\beta}) + e^{\beta t} \dot{\alpha}. \quad (5.5)$$

Assuming that $\dot{\alpha} = 0$ and $\dot{\beta} = 0$ because they do not change quickly, the system becomes (5.6)–(5.8). The values do not change quickly because the degradation of the machine is not dynamic, but depends upon slow processes.

$$\dot{I}_{\text{leakage}} = \alpha e^{\beta t} (\beta + t\dot{\beta}) + e^{\beta t} \dot{\alpha} \quad (5.6)$$

$$\dot{\alpha} = 0 \quad (5.7)$$

$$\dot{\beta} = 0. \quad (5.8)$$

By discretizing with the forward difference method, the system becomes (5.10), and finally (5.11)–(5.13). k is the time instant index and Δ is the time between k and $k + 1$,

$$\frac{I_{\text{leakage}}(k+1) - I_{\text{leakage}}(k)}{\Delta} = I_{\text{leakage}}(k)\beta(k), \quad (5.9)$$

$$I_{\text{leakage}}(k+1) = I_{\text{leakage}}(k) + \Delta\beta(k)I_{\text{leakage}}(k) \quad (5.10)$$

$$\alpha(k+1) = \alpha(k) \quad (5.11)$$

$$\beta(k+1) = \beta(k). \quad (5.12)$$

The nonlinear model in (5.14) to (5.16), (5.19) and (5.20) can be used to generate the final model using the principles of the EKF. The f function represents the insulation current and its parameters. The h function reflects only the measured insulation current, as only the insulation current is measurable in the system, the α and β are not.

$$x(k+1) = f(x(k), u(k)) + w(k) \quad (5.13)$$

$$y(k) = h(x(k)) + v(k) \quad (5.14)$$

$$x(k) = \{x_1(k), x_2(k), x_3(k)\} \quad (5.15)$$

$$\dots = \{I_{\text{leakage}}(k), \alpha(k), \beta(k)\} \quad (5.16)$$

$$w(k) \sim N(0, Q(k)) \quad (5.17)$$

$$v(k) \sim N(0, R(k)) \quad (5.18)$$

$$f = \begin{pmatrix} I_{\text{leakage}}(k) + \Delta\beta(k)I_{\text{leakage}}(k) \\ \alpha(k) \\ \beta(k) \end{pmatrix} \quad (5.19)$$

$$h = I_{\text{leakage}}(k). \quad (5.20)$$

In order to test the EKF, data is generated which follows the degradation model with white

noise added. The EKF simulation assumes the values in Table 5.3.

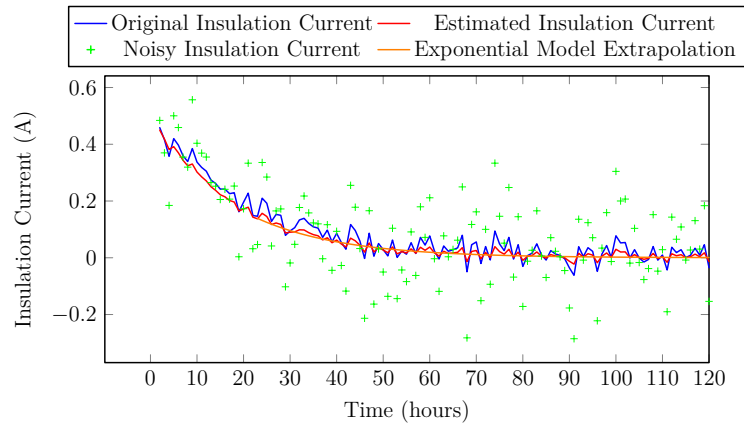
Table 5.3: Statistical Parameters used for the Kalman Filter

Parameter	Value
Actual α	4.7
Actual β	-.44
$\hat{\alpha}$	4.7
$\hat{\beta}$	-0.528
Measurement noise variance ($R(k)$) for x_1	0.05
Process noise variance ($Q(k)$) for x_1 (I_{leakage})	0.01
Process noise variance level ($Q(k)$) for x_2 (α)	0.01
Process noise variance level ($Q(k)$) for x_3 (β)	0.01
Initial state variance level (uncertainty) for all states	0.012

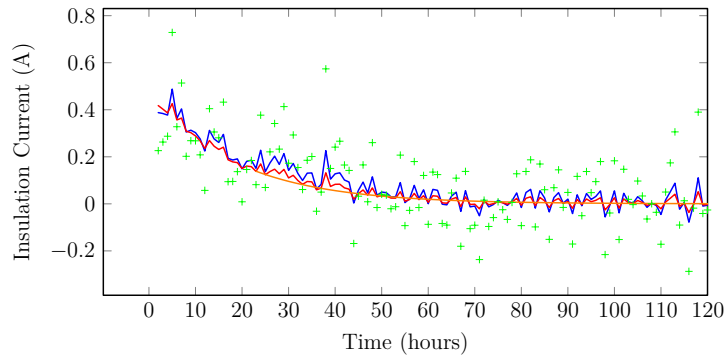
This section presents simulation results for the prognostic method. The prognosis results show the validity of the prognostic method for a case of simulated degradation.

In order to test the prognostic method, the EKF is applied to a set of noisy data with initial state and covariance conditions that differ from the actual values (the magnitude α found from experiments and the exponential parameter β from literature [50]) to test the convergence of the system. To allow for the correct convergence of the EKF, the α parameter is chosen to be near the actual value—This is possible because the insulation current can be assessed for a healthy machine. The β parameter is less well known; this is set to 20% below the actual quantity. The measurement noise variance is empirically determined to be 0.05. Because the model is fairly certain, the process noises are chosen to be 0.01. The initial state variance level is chosen to be 20% above the actual value. The result of the EKF run

is given in Figure Fig. 5.11. Note that the EKF quickly converges to the actual values. Two instances are given, each for one noise realization: Figure 5.11(a) corresponds to the original noise levels and Figure 5.11(b) shows the same results with 50% additional noise. The original insulation current is the actual, pre-noise insulation current. The noisy insulation current is what is used as the input—or measurement—to the EKF. The EKF is used to estimate the insulation current. Note that at the twenty-third sample the model parameters α and β from the EKF are used in an exponential model to extrapolate the insulation current. Note that the extrapolation matches well, since the EKF model converged to the actual parameters. With this exponential extrapolation, the lifetime of the machine can be calculated.



(a) Estimation with the original variance



(b) Estimation with 1.5 times the original variance

Figure 5.11: Estimated leakage current shown with the measurements and actual leakage current

Chapter 6

Conclusion

Given the ability to model the bond wire lift-off fault, insulation degradation, and demagnetization, diagnosis and prognosis schemes are introduced to improve the reliability of the inverter-driven motor drive. In each case, the effect of each fault is studied and the results are used to determine if a fault is present and understand the progression of the fault. This dissertation investigates the practical implementation of the inverter method with simulated accelerated aging, studies the electromagnetic behavior of a machine which has been demagnetized, and investigates the extraction of leakage current.

In the inverter characterization work, a novel inverter characterization procedure is investigated. The benefit of this method lies in its ability to identify individual device parameters, an important goal in monitoring the condition of all devices. The spectral method accurately characterizes the inverter. With the spectral method and calculation of the fast Fourier transform, the nonlinearities of interest are found. This is successfully extended to the alternating current case by way of the short-time Fourier transform. With the simulated and experimental work, these methods prove useful for the monitoring of inverter nonlinearities with both direct and alternating current.

The characterization method to accurately determine the device resistance is shown to detect small changes in the resistance, occurring with BWLO faults, previously a hurdle for using resistance for BWLO detection. Finally, by using characterization to improve the loss estimate, the calculation of RUL is improved.

The demagnetization diagnosis portion of this work introduces a method that is able to detect as well as distinguish partial from uniform demagnetization. The method was tested by investigating the demagnetization of one magnet in addition to uniform demagnetization. The method extends methods from literature by investigating the magnetic behavior of the machine in depth. By utilizing the incremental inductance, an effective detection method is introduced.

The process by which magnets further demagnetize is also studied by seeing the effect of local demagnetization under demagnetizing currents. In certain circumstances, such as high temperatures and when magnets have already been demagnetized somewhat, the magnets are more prone to irreversible and reversible demagnetization. By studying the process by which irreversible and reversible demagnetization occurs, both the machine electromagnetic design as well as controller design can be informed.

The insulation diagnosis and prognosis scheme is practical in that it does not require expensive sensors but only high sampling frequency oscilloscope and measuring resistors. The setup allows for the calculation of insulation current which can then be used with the diagnostic and prognostic technique to determine the remaining life of the machine insulation. A prognostic method is introduced for the machine insulation degradation using the extended Kalman filter. Previous work on insulation lifetime prediction only establishes correlation between the insulation current and the lifetime which follows the Arrhenius model for thermal degradation.

The diagnostic method proved able to detect changes in the overall condition of the stator insulation. Leakage current found at the switching transitions was shown to change as the parameters change. This method proved practical because the behavior of the experiment matched that of the simulation.

The prognostic method was shown to be able to track a noisy peak insulation current signal. As long as some rough information is known about the behavior of the insulation current, the EKF was shown to be effective even in the case that a limited amount of information was available about the degradation behavior.

APPENDIX

Appendix A

Measurement Circuit

Voltage sensors were used in the experiments in this work because the main goal was to evaluate the proposed method. Three practical issues of voltage sensing must be addressed to demonstrate the applicability of this method: sensors, scaling, and optimal ADC utilization. Having voltage sensors increases system cost and complexity. This work proposes a circuit to replace the voltage sensors. The relatively high cost of sensors can be avoided by adding a circuit using inexpensive components to detect device voltages. A scaling circuit would be necessary to scale voltage sensors; the complexity can be reduced by only using a circuit.

Scaling is an issue because the phase voltages measured will be over a very large range; the voltages must be properly scaled for the ADC, which is $0 - 3.3\text{ V}$ for most DSPs.

Some measured voltages are very high and others will be low with little information between the two. In order to maximize the ADC utilization the top and bottom voltage instances must be separated.

The three-stage circuit represented by Fig. A.1 was developed to accomplish this by scaling, separating the two voltages, and rectifying the result. The first sensing stage scales down both the DC-link voltage and the bottom device voltage V_{bot} with a differential op-amp circuit. The second stage has two roles: to amplify the small voltage to optimally utilize the ADC range and amplifying the large voltage beyond the range of the op-amp. The second stage amplifies V_{bot} as well as $V_{\text{bot}} - V_{\text{DC}}$; this results in the larger voltage of V_{bot} being amplified beyond the range of the op-amp, saturating the op-amp and effectively removing

that information. The same is true for the amplification of $V_{\text{bot}} - V_{\text{DC}}$, but the result is that the other device's voltage characteristic is saturated. Because the values near V_{DC} will be saturated when V_{bot} is amplified, that device's information will be lost. The same is true when $V_{\text{bot}} - V_{\text{DC}}$ is amplified, but for the other device's information. Because only two devices conduct in that phase for a given current, both characteristics can be determined at the current point with the output of both rectifier circuits. The third stage uses a precision amplifier op-amp circuit to rectify the negative voltages to assure that the voltage will remain in the range of allowed ADC inputs.

The circuit inputs, taken from experiments, are the DC-link voltage and the bottom device voltage, as shown in Fig. A.2(a). The circuit outputs given in Fig. A.2(b) correspond to the voltage of either device along with the saturated voltage values. The outputs are calculated using the proposed circuit simulated in TINA-TI. The device voltage takes up a considerable portion of the ADC range, maximizing ADC utilization and measurement precision.

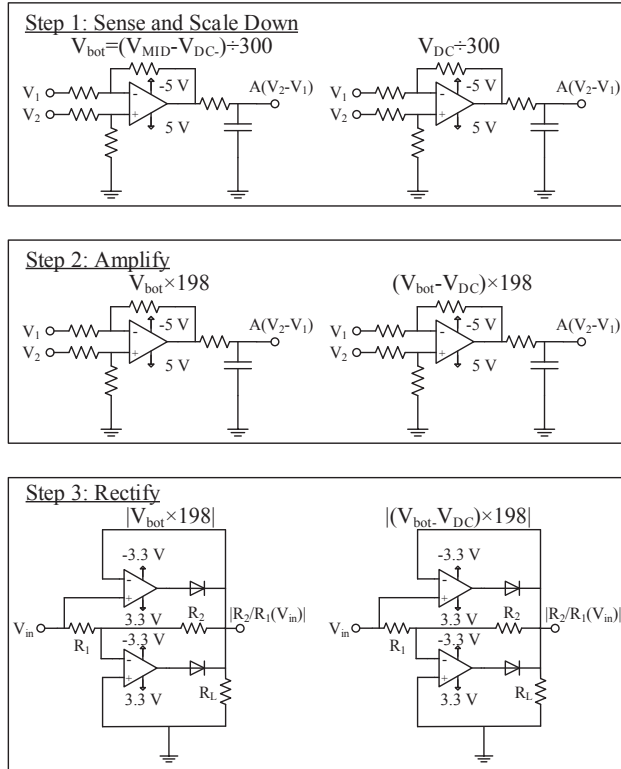
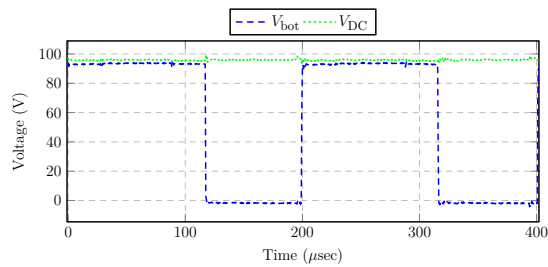
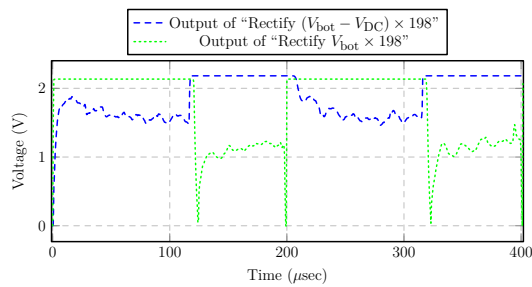


Figure A.1: Circuit to scale the voltages to within the analog to digital converter limits.



(a) Circuit input quantities.



(b) IGBT characteristic curves.

Figure A.2: Experimental phase A operating voltages and result used to test the circuit.

BIBLIOGRAPHY

BIBLIOGRAPHY

- [1] Qun-Tao An, Li-Zhi Sun, Ke Zhao, and Li Sun. Switching function model-based fast-diagnostic method of open-switch faults in inverters without sensors. *IEEE Trans. Power Electron.*, 26(1):119–126, 2011.
- [2] J.M. Anderson, R.W. Cox, and P. O’Connor. Online algorithm for early stage fault detection in igbt switches. In *Diagnostics for Electric Machines, Power Electronics and Drives (SDEMPED), 2013 9th IEEE International Symposium on*, pages 1–8, Aug 2013.
- [3] T. J. Barlow, S. Latham, I. S. McCrae, and P. G. Boulter. A reference book of driving cycles for use in the measurement of road vehicle emissions. Technical report, United Kingdom Transport Research Laboratory, 2009.
- [4] Reinhold Bayerer, Tobias Herrmann, Thomas Licht, Josef Lutz, and Marco Feller. Model for power cycling lifetime of IGBT modules - various factors influencing lifetime. In *Proc. 5th Int. Conf. on Integr. Power Syst. (CIPS)*, pages 1–6, 2008.
- [5] I. R. Bojoi, E. Armando, G. Pellegrino, and S. G. Rosu. Self-commissioning of inverter nonlinear effects in ac drives. In *Energy Conference and Exhibition (ENERGYCON), 2012 IEEE International*, pages 213–218, 2012.
- [6] D. Casadei, F. Filippetti, C. Rossi, and A. Stefani. Magnets faults characterization for permanent magnet synchronous motors. In *Diagnostics for Electric Machines, Power Electronics and Drives, 2009. SDEMPED 2009. IEEE International Symposium on*, pages 1–6, Aug 2009.
- [7] J.R. Celaya, A. Saxena, C.S. Kulkarni, S. Saha, and K. Goebel. Prognostics approach for power MOSFET under thermal-stress aging. In *Proc. of the Ann. Reliability and Maintainability Symposium*, pages 1–6, Jan 2012.
- [8] D. Diallo, M.E.H. Benbouzid, D. Hamad, and X. Pierre. Fault detection and diagnosis in an induction machine drive: A pattern recognition approach based on concordia stator mean current vector. *Energy Conversion, IEEE Transactions on*, 20(3):512–519, 2005.
- [9] DuPont. DUPONT (TM) NOMEX PAPER TYPE 410, August 2013.

- [10] A.G. Espinosa, J.A. Rosero, J. Cusido, L. Romeral, and J.A. Ortega. Fault detection by means of hilbert-huang transform of the stator current in a pmsm with demagnetization. *Energy Conversion, IEEE Transactions on*, 25(2):312–318, June 2010.
- [11] J.O. Estima and A.J. Marques Cardoso. A new algorithm for real-time multiple open-circuit fault diagnosis in voltage-fed PWM motor drives by the reference current errors. *IEEE Trans. Ind. Electron.*, 60(8):3496–3505, 2013.
- [12] D. Fabiani. *Accelerated Degradation of AC-Motor Winding Insulation Due to Voltage Waveforms Generated by Adjustable Speed Drivers*. PhD thesis, University of Bologna, 2003.
- [13] M. Farahani, E. Gockenbach, H. Borsi, K. Schallßer, and M. Kaufhold. Behavior of machine insulation systems subjected to accelerated thermal aging test. *IEEE Trans. Dielectr. Electr. Insul.*, 17(5):1364–1372, October 2010.
- [14] Shanelle Nicole Foster. *Operation of Interior Permanent Magnet Synchronous Machines with Fractional Slot Concentrated Windings under Both Healthy and Faulty Conditions*. PhD thesis, Michigan State University, 2013.
- [15] N.V. Grebchenko, M.A. Smirnova, and A.V. Kozhukhar. Continuous condition monitoring of the electrical insulation of ac motors without disconnection. In *Power Electronics, Electrical Drives, Automation and Motion (SPEEDAM), 2014 International Symposium on*, pages 512–514, June 2014.
- [16] S. Grubic, J.M. Aller, Bin Lu, and T.G. Habetler. A survey on testing and monitoring methods for stator insulation systems of low-voltage induction machines focusing on turn insulation problems. *IEEE Trans. Ind. Electron.*, 55(12):4127–4136, Dec 2008.
- [17] J. Holtz and Juntao Quan. Sensorless vector control of induction motors at very low speed using a nonlinear inverter model and parameter identification. *IEEE Trans. Ind. Appl.*, 38(4):1087–1095, 2002.
- [18] Jongman Hong, Sanguk Park, Doosoo Hyun, Tae june Kang, Sang Bin Lee, C. Kral, and A. Haumer. Detection and classification of rotor demagnetization and eccentricity faults for pm synchronous motors. *Industry Applications, IEEE Transactions on*, 48(3):923–932, May 2012.
- [19] D.F. Kavanagh, D.A. Howey, and M.D. McCulloch. An applied laboratory characterisation approach for electric machine insulation. In *Diagnostics for Electric Machines, Power Electronics and Drives (SDEMPED), 2013 9th IEEE International Symposium on*, pages 391–395, Aug 2013.

- [20] M. Kazerooni and N.C. Kar. Methods for determining the parameters and characteristics of pmsm. In *Electric Machines & Drives Conference (IEMDC), 2011 IEEE International*, pages 955–960. IEEE, 2011.
- [21] J. Lehmann, M. Netzel, R. Herzer, and S. Pawel. Method for electrical detection of bond wire lift-off for power semiconductors. In *Power Semiconductor Devices and ICs, 2003. Proceedings. ISPSD '03. 2003 IEEE 15th International Symposium on*, pages 333–336, 2003.
- [22] W. Leonhard. *Control of Electrical Drives*. Springer, 2001.
- [23] Kan Liu and Z.Q. Zhu. Online estimation of the rotor flux linkage and voltage-source inverter nonlinearity in permanent magnet synchronous machine drives. *IEEE Trans. Power Electron.*, 29(1):418–427, 2014.
- [24] J. Lutz. *Halbleiter-Leistungsbaulemente*. SpringerLink:Bücher. Springer Vieweg, 2012.
- [25] MATLAB. *version 7.10.0 (R2010a)*. The MathWorks Inc., Natick, Massachusetts, 2010.
- [26] J.D. McFarland and T.M. Jahns. Influence of d- and q-axis currents on demagnetization in pm synchronous machines. In *Energy Conversion Congress and Exposition (ECCE), 2013 IEEE*, pages 4380–4387, Sept 2013.
- [27] J.D. McFarland and T.M. Jahns. Investigation of the rotor demagnetization characteristics of interior PM synchronous machines during fault conditions. *IEEE Trans. Ind. Appl.*, 50(4):2768–2775, July 2014.
- [28] F. Meinguet, P. Sandulescu, X. Kestelyn, and E. Semail. A method for fault detection and isolation based on the processing of multiple diagnostic indices: Application to inverter faults in ac drives. *Vehicular Technology, IEEE Transactions on*, 62(3):995–1009, March 2013.
- [29] M. Mengoni, L. Zarri, A. Tani, Y. Gritli, G. Serra, F. Filippetti, and D. Casadei. On-line detection of high-resistance connections in multiphase induction machines. *Power Electronics, IEEE Transactions on*, PP(99):1–1, 2014.
- [30] Du Mingxing, Wei Kexin, Li Jian, and Xie Linlin. Condition monitoring igbt module bond wire lift-off using measurable signals. In *Power Electronics and Motion Control Conference (IPEMC), 2012 7th International*, volume 2, pages 1492–1496, 2012.

- [31] P. Neti, K. Younsi, and M.R. Shah. A novel high sensitivity differential current transformer for online health monitoring of industrial motor ground-wall insulation. In *Energy Conversion Congr. and Exposition*, pages 2493–2499, Sept 2013.
- [32] P. Nussbaumer, M.A. Vogelsberger, and T.M. Wolbank. Exploitation of induction machine’s high-frequency behavior for online insulation monitoring. In *9th Annu. Int. Symp. on Diagnostics for Electric Machines, Power Electron. and Drives*, pages 579–585, Aug 2013.
- [33] P. Nussbaumer, T.M. Wolbank, and M.A. Vogelsberger. Separation of disturbing influences on induction machine’s high-frequency behavior to ensure accurate insulation condition monitoring. In *28th Annu. Appl. Power Electron. Conference and Exposition*, pages 1158–1163, March 2013.
- [34] G. Pascoli, W. Hribernik, and G. Ujvari. A practical investigation on the correlation between aging and the dissipation factor value of mica insulated generator windings. In *Int. Conference on Condition Monitoring and Diagnosis*, pages 268–271, April 2008.
- [35] K. M. Rahman and S. Hiti. Identification of machine parameters of a synchronous motor. *IEEE Transactions on Industrial Applications*, 41:557–565, 2005.
- [36] J.-R. Riba Ruiz, J.A. Rosero, A.G. Espinosa, and L. Romeral. Detection of demagnetization faults in permanent-magnet synchronous motors under nonstationary conditions. *Magnetics, IEEE Transactions on*, 45(7):2961–2969, July 2009.
- [37] J. Rosero, L. Romeral, J.A. Ortega, and J.C. Urresty. Demagnetization fault detection by means of hilbert huang transform of the stator current decomposition in pmsm. In *Industrial Electronics, 2008. ISIE 2008. IEEE International Symposium on*, pages 172–177, June 2008.
- [38] J.A. Rosero, J. Cusido, A. Garcia, J.A. Ortega, and L. Romeral. Study on the permanent magnet demagnetization fault in permanent magnet synchronous machines. In *IEEE Industrial Electronics, IECON 2006 - 32nd Annual Conference on*, pages 879–884, Nov 2006.
- [39] K.S. Smith, L. Ran, and J. Penman. Real-time detection of intermittent misfiring in a voltage-fed PWM inverter induction-motor drive. *IEEE Trans. Ind. Electron.*, 44(4):468–476, 1997.
- [40] Yantao Song and Bingsen Wang. Survey on reliability of power electronic systems. *IEEE Trans. Power Electron.*, 28(1):591–604, 2013.

- [41] Zukui Song and Dilip V. Sarwate. The frequency spectrum of pulse width modulated signals. *Signal Process.*, 83(10):2227–2258, 2003.
- [42] G.C. Stone, E.A. Boulter, I. Culbert, and H. Dhirani. Electrical insulation for rotating machines-design, evaluation, aging, testing, and repair - book review. *IEEE Electr. Insul. Mag.*, 20(3):65–65, May 2004.
- [43] Peng Wang, A. Cavallini, and G. Montanari. The influence of repetitive square wave voltage parameters on enameled wire endurance. *Dielectrics and Electrical Insulation, IEEE Transactions on*, 21(3):1276–1284, June 2014.
- [44] A.R. Weber and G. Steiner. An accurate identification and compensation method for nonlinear inverter characteristics for ac motor drives. In *Instrumentation and Measurement Technology Conference (I2MTC), 2012 IEEE International*, pages 821–826, 2012.
- [45] Dawei Xiang, L. Ran, P. Tavner, Shaoyong Yang, A. Bryant, and P. Mawby. Condition monitoring power module solder fatigue using inverter harmonic identification. *IEEE Trans. Power Electron.*, 27(1):235–247, 2012.
- [46] Dawei Xiang, Shaoyong Yang, L. Ran, P. Tavner, A. Bryant, and P. Mawby. Change of terminal characteristics of a voltage-source-inverter (VSI) due to semiconductor device degradation. In *Proc. 13th Euro. Conf. on Power Electron. and Applicat.*, pages 1–10, 2009.
- [47] Yali Xiong, Xu Cheng, Z.J. Shen, Chunting Mi, Hongjie Wu, and V.K. Garg. Prognostic and warning system for power-electronic modules in electric, hybrid electric, and fuel-cell vehicles. *IEEE Trans. Ind. Electron.*, 55(6):2268–2276, 2008.
- [48] Shaoyong Yang, Dawei Xiang, A. Bryant, P. Mawby, L. Ran, and P. Tavner. Condition monitoring for device reliability in power electronic converters: A review. *IEEE Trans. Power Electron.*, 25(11):2734–2752, 2010.
- [49] Shaoyong Yang, Dawei Xiang, A. Bryant, P. Mawby, L. Ran, and P. Tavner. Condition monitoring for device reliability in power electronic converters: A review. *IEEE Trans. Power Electron.*, 25(11):2734–2752, 2010.
- [50] K. Younsi, P. Neti, M. Shah, J.Y. Zhou, J. Krahn, Konrad Weeber, and C.D. Whitefield. On-line capacitance and dissipation factor monitoring of AC stator insulation. *IEEE Trans. Dielectr. Electr. Insul.*, 17(5):1441–1452, October 2010.

- [51] W.G. Zanardelli, E.G. Strangas, and S. Aviyente. Identification of intermittent electrical and mechanical faults in permanent-magnet ac drives based on time-frequency analysis. *IEEE Trans. Ind. Appl.*, 43(4):971–980, 2007.